VILNIUS UNIVERSITY
CENTER FOR PHYSICAL SCIENCES AND TECHNOLOGY

Mindaugas Karaliūnas

Investigation of Zinc Oxide Heterostructures for Optoelectronic Devices by Means of Spectroscopy Methods

Doctoral dissertation
Technological Science, Materials Engineering (08 T),

Vilnius, 2013

Dissertation was prepared in 2008 – 2012 at the Institute of Applied Research and Department of Semiconductor Physics of Vilnius University.

Scientific supervisor:

Prof. habil. dr. Edmundas Kuokštis (Vilnius University, Technological Science, Materials Engineering – 08 T).

VILNIAUS UNIVERSITETAS
FIZINIŲ IR TECHNOLOGIJOS MOKSLŲ CENTRAS

Mindaugas Karaliūnas

Optoelektronikos prietaisams skirtų įvairialyčių cinko oksido darinių tyrimas spektroskopijos metodais

Daktaro disertacija
Technologijos mokslai, medžiagų inžinerija (08 T),

Vilnius, 2013

Disertacija rengta 2008 – 2012 metais Vilniaus universiteto Taikomųjų mokslų institute bei Fizikos fakulteto Puslaidininkių fizikos katedroje.

Mokslinis vadovas:
Prof. habil. dr. Edmundas Kuokštis (Vilniaus universitetas, technologijos mokslai, medžiagų inžinerija – 08 T).

Acknowledgements

First of all, I would like to thank my scientific supervisor prof. Edmundas Kuokštis for support, near to infinite trust and non-exceeding patience during my research work. I appreciate the opportunity to work with prof. Edmundas Kuokštis and learn the methods for doing science. Also I am thankful to the reviewers of the dissertation prof. Vladimiras Gavriušinas and dr. Tadas Malinauskas for valuable suggestions to improve the work and fruitful discussions.

I am very thankful to my teachers prof. Artūras Žukauskas, prof. Gintautas Tamulaitis, prof. Saulius Juršėnas, prof. Kęstutis Jarašiūnas, dr. Karolis Kazlauskas, and dr. Jūras Mickevičius at Institute of Applied Research for care, support and inspiration by their work. I am very grateful to my internship supervisor prof. C.-C. Yang for warm and unforgettable welcome at Institute of Photonics and Optoelectronics of National Taiwan University. Besides, I feel gratitude to my scientific research work supervisors dr. Galia Pozina and prof. Bo Monemar at Linköping University for kind hosting during my Erasmus studies in Sweden. Last, but not least, I am sincerely thankful to my first research practice supervisors dr. Bonifacijus Vengalis and dr. Renata Butkutė for supporting me in my first not firm steps towards science.

I would like to thank my elder colleagues dr. Algirdas Novičkovas, dr. Pranciškus Vitta, dr. Saulius Miasojedovas, dr. Natalija Kurilčik, dr. Algirdas Mekys, dr. Ramūnas Aleksiejūnas, dr. Arūnas Kadys, dr. Genadij Kurilčik, and dr. Zenonas Vaitonis at Institute of Applied Research for friendly environment and kind help during research work. Also, I would like to thank administration of Department of Semiconductor Physics of Physics Faculty for help solving many administrative issues: Justė Kudzytė, Jolanta Juodvalkienė, and Tatjana Zaiceva. I would like to thank my colleagues dr. Shao-Ying Ting at National Taiwan University and dr. Saulius Burinskas at Kaunas University of Technology, and prof. Egidijus Anisimovas at

Department of Theoretical Physics of Vilnius University for fruitful cooperation.

I acknowledge Science Council of Lithuania for financial support for internship at National Taiwan University through the programme "The internships for PhD students at foreign research institutions" and international conference "7$^{\text{th}}$ International Workshop on ZnO and Related Materials (IWZnO-2012)". Also, I acknowledge Physics Faculty of Vilnius University for financial support for conference "16$^{\text{th}}$ International Semiconducting and Insulating Materials Conference (SIMC-XVI)".

I would like to express my gratitude to dear friends and colleagues dr. Paulius Pobedinskas, dr. Vygintas Jankus, dr. Vytautas Liuolia, dr. Mindaugas Pranaitis, and dr. Saulius Nargėlas for always being good example of highly motivated and successful researchers. I would like to thank my younger colleagues PhD students Arūnas Miasojedovas, Darius Dobrovolskas, Lina Skardžiūtė, Jonas Jurkevičius, Dima Ševčenko, Steponas Raišys, Patrik Ščajev, Akvilė Zabiliūtė (for introducing with LaTeX), Egidijus Songaila, Vytautas Butkus (for BibTeX style), Kuan-Yu Chen, Tsung-Chin Cheng, and Chieh Hsieh.

I acknowledge students for contribution in experiments and research work as part of their scientific research practice at Institute of Applied Research: Tomas Serevičius, Vilmantas Šukauskas, Marius Stasiūnas, Vytautas Tumas, Vaiva Nagytė, Tadas Gulbinas, Vilius Čeladinas, Tomas Kristijonas Uždavinys, and Vytautas Šimkevičius.

With the opportunity, I thank my valuable and supportive friends Justa Rimkutė, Vasilij Michejev, Tomas Kumidajus, Martynas Plukys, PhD student Violeta Bečytė, PhD student Justas Tilindis, Aistė Norkutė, dr. Andrius Šuminas, and Belle Liu. I feel grateful to my friends in the way Deividas Nikiforovas and Aliona Kalbasova, as well as to the punk rock band "Padugnės" members Krešas, Nindze, Blonde and Tango giving me right mood during my work. Thanks to my friend PhD student Gabija Toleikytė for inspiring me to continue studies and research work.

Also, I am thankful to my dear family for being supportive and perceptive during my long decade-lasting years of studies at Vilnius University: father prof. Simas Karaliūnas, mother Jūratė Karaliūnienė, sisters Viktorija Gasparaitienė and Simona Storækre, brother-in-law Torstein Storækre, aunt Violeta Dapšienė and especially uncle dr. Kastytis Dapšys.

Contents

List of Abbreviations

i-type	Insulating type
n-type	Negative type
p-type	Positive type
A^0X	Neutral acceptor bound exciton
AFM	Atomic force microscopy
Ag	Silver
Al	Aluminium
CCD	Charge coupled device
Cd	Cadmium
CdS	Cadmium sulphite
CIE	*Commission Internationale de l'Eclairage*
Cu	Copper
CW	Continuous wave
D^0X	Neutral donor bound exciton
DAP	Donor-acceptor pair
DBX	Donor bound exciton
DC	Direct current
DOS	Density of states
DRC	Deep recombination centres
EDX	Energy dispersive X-ray spectroscopy
EHP	Electron-hole plasma
EL	Electroluminescence
Fe	Iron
FWHM	Full width at half maximum
FX	Free exciton
GaAs	Gallium arsenide
GaN	Gallium nitride
HE	High energy
HT	Hydrothermal
InP	Indium phosphide
IQE	Internal quantum efficiency
IR	Infrared
ISI	Information Scientific Institute
K	Potassium or Kelvin (measurement unit for temperature)
LD	Laser diode
LED	Light emitting diode
Li	Lithium
LITH	Light-induced transient gratings
LO	Longitudinal optical phonon
LSP	Localized surface plasmon
M-band	Biexcitons interaction luminescence band
MBE	Molecular beam epitaxy
Mg	Magnesium
MOCVD	Metalorganic chemical vapour deposition
MQWs	Multiple quantum wells
Na	Sodium

NBE	Near band edge
NIR	Near infrared
NP	Nanoparticles
OG	Optical gain
P-band	Excitons interaction luminescence band
Pb	Lead
PL	Photoluminescence
PMT	Photomultiplier tube
QD	Quantum dot
QW	Quantum well
RT	Room temperature
SCAM	$ScAlMgO_4$ crystal
SE	Stimulated emission
SEM	Scanning electron microscopy
Si	Silicon
SNOM	Scanning near optical field microscopy
TCSPC	Time correlated single photon counting
TES	Two electron satellite
UV	Ultraviolet
V_O	Oxygen vacancies
V_{Zn}	Zinc vacancies
VSL	Variable stripe length
XRD	X-ray diffraction
YAG:Nd	Neodymium doped yttrium aluminium garnet
ZnO	Zinc oxide
ZnSe	Zinc selenite

Abstract

ZnO is a promising material for optoelectronics as stable, reliable, wide direct band-gap therefore transparent for visible light semiconductor. The band gap around 3.37 eV at room temperature results the absorption-edge and emission in near ultraviolet wavelength region of the spectrum. The unique feature of the material is huge binding energy of excitons (60 meV). This allows studying the exciton system experimentally even at room temperature. Moreover, stimulated emission induced by interaction of excitons leads to high lasing stability and low stimulated emission threshold.

Introducing Mg or Cd into ZnO lattice in combination with nanotechnology opens attractive perspective for the band gap engineering which is essential in modern optoelectronics. The ternary MgZnO alloys demonstrate even better optical properties than merely ZnO does. Therefore MgZnO has strong potential to be applied in solar blind photodetectors, as well in deep ultraviolet light-emitting diodes. The CdZnO quantum structures may be alternative to blue and green InGaN based light-emitting diodes and lasers.

In this work, the results on ZnO, MgZnO and CdZnO epitaxial layers, heterostructures and quantum well structures studied by means of advanced spectroscopy techniques are presented. The research was done addressing to the up-to-date issues on ZnO and related materials application in optoelectronics. The following aspects are investigated in this work:

- Stimulated emission mechanisms and optical gain features of high quality ZnO epitaxial layers;
- Optical properties of highly conductive Ga doped ZnO epitaxial layers;
- Characterization of N doped ZnO layers;
- Exciton localization effect in ternary MgZnO epitaxial layers;
- Optical characterization of CdZnO/ZnO multiple quantum wells structures for light-emitting diodes.

Number of advanced spectroscopy techniques was applied in the studies of the ZnO and ZnO-based structures. In this work, the experiments were carried out applying the spectrally-resolved time-integrated photoluminescence spectroscopy in stationary or quasistationary (nanosecond) excitation conditions, as well picosecond pulsed excitation conditions. The transmission spectroscopy was applied for the absorption spectra measurements. The time-resolved photoluminescence spectroscopy was applied for carrier dynamics investigation applying the time correlated single photon counting technique, streak camera apparatus or the time-resolved spectrally-integrated photoluminescence decay measurement technique with the Kerr gate. The light-induced transient grating technique was used for investigation of carrier dynamics. The advanced scanning near optical field microscopy was used for photoluminescence measurements with nano-scale resolution. Together with optical characterisation the crystal structure analysis was carried out using X-ray diffraction, atomic force microscopy and scanning electron microscopy, as well energy dispersive X-ray spectroscopy.

The analysis of ZnO photoluminescence spectra led to the problem, that the P-band due to exciton-exciton interaction is usually overlapped with the photoluminescence bands caused by other radiative recombination mechanisms. In order to determine the position of P-band, the exciton-exciton interaction model was analysed theoretically. The theoretical P-band maximum is in typical energy position for inelastic collision of free excitons, i.e. at the position shifted to longer wavelengths by two excitons binding energy E_x^b from the band gap energy. However, there is an experimental fact of diversity of the P-band energies varying from sample to sample. It was shown, that the reason is the inelastic interaction of free excitons with localized excitons, which has lower energy by value of localization energy ΔE_{loc}. It was taken into account in calculations of the P-band spectra and the shift to the side of the lower photon energy by the localization energy value was demonstrated.

The photoluminescence investigation of the molecular beam epitaxy grown MgZnO layers revealed the S-shaped photoluminescence spectra peak position dependence on temperature. This behaviour is attributed to the carrier localization in randomly distributed potential field fluctuations. However, for the first time photoluminescence peak position dependence on temperature with two blue-shifts for samples with high Mg content is measured.

The model of the band-filling of density-of-states tail is created with the presence of the two energy separated Gaussian-like density-of-states tail. The scanning near optical field microscopy experiment proved the presence of less than 100 nm width Mg rich areas with enhanced luminescence intensity. The carriers are localized within Mg rich areas due to Mg inhomogeneous distribution and are prevented from escaping to Mg absent areas by potential barriers. The second localization field for carriers is present in the Mg absent areas. It proves the double scale potential field profile described by photoluminescence experiment. The atomic force microscopy and energy dispersive X-ray spectroscopy experiments revealed a correlation of structural quality with the calculated average carriers localization energy.

The CdZnO/ZnO multiple quantum wells structures for 505 nm emission light-emitting diodes were characterized optically and compared with the corresponding InGaN/GaN multiple quantum wells structures. The photoluminescence intensity of CdZnO/ZnO multiple quantum wells structures is by two orders of magnitude lower than that of InGaN/GaN multiple quantum wells structures. The photoluminescence decay time of CdZnO/ZnO multiple quantum wells was measured in the range from 30 ps to 50 ps at room temperature and it depends on the growth conditions. The measured photoluminescence decay time of InGaN/GaN multiple quantum wells is around 4 ns, therefore it is two orders of magnitude greater than for CdZnO/ZnO structures. The difference in the luminescence properties of CdZnO/ZnO and InGaN/GaN multiple quantum wells structures for 505 nm emission light-emitting diodes can not be attributed merely to the crystal quality of the active layers, as the internal quantum efficiency is 5% and 15%, respectively. It was ascertained, that weak carrier localization effect in CdZnO/ZnO multiple quantum wells structures is important reason for the low emission efficiency.

Reziumė

ZnO — tiesiatarpis puslaidininkis, puikiai tinkantis taikymams optoelektronikoje dėl savo savybių, tokių kaip stabilumas, kietumas, skaidrumas regimajai spektro sričiai. ZnO draustinis tarpas kambario temperatūroje yra 3,37 eV. Tai lemia krašto sugertį ir liuminescenciją artimojo ultravioleto spektrinėje srityje. Išskirtinė ZnO savybė yra nepaprastai didelė eksitonų ryšio energija (60 meV), todėl ZnO yra tinkama terpė eksperimentiškai tirti eksitonų sistemos savybes net ir kambario temperatūroje. Be to, eksitonų sąveika pagrįsta priverstinė spinduliuotė pasižymi aukštu šviesos emisijos stabilumu ir žemu optinio stiprinimo slenksčiu.

Įterpiant Mg ar Cd į ZnO kristalinę gardelę, atliekama draustinio tarpo inžinerija, kuri yra esminis reikalavimas puslaidininkinių medžiagų grupėms šiuolaikinei optoelektronikai dėl nanotechnologijų teikiamos naudos. Trigubi MgZnO lydiniai pasižymi net geresnėmis optinėmis savybėmis, nei tiktai ZnO, todėl MgZnO turi dideles galimybes būti panaudotas saulės neakinamiems fotodiodams ir ultravioleto spektrinės srities šviestukams. CdZnO kvantinės struktūros gali tapti alternatyva InGaN pagrindu gaminamiems mėlyniems ir žaliems šviestukams ir lazeriams.

Šiame darbe pateikiami ZnO, MgZnO ir CdZnO epitaksinių sluoksnių, heterodarinių ir kvantinių struktūrų tyrimų, atliktų taikant pažangios spektroskopijos metodus, rezultatai. Atlikti tyrimai skirti spręsti dabartines ZnO ir susijusių junginių taikymo optoelektronikoje problemas. Šiame darbe nagrinėjami problematikos aspektai:

- aukštos kokybės ZnO epitaksinių sluoksnių priverstinės spinduliuotės mechanizmai ir optinio stiprinimo ypatybės;
- didelio laidumo Ga legiruotų ZnO epitaksinių sluoksnių optinės savybės;
- N legiruotų ZnO sluoksnių charakterizavimas;

- eksitonų lokalizacijos efektai MgZnO epitaksiniuose sluoksniuose;
- CdZnO/ZnO daugkartinių kvantinių duobių struktūrų, skirtų šviestukams, optinis charakterizavimas.

ZnO ir susijusių junginių struktūrų tyrimams buvo taikyti įvairūs pažangios spektroskopijos metodai. Šiame darbe atliktuose eksperimentuose buvo naudojama spektrinės skyros, laike integruotos fotoliuminescencijos spektroskopija nuostoviomis ir kvazinuostoviomis nanosekundinio sužadinimo sąlygomis, taip pat pikosekudinio impulsinio sužadinimo sąlygomis. Sugerties krašto matavimams buvo naudojama optinio pralaidumo spektroskopija. Laikinės skyros fotoliuminescencijos spektroskopija buvo taikoma krūvininkų dinamikos tyrimams panaudojant laike koreliuotų pavienių fotonų skaičiavimo metodą, greitaveikę fotoregistracijos kamerą ir laikinės skyros spektriškai integruotą fotoliuminescencijos gesimo matavimo metodą su Kero sklende. Krūvininkų dinamikai tirti buvo pasitelkta pažangi šviesa indukuotų laikinių gardelių metodika. Fotoliuminescencijos matavimams su šimtų nanometrų eilės skiriamąja geba buvo panaudota pažangi skenuojanti artimojo optinio lauko mikroskopija. Kartu su optiniais charakterizavimo metodais buvo atlikta kristalų struktūros ir sudėties matavimai naudojant Rentgeno spindulių difrakciją, atominės jėgos mikroskopiją, skenuojančią elektroninę mikroskopiją, o taip pat spektrinės skyros Rentgeno spindulių spektroskopiją.

ZnO fotoliuminescencijos spektrų analizė atskleidė, kad netamprios eksitonų sąveikos sąlygota spektrinė P-juosta dažnai persidengia su kitų rekombinacijos mechanizmų spektrinėmis juostomis. Siekiant nustatyti P-juostos padėtį, buvo analizuojamas eksitono-eksitono sąveikos teorinis modelis. Teorinė P-juostos smailė yra ties griežtai apibrėžta energija, kuri yra dviejų eksitono ryšio energijų E_x^b atstumu nuo draustinio tarpo. Tačiau eksperimentiškai išmatuojamų P-juostų smailių padėtys varijuoja ir skirtinguose bandiniuose skiriasi. Parodyta, kad to priežastimi yra netampri laisvų eksitonų sąveika su lokalizuotais eksitonais, kurių ryšio energija yra mažesnė per lokalizacijos energijos vertę ΔE_{loc}. Tai buvo įskaityta skaičiuojant P-juostos spektrą ir parodytas poslinkis į mažesnės fotonų energijos pusę per lokalizacijos energijos vertę.

Molekulinio pluošto epitaksijos būdu užaugintų MgZnO sluoksnių fotoliuminescencijos tyrimai parodė S-formos smailės padėties priklausomybę nuo

temperatūros. Šis efektas priskiriamas krūvininkų lokalizacijai atsitiktinai pasiskirsčiusiose potencialinio lauko fliuktuacijose. Tačiau bandiniuose su dideliu Mg kiekiu pirmą kartą buvo išmatuota fotoliuminescencijos smailės padėties priklausomybė nuo temperatūros su dviem mėlynaisiais poslinkiais. Pasiūlytas būsenų tankio uodegos pildymo modelis, kai būsenų tankio uodegą formuoja dvi skirtingos energijos padėties Gauso funkcijos. Skenuojančios artimojo optinio lauko mikroskopijos eksperimentas patvirtino esant mažesnių nei 100 nm skersmens sričių su padidintu Mg kiekiu ir padidėjusiu liuminescencijos intensyvumu. Krūvininkai yra lokalizuoti srityse su padidintu Mg kiekiu dėl nehomogeniško Mg pasiskirstymo ir negali pereiti į sritis su mažesniu Mg kiekiu. Antrasis krūvininkus lokalizacijantis laukas yra mažesnio Mg kiekio srityse. Tai patvirtina dviejų skalių potencialinio lauko modelį, nustatytą fotoliuminescencijos eksperimentu. Matavimai, atlikti atominės jėgos mikroskopu ir spektrinės skyros Rentgeno spindulių spektrometru, atskleidė glaudų ryšį tarp struktūrinės sluoksnių kokybės parametrų ir nustatytų vidutinių krūvininkų lokalizacijos energijos verčių.

Optiškai charakterizuotos CdZnO/ZnO daugkartinių kvantinių duobių struktūros, skirtos ties 505 nm spinduliuojantiems šviesos diodams, ir palygintos su atitinkamomis InGaN/GaN daugkartinių kvantinių duobių struktūromis. CdZnO/ZnO daugkartinių kvantinių duobių struktūrų fotoliuminescencijos intensyvumas yra dviem eilėmis mažesnis nei InGaN/GaN daugkartinių kvantinių duobių struktūrų. Išmatuotos fotoliuminescencijos gesimo trukmės CdZnO/ZnO daugkartinių kvantinių duobių struktūroms kinta nuo 30 ps iki 50 ps kambario temperatūroje ir priklauso nuo auginimo sąlygų. InGaN/GaN daugkartinėms kvantinėms duobėms išmatuotos fotoliuminescencijos gesimo trukmės yra apie 4 ns, todėl dviem eilėmis ilgesnės nei CdZnO/ZnO struktūrų. CdZnO/ZnO ir InGaN/GaN daugkartinių kvantinių duobių struktūrų, skirtų ties 505 nm spinduliuojantiems šviesos diodams, liuminescencijos savybių skirtumas negali būti priskirtas vien tik aktyviosios srities kristalinės kokybės skirtumams, kadangi vidinis kvantinis našumas yra atitinkamai 5% ir 15%. Nustatyta, kad silpnas krūvininkų lokalizacijos efektas CdZnO/ZnO daugkartinių kvantinių duobių struktūrose yra svarbi mažo emisijos efektyvumo priežastis.

1 Introduction

Zinc oxide (ZnO) is a wide band-gap semiconductor promising for applications in optoelectronics. The direct band-gap of 3.37 eV at the room temperature results in the light absorption and emission at near-UV spectral range [1]. Another unique property is extremely large exciton binding energy of 60 meV [2]. Even at room temperature with thermal energy of 26 meV, carriers in the crystal are found as Wannier-Mott type excitons. It makes this compound a convenient medium for study of the fundamental processes in high density gas of various interacting quasi-particles, such as electrons, holes, excitons and their complexes (bound excitons and biexcitons) and formation of dense electron-hole plasma exceeding Mott-density. Favorable large exciton binding energy may also lead to lower thresholds for SE [3] and higher lasing stability. Another advantage of ZnO-based compounds over competitive semiconductor groups is cheaper production as well.

ZnO as a wide-gap semiconductor is known for a long time. The first research period started at 1930s and lasted until the end of the seventies [4]. The basic crystal structural, electrical and optical properties were investigated during that time. The most sample species at that time were bulk ZnO crystals grown by gas transport or hydrothermal growth techniques. The interest to ZnO paled in the beginning of the eighties due to the p-type unavailability. This restricted the applications of ZnO in semiconductor devices. The brief overview of early research achievements can be found in a book [5].

The current research period gradually started from the 1990s and it is related with the achievements in growth techniques, namely MBE [6] and MOCVD [7], as well as in advanced characterization techniques. Recently, the number of scientific publications on (Cd,Mg)ZnO materials and their quantum structures increased significantly. The possibility to perform band-gap engineering by introducing Cd or Mg into ZnO compound brings this

reborn material frontward as one of the most promising materials in modern optoelectronics [8, 9]. MgZnO can find the application in the deep UV photodiodes, LEDs and LDs as a competitive material to nitride-based compounds. The CdZnO quantum structures can be alternative to InGaN quantum structures based blue and green light emitters. The lattice mismatch between ZnO and GaN is about 2% whereas that for ZnO and sapphire is about 18% [10]. Therefore, ZnO also is often used in combination with well established GaN technology [11]. Recent achievements in growth technology (including MBE approach) seem promising from the viewpoint of fabrication of quantum structures like nanorods [12], nanotubes [13], nano-wells [8, 14], and etc., which show enhanced light extraction efficiency.

The current research on ZnO and ZnO-based materials are mainly related with the applications in one of the following field, such as:

- UV and visible LEDs and LDs;
- solar-blind photodiodes;
- visible light transparent conducting oxides;
- solar cells;
- dilute magnetic semiconductor for spintronics;
- high radiation resistant devices for space- and nuclear-electronics;
- biosensors.

The unique properties of ZnO can be utilized in the new semiconductor devices with better performance and efficiency. However, several problems still have to be resolved before ZnO can become competitive with other semiconductor groups in optoelectronics. For ZnO applications the p and n doping is necessary. The nominally undoped ZnO epitaxial layers are n-type. Also the n-type ZnO epitaxial layers can be grown highly conductive by doping ZnO with Al, Ga or In. The p-type conductivity of ZnO epitaxial layers may be achieved by introducing N, P or As to replace the O^{2-} in the ZnO lattice [15]. On the other hand, Li, Na, K, Cu or Ag can be introduced to replace Zn^{2+} in the ZnO lattice [16]. Although there is variety of dopants available, the highly conductive stable and reproducible p-type ZnO epitaxial layers are still major issue that must be resolved. However,

some breakthrough was done by realization of co-doping of ZnO epitaxial layers [17].

Motivation

The breakthrough of GaN based semiconductor technology lasted more than two decades starting the new generation of solid-state lighting. The beginning of GaN research boom was initiated by the works of I. Akasaki group on stable and reproductive *p*-type GaN epitaxial layers [18, 19] and by the works of Sh. Nakamura on growth of high quality GaN epitaxial layers suitable for commercial violet and blue LEDs [20, 21, 22]. The impact of the research on GaN based technologies for optoelectronic was tremendous: the whole new solid-state lighting industry was established offering the vast variety of applications for semiconductor light emitting devices. Many technological problems were solved and great amount of knowledge on physics behind the light generation and extraction was acquired in the past few decades due to intense research in this field. By the way, the significant contribution is done by the scientists at Applied Research Institute of Vilnius University — more than 150 scientific papers were published in recent years (source: *Web of Knowledge*).

While the more powerful and more efficient LEDs and LDs are hitting the market, the research progress on GaN based technologies saturates with around 3000 papers each year since 2006. The ZnO based technologies however have the unrealized potential to be used in optoelectronics not only supplementing the available lighting active media, but also revealing new aspects of the fundamental recombination processes. The rapid progress of the growth, doping and processing techniques promises the ZnO based heterostructures and quantum structures of sufficient structural and optical quality for commercial optoelectronic devices in the near future. The unique properties of ZnO may offer new interesting features of light emitters. Therefore it is important and challenging to work in the area of ZnO based technologies.

Goal of the work

The goal of this work is to study ZnO, MgZnO, CdZnO heterostructures and quantum structures using advanced spectroscopy techniques and to describe the optical quality of the structures considering the relation of the crystal properties of the layers and linking to the applications in the field of optoelectronics.

Tasks of the dissertation

To reach and fulfil the stated goal of this work the following tasks were established:

1. Investigation of the MBE grown high quality undoped ZnO epitaxial layers on the sapphire substrates using spectroscopic techniques and characterization of the optical quality of the epitaxial layers linking to the crystal quality. Characterization of the MBE grown Ga doped *n*-type ZnO thin heteroepitaxial layers on various epitaxial layer structures and relate the optical properties to the structures. Optical characterization of the N doped *p*-type ZnO layers grown by magnetron sputtering to find the evidences of N caused acceptor levels, that activates *p*-type conductivity of the ZnO layers.

2. Investigation of the optical properties of the MBE grown MgZnO thin epitaxial layers on sapphire substrates and description of the influence of the Mg content in the epitaxial layers to optical properties, as well to crystal structural quality of MgZnO epitaxial layers.

3. Characterization of the CdZnO/ZnO MQWs structures for application of electrically driven green (λ_{em} = 505 nm) LEDs grown by combined MBE and MOCVD techniques; description of the optical quality of the structures relating to the growth conditions and comparing to the conventional InGaN/GaN MQWs structures for green LEDs application using spectroscopic techniques; evaluation of the main reasons that influence the optical output characteristics of the CdZnO/ZnO MQWs structures for LEDs.

Novelty and importance of the work

The ZnO based semiconductor structures for applications in the field of optoelectronics is currently in the intensive research period. The progress in the growth and doping techniques gives the possibility to fabricate ZnO based heterostructures of sufficient structural and optical quality for efficient optoelectronic devices. Therefore, the investigation of currently available ZnO based structures is of great importance. The study of carrier dynamics and fundamental interaction processes gain the necessary knowledge to overcome main technological obstacles.

In this work series of ZnO, MgZnO and CdZnO heterostructures and quantum structures were studied by the means of advanced spectroscopic techniques. The main achievements of this work lie in these findings:

The model of inelastic exciton interaction involving localized excitons is applied to calculate the P-band observed in ZnO PL spectra. The introduction of localized donor bound exciton to the interaction led to the shift of the P-band peak energy to the lower energy side. This explains the diversity of measured P-band's peak positions.

The carrier localization effect is studied in MBE grown MgZnO epitaxial layers with high (17 – 32%) Mg content in the alloys. The PL investigation revealed the double S-shaped PL peak position dependence on temperature, what is the evidence of carrier localization in randomly distributed potential field fluctuations. The double blue-shift of the PL peak position with increase of temperature is described for the first time and two blue-shifts are attributed to the separated double-scale potential field fluctuations with different average localization energy.

The PL decay time was measured for MBE grown CdZnO/ZnO MQWs structures for green LEDs, that emits at around 505 nm peak wavelength. The typical PL decay time is in the range from 30 ps to 50 ps at room temperature and depends on growth conditions of MQWs. By comparing the optical properties of CdZnO/ZnO MQWs structures with corresponding InGaN/GaN MQWs structures it is ascertained, that for efficient light emission the major influence has carrier localization effect in the active area.

Key statements for defence

The following statements are mooted as results of the accomplished work:

1. Inelastic interaction among free and localized excitons with different localization energy shifts the P-band's peak position in the photoluminescence spectra of highly excited ZnO crystals.

2. The model of two different Gaussian density-of-states tails explains the double blueshift of photoluminescence peak position in dependence on temperature.

3. Carrier lifetime and emission efficiency in CdZnO/ZnO MQWs structures designed for 505 nm LEDs is lower by two orders of magnitude in comparison to corresponding InGaN/GaN MQWs structures due to weak carrier localization effect in the active area.

Layout of the dissertation

Dissertation consists of brief introduction, 5 chapters and conclusion chapter. The introduction to the dissertation briefly describes the main idea of the work, explains the motivation behind the research, the main goal and tasks of the work, the novelty and importance of the dissertation. The key statements for defence are introduced. Also the contribution of the author and approbation of the research results are described in this chapter along with the list of publications and conference contributions.

The second chapter is devoted to review on the current breakthrough of research in the field of ZnO applications for optoelectronics with the corresponding references to the scientific literature. Together with it some of the basic knowledge about the ZnO is presented in order to build the foundation for the analysis and interpretation of the results obtained in this work. The third chapter lists and explains the techniques used in the conducted experiments. The advantages and limitations of experimental techniques are pointed out as well. The fourth chapter contains the original results of the optical properties of the undoped and doped ZnO epitaxial layers paying attention to the stimulated emission properties. The fifth chapter considers the investigation of carrier localization effects in the ternary MgZnO epitaxial layers. In the sixth chapter, the investigation on the carrier dynamics in

the CdZnO/ZnO MQWs structures is considered. The last three chapters, namely the fourth, fifth and sixth, contain the original experimental data, analysis, interpretation of the results and validation combining with the known models of semiconductor physics. The last chapter states the main results of this work.

Contribution of the author

The author's major contribution to this work is the implementation and application of stationary and quasi-stationary PL and streak camera experiments. Also the author dealt with the data acquisition, analysis, visualization and interpretation. The modelling results presented in this work are accomplished by the author using the numerical calculation methods. The results and conclusions are achieved by the author discussing the matter with the supervisor of the doctoral studies prof. dr. Edmundas Kuokštis.

The author has major contribution to preparation of the publications [23, 24]. In the paper [25], the author contributed the PL results and discussion. The author's results are included in the publications [26, 27]. The author has prepared number of presentations in the conferences: six poster and five oral presentations. The author gratefully acknowledges the contribution of the co-authors to the publications and conference papers.

However, this work would not be possible without the contribution of the researchers at Institute of Photonics and Optoelectronics of National Taiwan University. The samples growth and preparation was done by research group of prof. dr. Chih-Chung Yang with dr. Shao-Ying Ting and dr. Jeng-Jie Huang. The N-doped ZnO samples were grown by dr. Saulius Burinskas at Kaunas University of Technology. The Ga-doped samples were grown by dr. Huiyong Liu and dr. Vitaliy Avrutin at Virginia Commonwealth University. The integral form of excitons' interaction with Dirac δ wave-function was derived by prof. dr. Egidijus Anisimovas at Department of Theoretical Physics of Vilnius University.

Approbation of the research results

The significant part of the research results discussed in this work is published in the periodical peer-reviewed scientific journals working with the co-authors of the papers. Also the segments of the research were presented in number of international and national conferences as part results. The list of publications and conference contributions related to the doctoral dissertation is given below. Several publications that are not related directly by subject to the doctoral dissertation are also listed separately in the third section.

List of publications related to the dissertation

1. M. Karaliūnas, V. Šukauskas, E. Kuokštis, S.-Y. Ting, J.-J. Huang, and C.-C. Yang, Band tail filling effect in MBE-grown ternary MgZnO epitaxial layers with high Mg content, Phys. Status Solidi C **10**(10), 1265 (2012).

2. M. Karaliunas, T. Serevicius, E. Kuokstis, S. Jursenas, S.-Y. Ting, J.-J. Huang, and C.-C. Yang, Optical Characterization of MBE-grown ZnO Epilayers, Advanced Materials Research **222**, 86 (2011).

3. S. Burinskas, J. Dudonis, D. Milčius, M. Karaliūnas, and E. Kuokštis, Synthesis of ZnO:N thin films by reactive DC magnetron sputtering, Lith. J. Phys. **50**(3), 325 (2010).

4. E. Kuokštis, M. Karaliūnas, S. Juršėnas, S. Miasojedovas, T. Serevičius, S.-Y. Ting, J.-J. Huang, and C.-C. Yang, Photoluminescence studies of MBE-grown ZnO and MgZnO epitaxial layers, Phys. Status Solidi C **6**(12), 2668 (2009).

5. M. Karaliūnas, E. Kuokštis, K. Kazlauskas, S. Juršėnas, V. Hoffmann, and A. Knauer, Optical gain dynamics in InGaN/InGaN quantum wells, Proc. SPIE **7142**, 71420U (2008).

6. V. Hoffmann, A. Knauer, F. Brunner, C. Netzel, U. Zeimer, S. Einfeldt, M. Weyers, G. Tränkle, J. M. Karaliunas, K. Kazlauskas, S. Jursenas, U. Jahn, J.R. van Look, and M. Kneissl, Influence of MOVPE

growth temperature on the structural and optical properties of InGaN MQW laser diodes, J. Cryst. Growth **310**, 4525 (2008).

List of conference contributions related to the dissertation

1. E. Kuokštis, M. Karaliūnas, M. Stasiūnas, S.-Y. Ting, J.-J. Huang, and C.-C. Yang, Optical Properties of CdZnO/ZnO Multiple Quantum Wells for Optoelectronic Application, Poster S1-65. 40th Lithuanian National Physics Conference (LNFK-40), 10-12th June 2013, Vilnius, Lithuania.

2. E. Kuokštis, V. Šukauskas, M. Karaliūnas, S. Marcinkevičius, V. Liuolia, S.-Y. Ting, J.-J. Huang, and C.-C. Yang, Investigation of MgZnO Epitaxial Layers as Active Media for Applications in Optoelectronics, Poster S1-64. 40th Lithuanian National Physics Conference (LNFK-40), 10-12th June 2013, Vilnius, Lithuania.

3. H. Liu, M. Karaliunas, V. Celedinas, K. Jarasiunas, V. Avrutin, N. Izyumskaya, M. Reshchikov, Ü. Özgür, and H. Morkoç, Optical Properties of Highly Conductive and Transparent GZO Grown by Molecular Beam Epitaxy, Oral presentation Z14.08. 2012 MRS Fall Meeting & Exhibit, November 25-30, 2012, Boston, MA, U.S.A.

4. M. Karaliūnas, V. Šukauskas, E. Kuokštis, S.-Y. Ting, J.-J. Huang, and C.-C. Yang, Band tail filling effect in MBE grown ternary MgZnO epitaxial layers with high Mg content, Poster 76. The 7th International Workshop on Zinc Oxide and Related Materials (IWZnO-2012), 11-14th September 2012, Nice, France.

5. M. Karaliūnas, M. Stasiūnas, E. Kuokštis, S.-Y. Ting, J.-J. Huang, and C.-C. Yang, Photoluminescence Dynamics of CdZnO/ZnO Quantum Structures, Poster S1-40. 39th Lithuanian National Physics Conference (LNFK-39), 6-8th October 2011, Vilnius, Lithuania.

6. M. Karaliūnas, V. Tumas, E. Kuokštis, and E. Anisimovas, Exciton-Exciton Interaction Models in ZnO, Oral presentation O3-2. International Conference Advanced Optical Materials and Devices (AOMD-7), August 28 – 31 2011, Vilnius, Lithuania.

7. M. Karaliūnas, V. Šukauskas, T. Serevičius, E. Kuokštis, S.-Y. Ting, J.-J. Huang, and C.-C. Yang, The Band Tail Filling Effects in Ternary MgZnO Epitaxial Layers, Poster P58. The 13-th International Conference - School Advanced Materials and Technologies, 27-31 August 2011, Palanga, Lithuania. ISSN 1822-7759.

8. M. Karaliūnas, E. Kuokštis, K. Y. Chen, S. Y. Ting, J. J. Huang, C. H. Liao, C. Y. Chen, and C. C. Yang, Photoluminescence Properties of InGaN/GaN and CdZnO/ZnO Multiple Quantum Wells for Light-Emitting Diodes, Oral presentation. 16th Semiconducting and Insulating Materials Conference (SIMC-XVI), June 19-23, 2011, Stockholm, Sweden.

9. M. Karaliūnas, Photoluminescence decay time study of CdZnO/ZnO and InGaN/GaN QWs LED structures, Oral presentation. The Internships of PhD students in Foreign Science Centres. March 17, 2011, Vilnius, Lithuania.

10. M. Karaliūnas, E. Kuokštis, S.Y. Ting, J.J. Huang, and C.-C. Yang, Optical Properties of CdZnO Multiple Quantum Wells, Poster P68. The 12-th International Conference "Advanced Materials and Technologies" and Summer School "European Doctorate in Physics and Chemistry of Advanced Materials", 27-31 August 2010, Palanga, Lithuania. ISSN 1822-7759.

11. M. Karaliūnas, T. Serevičius, E. Kuokštis, S. Juršėnas, S. Y. Ting, J. J. Huang, and C.-C. Yang, Optical Characterization of MBE-grown ZnO Epilayers, Oral and poster presentation. The 9th International Conference on Global Research and Education, August 9-12, 2010, Riga, Latvia.

12. M. Karaliūnas, E. Kuokštis, S. Y. Ting, J. J. Huang, and C.-C. Yang, Stimulated Emission Study in MBE-Grown ZnO Epilayers, Poster TuP62. XXXIX "Jaszowiec" 2010 International School and Conference on the Physics of Semiconductors, June 19-24, 2010, Krynica-Zdrój, Poland.

13. M. Karaliūnas and E. Kuokštis, Optical Gain Coefficient Spectra in

MBE-Grown ZnO Epilayers, Oral presentation. International Conference of Young Scientists, April 29-30, 2010, Šiauliai, Lithuania.

14. M. Karaliūnas, P. Ščajev, and K. Jarašiūnas, Room Temperature Photoluminescence Spectra in Bulk 3C-SiC Crystals, Poster P39. The 11-th International Conference-School Advanced Materials and Technologies, 27-31 August 2009, Palanga, Lithuania. ISSN 1822-7759.

15. M. Karaliūnas, E. Kuokštis, S. Juršėnas, S. Miasojedovas, T. Serevičius, S.-Y. Ting, J.-J. Huang, and C.-C. Yang, Photoluminescence studies of MBE-grown ZnO and MgZnO epiaxial layers, Oral presentation. 15th Semiconducting and Insulating Materials Conference (SIMC-XV), June 15-19, 2009, Vilnius, Lithuania.

16. M. Karaliūnas, E. Kuokštis, S.-Y. Ting, J.-J. Huang, and C.-C. Yang, Optical Gain in MBE-Grown ZnO Layers, Poster S1-38. 38th Lithuanian National Physics Conference (LNFK-38), 8-10th June, 2009, Vilnius, Lithuania.

Publications not included in the dissertation

1. P. Ščajev, M. Karaliūnas, E. Kuokštis, and K. Jarašiūnas, Radiative and nonradiative recombination rates in cubic SiC, J. Lumin. **134**, 588 (2013).

2. P. Ščajev, P. Onufrijevs, G. Manolis, M. Karaliūnas, S. Nargelas, N. Jegenyes, J. Lorenzzi, G. Ferro, M. Beshkova, R. Vasiliauskas, M. Syväjärvi, R. Yakimova, M. Kato, and K. Jarašiūnas, On applicability of time-resolved optical techniques for characterization of differently grown 3C-SiC crystals and heterostructures, Material Science Forum **711**, 159 (2012).

3. M. Karaliūnas, P. Vitta, A. Žukauskas, A. Zahnd, D. Bista, B. B. Chhetri, and M. R. Updhyaya, Characterization of Nepali Solid-state Lamps, Electronics and Electrical Engineering **89**(1), 29 (2009).

2 General properties of ZnO related materials and applications in optoelectronics

In this chapter, the general properties of ZnO is reviewed paying more attention to the aspects that are important for further discussions regarding the results obtained in this work. A brief overview of recent achievements in application of ZnO related materials in optoelectronics is included with the intention to accumulate the interest in the field of ZnO research.

The research on ZnO and related materials, as well the research involving ZnO as component for other cutting-edge technologies, is currently booming. According to C. Klingshirn's review on ZnO published in 2007 [4], over the last few years the renaissance in the research field of ZnO occurred starting from the mid of 1990s. Indeed, the number of publications found in the database for scientific literature "ISI Web of Knowledge" with the keyword "ZnO" rapidly increases, as it can be seen in Fig. 2.1. The number of publications grown more than 3 times from 2004 until 2011 reaching more than 6500. Besides, if compare to the GaN related publications number of $\sim$ 3300 in 2011, there was 2 times more ZnO publications published. The ZnO is considered the main rival of GaN in applications for optoelectronic devices.

On the other hand in Fig. 2.2 the numbers of publications found with the keywords "ZnO" and "GaN" in the database of the journal "Applied Physics Letters" are depicted with time. It is a weekly journal that features concise, up-to-date reports on significant new findings in applied physics and it is highly appreciated in the community of scientist in the area of

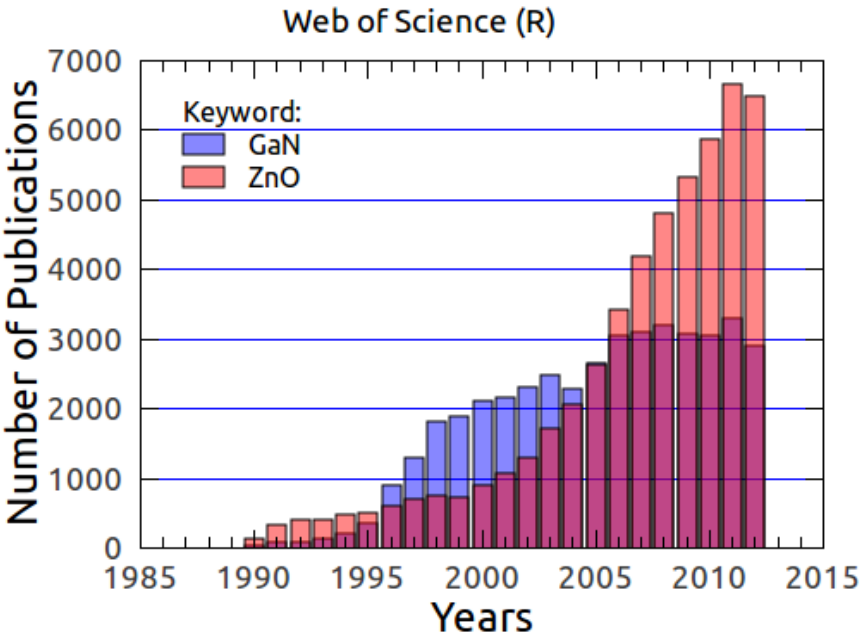

Figure 2.1: Number of publications found using the keywords "ZnO" and "GaN" distribution over the time. (Source: *Thomson Reuters / Web of Science*)

material physics. We can see the rapid increase of ZnO related publications number from 2000 to 2006. However, the GaN related research remains more relevant subject in the last decade for applied physics.

A revival of ZnO research was initiated in the late nineties basically due to the optically pumped lasing at room temperature in ZnO epilayers [28] relating this effect to inelastic exciton-exciton interaction with induced optical gain spectra [29]. It was demonstrated the electrically driven homoepitaxial ZnO-based *p-i-n* LED [30]. Very recently, the life-time of ZnO-based LEDs of 6.8 hours was reported [17]. The current breakthrough on ZnO material system is largely related to improved MBE and MOCVD growth techniques, that is the possibility to make quantum structures by accomplishing band gap engineering by adding Cd or Mg to ZnO compound.

2.1 Basic structural properties of ZnO

ZnO is a wide direct-gap II-VI semiconductor of preferable hexagonal wurtzite type crystal structure shown in Fig. 2.3(a). Other possible crystal lattice types for ZnO are cubic zinc blende shown in Fig. 2.3(b) and cubic rocksalt

shown in Fig. 2.3(c). A cubic zinc blende ZnO can be grown on the suitable cubic lattice type substrates. For example, the ZnO epitaxial growth on GaAs (001) substrates using ZnS buffer layer resulted polycrystalline films of zinc blende lattice with the lattice constant $a = 4.463$ Å[31]. The zinc blende ZnO has small practical value for applications due to the lack of phase stability. The epitaxially grown zinc blende ZnO thin films tend to relax forming hexagonal wurtzite ZnO inclusions [32]. A cubic rocksalt ZnO is stable only at high ambient pressure, therefore it has even less practical value in the sense of applications for semiconductor devices.

An ideal wurtzite crystal structure has a hexagonal unit cell with two lattice parameters a and c in the ratio of $a/c = \sqrt{8/3} = 1.633$. The u parameter, which is defined as the bond parallel to the c-axis length b divided by lattice parameter c, in an ideal wurtzite structure is $u = 3/8 = 0.375$. The measured lattice parameters for ZnO are close to ideal values: $a/c = 1.602$ and $u = 0.382$ [5]. This implies to the fact that ZnO is a hard and robust material of high density.

Due to small unit-cell volume and large band gap energy ZnO exhibit high radiation hardness with high threshold displacement energy [33]. Compar-

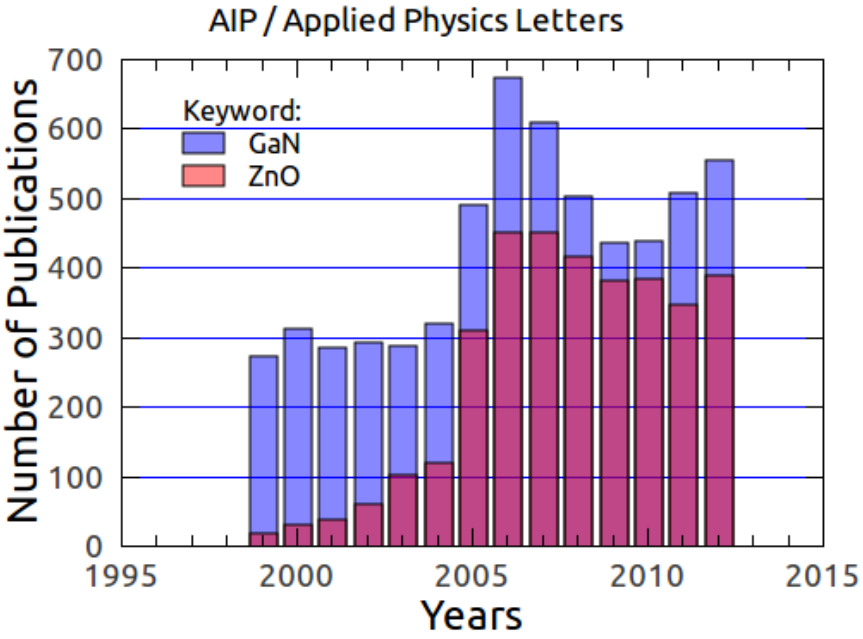

Figure 2.2: Number of papers in the journal "Applied Physics Letters" distribution over the time. (Source: *apl.aip.org*)

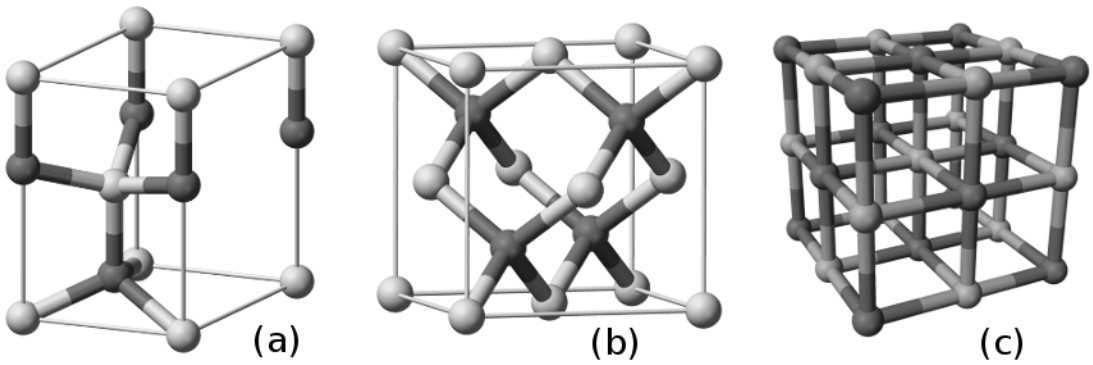

Figure 2.3: Unit cells of possible ZnO crystal lattice types: (a) hexagonal wurtzite, (b) cubic zinc blende, and (c) cubic rocksalt, which exists only in high pressure ambient conditions. (Source: *wikipedia.org*)

ing to Si, GaAs, and GaN, ZnO is more resistant to particle irradiation. The reported damage threshold values are around 1.5 MeV and the threshold this high can not be explained by the creation of simple vacancy-interstitial (Frenkel) pairs, but must involve "chains" of defects [34].

The energy band diagram in the vicinity of fundamental band gap of ZnO is depicted in the Fig. 2.4. The conduction band is formed essentially from the 4s orbitals of Zn^{2+} ions and the upper valence band is formed from the 2p states of O^{2-} with an admixture of Zn^{2+} 3d levels. The valence band of ZnO splits due to the hexagonal crystal field and the spin-orbit coupling into three sub-bands labelled A, B and C from higher to lower energy [35]. The usual valence bands ordering for wurtzite semiconductors is A Γ_9, B Γ_7, and C Γ_7. It means that in most cases the spin-orbit splitting is larger than the crystal field splitting [4]. In the case of ZnO however, valence band ordering differ from the wurtzite semiconductors due to the negative spin-orbit coupling. The ordering of the valence bands is A Γ_7, B Γ_9, and C Γ_7, while the conduction band has the Γ_7 symmetry [36]. This imposes selection rules for optical transitions as indicated in Fig. 2.4. The transitions from the two upper A Γ_7 and B Γ_9 valence bands to the Γ_7 conduction band are allowed only for $\vec{E} \perp \vec{c}$ and transitions from the C Γ_7 valence band are allowed only for $\vec{E} \parallel \vec{c}$. Therefore, if the ZnO epitaxial layers are *c*-axis oriented, the oscillator strength of the C exciton is found to be small compared to the oscillator strength of A and B excitons [36]. The energy difference between A and B valence bands $\Delta E_{AB} = 5$ meV and between B

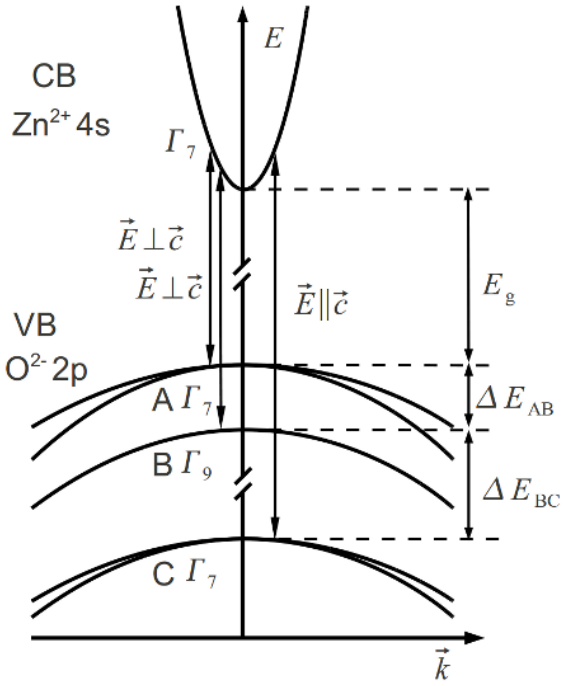

Figure 2.4: ZnO band structure in the vicinity of the Γ point. The conduction band (CB) is of Γ_7 symmetry. The inverted ordering of valence bands (VB) is: A Γ_7, B Γ_9, and C Γ_7. The energy $E_g = 3.4376$ eV, $\Delta E_{AB} \simeq 4.9$ meV, and $\Delta E_{BC} = 43.7$ meV. The C valence band splitting for heavy holes (HH) with the effective mass $0.55m_0$ and for light holes (LH) with the effective mass $0.31m_0$ is represented. [4, 15]

and C $\Delta E_{BC} = 44$ meV [15].

As it was mentioned before, exciton binding energy in ZnO is 60 ± 1 meV [2, 35]. It is uniquely large if compare to other semiconductors. The exciton binding energy of various semiconductors is plotted in the Fig. 2.5 as a function of band gap energy. The recent theoretical study suggests that a substantial ionic bonding in ZnO is responsible for this phenomena [37]. Note, that III-V group semiconductors has substantial covalent bonding. On the other hand, the insulator MgO with the band gap of 7.8 eV [9] has completely ionic bonding [4]. The exciton binding energy in MgO was measured as high as 145 ± 25 meV [38, 39]. Therefore, the stronger localization of conductive and valence band edge states on ion sites leads to enhanced electron-hole interaction [37].

The exciton binding energy can be increased significantly in the MQWs structures. In the $ZnO/Zn_{0.73}Mg_{0.27}O$ MQWs with the well width of 1.29 nm

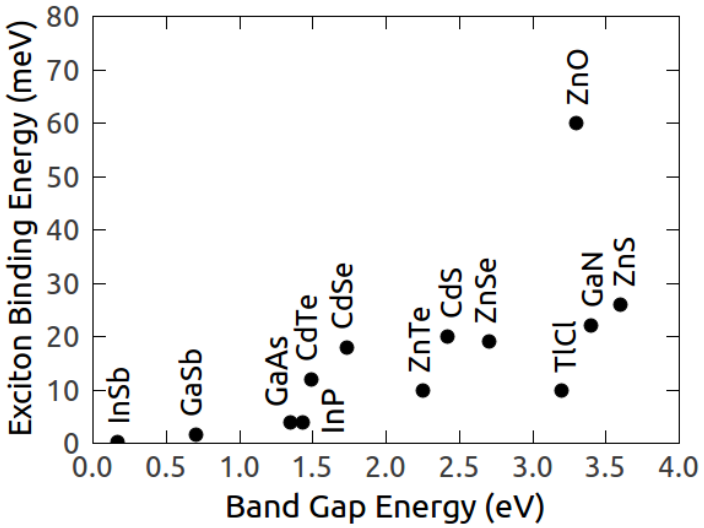

Figure 2.5: Exciton binding energy versus band gap energy of various semiconductors.

the exciton binding energy reaches 115 meV, almost double that of bulk ZnO [40]. Also the biexcitons binding energy was enhanced more than two times than in bulk ZnO up to 30.9 meV in the ZnO/$Zn_{0.74}Mg_{0.26}O$ MQWs structures with the well width of 1.75 nm [14].

2.2 Band gap engineering

The fundamental band gap of ZnO results the NBE emission at near UV spectral range, that is around 3.31 eV photon energy or 374.5 nm wavelength at room temperature. However, the essential prerequisite for material to be used in optoelectronics is the feasibility to realize the band gap engineering. In the case of ZnO, this can be achieved by alloying ZnO with CdO or MgO for narrowing or widening its band gap, respectively [8, 9, 41]. It allows the band gap variation of (Cd,Mg)ZnO compound semiconductor in the range from 2.8 to 4 eV ensuring the wurtzite structure of epitaxial layers [42]. The band gap engineering paves the way for LEDs and laser diodes of any peak wavelength around the fundamental emission of host material.

At present, the light emitting diodes cover whole visible spectral range and is widely used as a monochromatic light sources as well in white light lamps. The violet, blue and green LEDs are made of GaN material group alloying with the In, and yellow, orange and red LEDs are made of (Al,Ga)InP

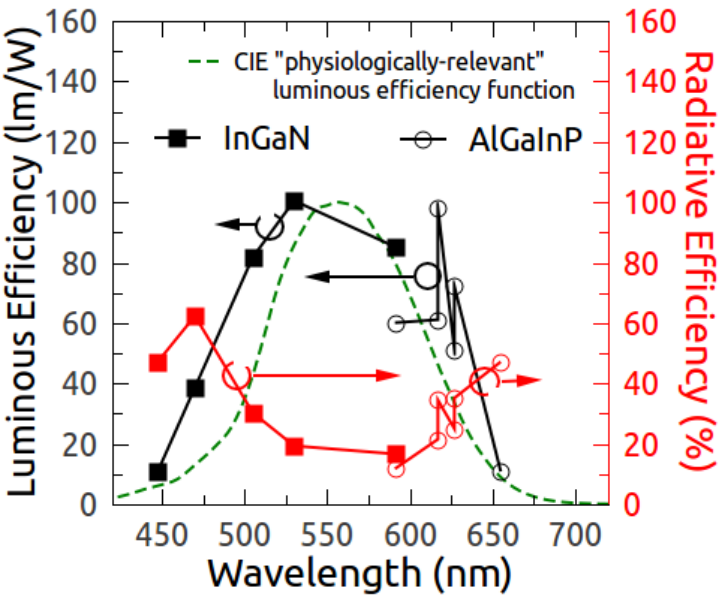

Figure 2.6: Luminous and radiative efficiency dependence on wavelength. The solid dots denote the InGaN based commercially available LEDs' efficiency and open dots denote the AlGaInP based commercially available LEDs' efficiency. The line shows the CIE "physiologically-relevant" luminous efficiency function, or the human eye sensitivity function. [43]

material group. However, there still is a problem with emission efficiency of LEDs in the green spectral range.

In Fig. 2.6 the radiative and luminous efficiency of the most efficient commercial available LEDs up to date is depicted as a function of dominate emission wavelength [43]. Although the green LEDs look bright for human eye, the radiative efficiency is significantly lower if compare to red and blue LEDs. The reason is that human eye sensitivity to light function $V(\lambda)$ peaks at 555 nm wavelength. There is a lack of efficiently radiative semiconductors in that particular spectral range. As it can be seen in Fig. 2.7, the spectral range around 505 nm emission wavelength is well covered by (Al,Ga)InP, (Al,In)GaN and (Mg,Cd)ZnO material groups.

In Fig. 2.7, the band gap energy dependence on lattice constant is depicted for semiconductor groups with high importance in optoelectronics [44]. The emission of radiative host semiconductors, namely InP, GaN and ZnO, is shifted to IR or UV side of the spectrum. Indeed, the problem arises due to the diversity of material properties. For example, InP has a zinc-blende crystal structure and has perfect match with the AlGaAs and

Si crystal lattice constant. It is direct gap material and is primarily used for optical-fibre communications in the long-wavelength region [45]. However, the semiconductors for alloying the InP towards the green spectral range are AlP and GaP. Even if these semiconductors have the same zinc-blende crystal structure, they have indirect band gap structure [44]. The indirect band gap semiconductors are very poor light emitters.

Both MgO and CdO are of NaCl type cubic or rocksalt crystal structure. Despite the thermodynamical Mg solid solubility in ZnO limit to only 2% maximum [42], for the thin film alloys grown under metastable conditions MgO solid solubility in ZnO is 33 mol% [46]. Above this molar part of Mg in the alloys the phase separation can occur with high probability. However, recent achievements in the growth process optimisation led to the single phase wurtzite structure MgZnO epitaxial layers with 55% of Mg in the alloy [47].

For alloying the CdO with ZnO, the thermodynamical solid solubility is limited up to 2% maximum at thermal equilibrium conditions [48]. However, under metastable growth conditions, the Cd concentration up to 30% can be achieved resulting the ability to tune the energy gap of CdZnO through the visible range from 380 to 620 nm wavelength [49].

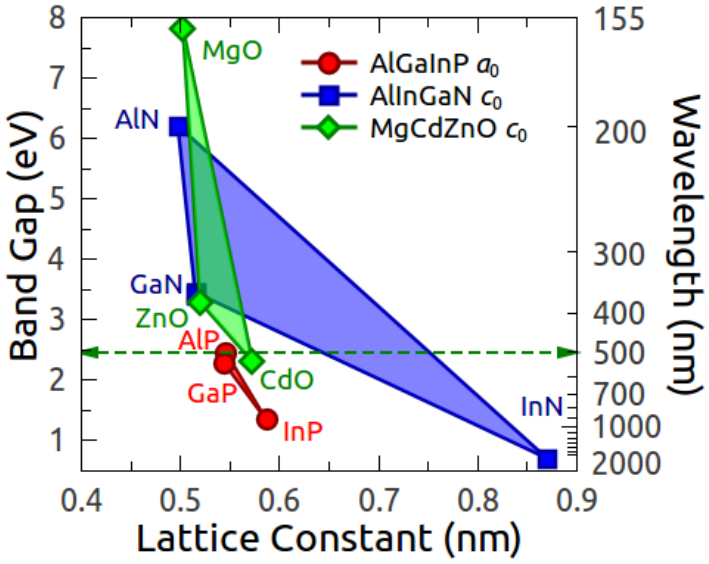

Figure 2.7: Band gap energy dependence on lattice constant for AlGaInP, AlInGaN, and MgCdZnO material groups. The dashed horizontal line marks the band gap energy equivalent to green light emission at 505 nm wavelength.

2.3 Growth of ZnO-based heterostructures

The most common substrate used for growth of ZnO epitaxial layers is a sapphire (Al_2O_3) with various its crystallographic orientations. Despite the fact that lattice mismatch between Al_2O_3 and ZnO is about 18% [10], the ZnO epitaxial layers on sapphire substrates are of sufficient crystal quality for optoelectronic devices [50].

Because of the smaller lattice mismatch between ZnO and GaN (1.8%) the latter material is considered to be as a buffer layer for ZnO [4]. For exceptional good quality structures ZnO can be grown on the lattice matched SCAM substrates [36]. The hydrothermal growth technique allows to produce large volume ZnO crystals that can be used as substrates for the homoepitaxy growth.

Molecular beam epitaxy

The ultra-high vacuum of around 5×10^{-10} torr is necessary for the growth in the MBE chamber. For MBE growth the slow deposition rate typically less than 1000 nm per hour is the key issue. The slow deposition rate require the higher vacuum conditions to achieve the same impurity levels as thous of other deposition techniques [51].

A typical MBE system has three chambers: load-lock chamber, preparation chamber, and growth chamber. In the preparation chamber the substrates are thermally cleaned. Prior to growth, the substrates are exposed to an oxygen plasma. The oxygen plasma treatment is expected to act as a further cleaning step and is necessary to guaranty an oxygen-terminated surface [50].

In the growth chamber, a thin film crystallizes via the reaction among thermally energized molecular (or atomic) beams of the constituent elements on the substrate surface. In contrast to MOCVD, which is operated near the thermodynamic equilibrium, MBE growth is governed mainly by the kinetics of the molecular beams reacting with the crystalline surface [52].

For the growth of ZnO-related compounds, the metal fluxes of solid species Zn, Mg, and Cd are evaporated from the Knudsen-cells. The beam equivalent pressure of a solid source is measured by the beam flux mon-

itor ion gouge. The temperature of the Knudsen-cells are controlled by proportional-integral-derivative temperature controllers. For active oxygen source the radio-frequency oxygen plasma is generated in the growth chamber. When the O_2 plasma is used, the chamber vacuum during the growth is typically of 10^{-5} torr [51]. The Si, and GaP Knudsen-cells are used for the n-type and p-type doping, respectively.

Metalorganic chemical vapour deposition

MOCVD, or sometimes called metal-organic vapour phase epitaxy (MOVPE), is a growth method especially suitable for compound semiconductors. The MOCVD technique is based on the chemical reaction of the vapour or gas molecules on the heated substrate surface. The vapours from the sources are transported to the reaction zone with a carrier gas flow [53].

For the ZnO growth, the MOCVD technique typically involves the use of metal alkyls, usually dimethylzinc ($(CH_3)_2Zn$, DMZn) or diethylzinc ($(C_2H_5)_2Zn$, DEZn) in combination with a seperate source of oxygen, and argon as a carrier gas [51]. The chemical reactions takes place during growth process with DEZn, which is a very reactive electron deficient compound with two vacant orbitals.

1. Growth with oxygen:

$$(C_2H_5)_2Zn + 7O_2 \rightarrow ZnO + 4CO_2 + 5H_2O.$$

2. Growth with H_2O:

$$(C_2H_5)_2Zn + 2H_2O \rightarrow Zn(OH)_2 + 2C_2H_6,$$
$$Zn(OH)_2 \rightarrow ZnO + H_2O.$$

3. Growth with CO_2:

$$(C_2H_5)_2Zn + 2CO_2 \rightarrow (C_2H_5COO)_2Zn,$$
$$(C_2H_5COO)_2Zn \rightarrow ZnO + \text{gaseous products}.$$

The following reaction has been proposed in the case of DMZn with CO_2:

$$(CH_3)_2Zn + 2CO_2 \rightarrow (CH_3COO)_2Zn.$$

Zinc acetate can then react with water according to the following reaction to form ZnO:

$$(CH_3COO)_2Zn + H_2O \rightarrow ZnO + 2CH_3COOH.$$

Other reactions for the growth of MgO, CdO and their alloys are all the same except the Zn is replaced with other II-group element.

Magnetron sputtering

Physical sputtering is driven by momentum exchange between the ions and atoms in the materials due to collisions. The sputtering technique has many advantages, such as low cost, simplicity, high deposition rate (about 1 µm per hour).

The most popular growth technique for early ZnO investigations was sputtering method. ZnO films can be grown at a certain substrate temperature by sputtering from a high-purity ZnO (99.99%) target using RF magnetron sputtering system. The growth is usually carried out in the ambient with $O_2/Ar + O_2$ ratio ranging from 0 to 1 at a pressure in the range from 10^{-3} to 10^{-2} torr. O_2 serves as the reactive gas and Ar acts as the sputtering enhancing gas. The RF power applied to the plasma can be tuned for example from 150 to 300 W at the frequency 13.56 MHz to regulate the sputtering yield rate from the ZnO target. As it was shown, this can change structural properties of ZnO films significantly [54].

ZnO can also be grown by DC sputtering from a Zn target in the $Ar + O_2$ gas mixture. Fig. 2.8 shows schematic diagram of DC sputtering system at Kaunas University of Technology [25].

2.4 Optical properties of ZnO and related materials

2.4.1 Inelastic exciton-exciton interaction transition

Due to high exciton binding energy in ZnO, the experimental observation of the excitons inelastic collision caused PL band is evident even at room temperature. This PL band, called as *P*-band, was first described in the CdS crystal at cryogenic temperature as early as 1969 [56]. The schematic

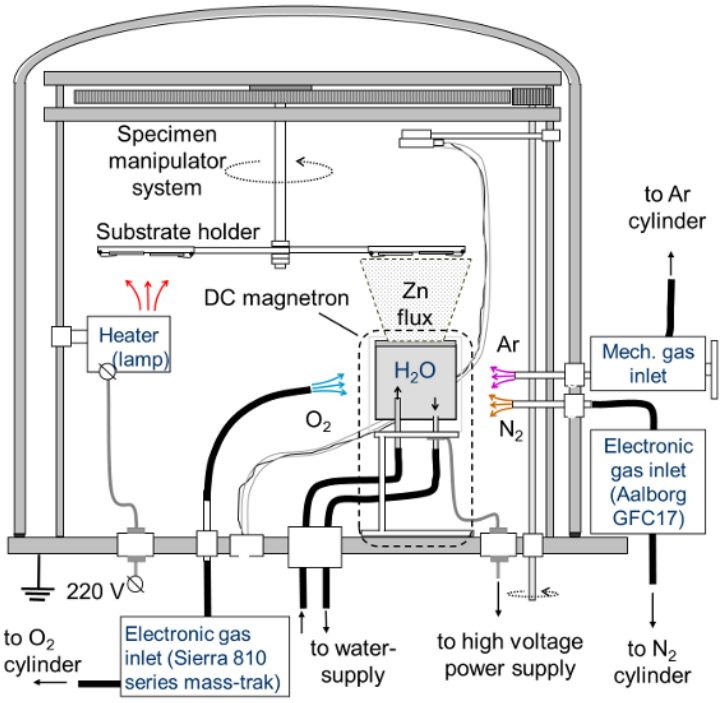

Figure 2.8: Schematic drawing of the DC magnetron sputtering chamber with the main components: magnetrons with the different metal cathodes; quartz crystal film deposition monitor; inlets for gas, water coolant, high voltage and motion; electrical motor controls sample manipulation system. [55]

drawing of the inelastic exciton-exciton interaction is shown in the Fig. 2.9. Two excitons with the wave vectors $\vec{K}$ and $\vec{K}'$ in their initial 1S states inelastically interact with each other. As a result one exciton produces the photon with the energy $h\nu$ and the other reaches the final continuum state, where the exciton is dissociated to free electron and hole with the wave vectors $\vec{k}$ and $\vec{\overline{K}}$, respectively.

There are few important features, that are the footprints of P-band in the PL spectrum. First, the P-band is not present at low excitation and it appears at particular excitation power density, which is the threshold excitation power density P_{th}^{P}. Second, the P-band's peak position is twice of exciton binding energy below the band gap. If we consider the energy of two interacting excitons before the collision E_{ex} and E'_{ex} as

$$E_{ex} = E'_{ex} = E_g - E_x^b, \tag{2.1}$$

where E_g is the band gap energy and E_x^b is the exciton binding energy. Then

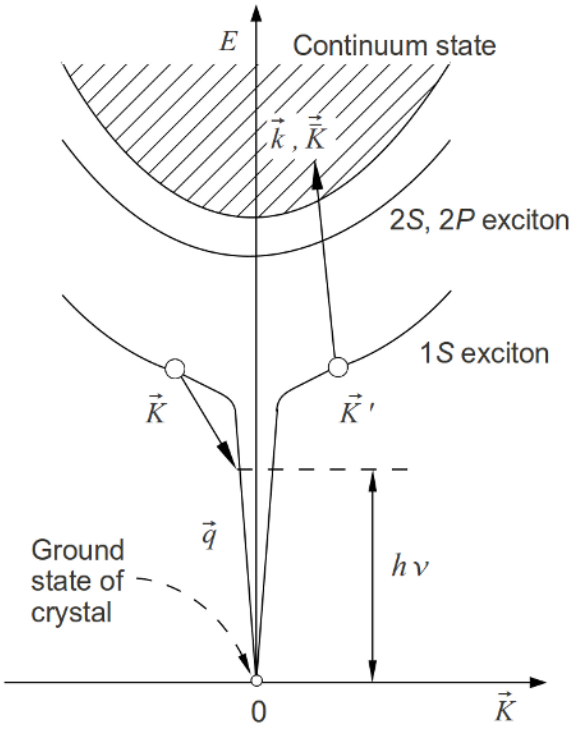

Figure 2.9: Schematic drawing of the inelastic exciton-exciton collision. The wave vectors $\vec{K}$ and $\vec{K}'$ refer to excitons in 1S states. The wave vectors $\vec{k}$ and $\vec{K}$ refer to electron and hole final states, respectively. [4, 57]

after applying the energy conservation principle the emitted photon energy is

$$h\nu = E_g - 2E_x^b - \frac{3}{2}k_B T, \tag{2.2}$$

where the last term of the formula is the average kinetic energy of electron-hole pair. Third of the features is the P-band's intensity proportionality to the square of the exciton density when the excitation power is increased. It is because the spontaneous emission rate increases in proportion to the square of the free-exciton density. Therefore the amplitude of the optical gain is proportional to square of exciton density as well [58].

Many experimental results show the appearance of P_2-band prior to the P-band with the increase of excitation power [59, 60]. This happens when the transition of another exciton to the excited bound state (2S) is much stronger than that to dissociated states in low-carrier density state [61]. Therefore the energy shift of the P-band's peak position can occur. Considering the excitation of exciton to higher excited states the energy of the

resulting photon after collision is given by

$$P_n = E_{ex} - E_x^b \left(1 - \frac{1}{n^2}\right) - \frac{3}{2} k_B T \, (n = 2, 3, 4 \cdots, \infty), \tag{2.3}$$

where P_n is the photon energy, E_{ex} is the free-exciton emission energy, n is the quantum number of the envelope function, and $k_B T$ is the thermal energy. The calculated values for emission photons of the interacting excitons to first several excited states and to the continuum are listed in the Table 2.1. Therefore the maximum peak shift $(P_\infty - P_2)$ of 15 meV can be expected.

Table 2.1: Theoretical values of emitted photon energy after inelastic collision of two 1S state excitons calculated using relation (2.3). The exciton binding energy $E_x^b = 60$ meV and $E_{ex}^A(8\text{ K}) = 3.3771$ eV and $E_{ex}(295\text{ K}) = 3.31$ eV. The quantum number n is of the final state of remaining exciton after collision.

P-band	P_2	P_3	P_4	P_5	...	P_∞
Photon energy at 8 K (eV)	3.331	3.323	3.320	3.319		3.316
Photon energy at 295 K (eV)	3.24	3.23	3.23	3.23		3.22
Final exciton state n	2	3	4	5		∞

Other deviation from theory is the experimentally measured proportionality coefficient of P-band's intensity to the excitation power β. According to A. Yamamoto *et al.* [10], possible explanations for reduced slope β are as follows: (i) the PL band due to bound excitons overlaps with the M-band; (ii) in general, when the excitation density is increased, the slope of FX–1LO band decreases from 1 to 0.5, so if the slope becomes 0.75, the slope of the M-band would be $0.75 \times 2 = 1.5$; (iii) the excitons are scattered and annihilated by other particles, such as other biexcitons, excitons, bound excitons, what also leads to reduction of the dependence coefficient β [4].

The assumptions made for biexcitonic M-band are correct for P-band as well. Moreover, the scattering of excitons may occur due to the interaction with free carriers, electrons and holes. The scattering of excitons by both point and extended defects influences not only the slope of P-band's intensity dependence on excitation density but also the P-bands threshold excitation density. Therefore, the P_{th}^P is closely related with crystal quality

and may be the quantitative property for ZnO structural quality [62].

The excitons inelastic interaction is the process that can be easily stimulated. The ZnO lasing based on exciton-exciton scattering at room temperature was demonstrated [28]. The threshold excitation power density for P-band stimulation was measured as 240 kW/cm^2. Using the VSL technique, the positive OG spectrum was measured with the peak value of 170 cm^{-1} at the excitation density of 220 kW/cm^2 at the 3.16 eV photon energy [29]. The specific features of P-band's stimulated emission is the stability of peak position with increase of excitation power density and the symmetrical shape of the line as well as of the OG spectrum.

If the excitation power density is increased further, the P-band disappears due to the screening effects of Coulomb interaction due to the high density of photogenerated carriers. The transition carrier density from the excitons to the free carrier plasma, or EHP, is called Mott density. Using the Debye-Hückel screening length, the Mott density in ZnO at RT is given by

$$n_M = \frac{k_B T}{2a_B^3 E_x^b} \approx 3.7 \times 10^{19}\,\mathrm{cm}^{-3}, \tag{2.4}$$

where $a_B = 18$ Å is the exciton Bohr radius and $E_x^b = 60$ meV is the exciton binding energys of ZnO [29]. Usually, at such density the conditions for stimulated emission of EHP are already fulfilled. Therefore the Mott transition in good quality ZnO crystal is evident as the gradual changeover from stimulated P-band to the stimulated EHP band in PL spectra dependence on excitation power density.

2.4.2 Excitonic molecule transition

Similarly to the P-band, in high quality ZnO crystals under elevated optical excitations at low temperature the emission band arises. This band is attributed to optical transition of excitonic molecules, or biexcitons, and is known as M-band. The M-band appears at 3.350 eV photon energy above the excitation power density threshold as low as $P_{th}^M = 100$ W/cm^2 at liquid nitrogen temperature [63]. The P_{th}^M closely depends on crystal quality and may be the quantitative property for ZnO structural quality. The intensity of M-band superlinearly increases with the excitation power density $I_M \propto P_{exc}^2$. However, experimentally obtained dependence rates are

around 1.5 as the M-band overlaps with the PL bands of other radiative mechanisms with lower dependence rates [10].

The early study of excitonic molecule transition by means of excitation spectroscopy at 1.7 K temperature deduced the excitonic molecule energy to $E_M = 6.740$ eV and binding energy $E_{xx}^b = 12$ meV [64]. The M-band emission in ZnO is identified to be mainly due to decay of excitonic molecules into longitudinal B excitons and upper B polaritons. This process is easily stimulated and gives rise to a M_2-band of positive gain. In the same work, the positive OG coefficient spectrum of M-band was measured applying VSL technique. The positive OG was measured at the excitation density as low as 30 kW/cm^2 and the OG value around $g_M = 100$ cm^{-1}. The number of levels and their separation, which is almost equal to the A-B valence band splitting of ~ 6 meV, suggest that the three biexciton levels correspond to the three possible combinations of A and B valence band [65].

In the ZnO nanorods the M-band appearance was reported at 3.350 eV photon energy at 70 K temperature. The decay time of M-band was measured in the temperature range from 8 K to around 180 K ($k_BT = 15.5$ meV). It was shown, that the decay time is temperature independent with $\tau_M \approx 80$ ps [66].

2.5 Doping

For ZnO applications the p and n doping is necessary. The nominally undoped ZnO epitaxial layers are n-type. Despite the fact, that there is variety of dopants available for p-type doping, the highly conductive stable and reproducible p-type ZnO epitaxial layers are still major issue. Compared to other II-VI semiconductors and GaN, it has been difficult to dope ZnO to produce a p-type semiconductor because of a strong self-compensation effect arising from the presence of native defects or hydrogen impurities. This problem is very common for wide band gap materials. The semiconductors ZnO, ZnSe, CdS or GaN are generally n-type while ZnTe is generally p-type [4]. Oxygen vacancies (V_O), V_O complexes, Zn interstitial-related complexes, and residual impurities such as H and Al are all believed to be donors in ZnO, while Zn vacancies (V_{Zn}) and their complexes are considered to be acceptors [67].

For the long time, one of the most suitable dopants is considered to be

N on the O site (N_O) due to the similar atomic radius. D. C. Look *et al.* demonstrated the successful *p*-type doping in ZnO with N and estimated N caused acceptor energy level less than 200 meV from the valence band [68]. Also, PL lines at the energy 3.238 eV and 3.315 eV were attributed to the donor-acceptor transition and neutral acceptor bound exciton radiative transition A^0X, respectively.

Later, the theoretical calculations revealed, that N is actually a deep acceptor with a ionization energy around 1.3 eV [69]. However, recently the compelling study showed, that shallow acceptor levels are created not by N in O site N_O, but by complexes of V_{Zn}-N_O-H^+ involving the Zn vacancy V_{Zn} and ionized hydrogen H^+. The estimated acceptor ionization energy for such complex is 134 meV [70].

For *n*-type doping of ZnO, the Ga is reliable dopant. In the highly doped *n*-type conductivity ZnO the electron concentration can reach up to 10^{21} cm^{-3}, while in the *p*-type ZnO the hole concentration is not higher than 10^{18} cm^{-3} [16].

Some breakthrough was done by realization of co-doping of ZnO epitaxial layers [17]. Li atoms substitute Zn and act as acceptors, while the incorporation of N makes interstitial Li passive and reduces the possible compensation of Li_{Zn} acceptors.

2.6 Devices

2.6.1 Light emitting devices

Recently, the breakthrough in ZnO heterostructure based LEDs has been made. The novel *p*-$Mg_{0.25}Zn_{0.75}O$:(Li,N)/*n*-ZnO single heterostructure was fabricated on sapphire (0001) substrate using MBE growth technique. The lifetime of the LED first time reported to be about 6.8 hours feeding with continues current of 20 mA and it is the evidence of reliable *p*-type doping of ZnO based epilayers [17]. The output power of the LED reported to be in the order of tens of nanowatt. The reproducible *p*-type doping was implemented by employing Li and N as a dual-acceptor dopant in MgZnO.

The peak emission of the EL is reported at around 392 nm with the weak DRC emission at around 500 nm. The NBE peak wavelength differ from earlier reported EL peak position, which is usually located at around

420 nm. According to the paper, this discrepancy occurs due to the particular structure of the LED and the EL rises from the NBE exciton radiative recombination in n-ZnO layer, rather than from the DAP radiative recombination in p-ZnO layer as reported by others [30].

Other interesting phenomena is the EL enhancement with LSP. The EL of LEDs by LSPs can be enhanced in two ways. One is the increase of the internal quantum efficiency of the device when the carriers in the active region are coupled with the LSP modes. Therefore the capture probability of the carriers by non-radiative centers is reduced significantly. The other way is to enhance the external quantum efficiency of the device to reduce the loss caused by total reflection. The former mechanism works if the metal NPs are introduced near the active region of the device and the latter mechanism works if the NPs are deposited on the surface of the device. The generated LSP modes can be extracted as photons. Because the LSP coupling rate is much faster than the recombination rate of the electron-hole pairs, the electron-hole pairs have a less probability to be captured by nonradiative centers.

Recently it was reported that the EL of ZnO LED may be enhanced 5 times by introducing the Ag NPs in the LED structure [71]. The n-ZnO/NPs/i-ZnO/MgO/p-GaN LED structures on the sapphire (0001) substrate were fabricated with the different size metal NPs sandwiched between n-ZnO and i-ZnO (as active layer). The size of NPs has crucial role for the LSPs enhancement effect as the LSP resonance extinction spectrum has to be consistent with the emission spectrum of the LED.

2.6.2 Detectors

The single-crystalline cubic MgZnO epilayers were reported as an excellent solar-blind photodetectors with the attractive characteristics by Wang *et al.* [72]. The single-phase cubic 700 nm thick MgZnO epitaxial layers with 54% of Mg in the alloy were grown on the sapphire substrates. The authors claim, that high crystalline quality was achieved without highly possible inclusions of wurtzite-phase MgZnO due to transition from wurtzite ZnO to cubic MgO crystal structure [73]. The single phase cubic MgZnO epitaxial layer was achieved by applying the relatively low growth temperature and oxygen rich growth ambient in the MOCVD chamber. The

fabricated photodetector shows significantly smaller dark current of about 1.5×10^{-11} A/cm^2, what is comparable with best AlGaN solar-blind photodetector with 1.6×10^{-11} A/cm^2 dark current value. The responsivity of the device is reported about 396 mA/W at 10 V bias, what is more than three orders of magnitude larger than the responsivity of earlier reported MgZnO based solar-blind photodetectors [72].

2.7 Radiative and nonradiative recombination

The non-equilibrium carriers in the semiconductor can recombine either radiatively or nonradiatively, as it is depicted in Fig. 2.10. After excitation these two processes occur simultaneously with corresponding rates R_r and R_{nr}, respectively. As a result, the excited non-equilibrium carriers returns to the initial state by giving away the energy of excited state as photons or phonons. The total carriers recombination rate is expressed as $R = R_r + R_{nr}$.

The radiative recombination rate can be calculated using rate equations. The radiative recombination rate R_r follows the bimolecular rate equation:

$$R = Bnp, \tag{2.5}$$

where n is electron concentration and p is hole concentration. The proportionality constant B is called the bimolecular recombination coefficient. For excitons the recombination rate equation is monomolecular:

$$R = B_{ex} n_{ex}, \tag{2.6}$$

as the excitons correlated electron-hole pairs and are bound together. By solving differential rate equation one can yield that with time photogenerated excess carriers Δn recombine exponentially

$$\Delta n(t) = \Delta n(0) \mathrm{e}^{-B(n_0+p_0)t} = \Delta n(0) \mathrm{e}^{-\frac{t}{\tau}}, \tag{2.7}$$

where $\Delta n(0)$ is excess carrier density at $t = 0$, n_0 and p_0 are equilibrium

carrier densities. The carrier lifetime τ can be expressed as

$$\tau = \frac{1}{B(n_0 + p_0)}, \tag{2.8}$$

which is limited for the low excitation condition. τ is measured by preforming experiment as PL decay time. It is inverse quantity to the total recombination rate R:

$$\tau_{PL} \equiv \tau = \frac{1}{R} = \frac{\tau_r \tau_{nr}}{\tau_r + \tau_{nr}}. \tag{2.9}$$

Internal quantum efficiency (IQE) is radiative recombination probability and is described as ratio of radiative ratio R_r with total recombination ratio

$$\mathrm{IQE} = \frac{R_r}{R} = \frac{\tau_{PL}}{\tau_r}. \tag{2.10}$$

Therefore, even if the PL decay time was measure, the radiative recombination time is unknown. On the other hand, we can write, that

$$\mathrm{IQE} = \frac{1}{1 + \frac{R_{nr}}{R_r}} = \frac{1}{1 + \frac{\tau_r}{\tau_{nr}}}. \tag{2.11}$$

If the $\tau_r \ll \tau_{nr}$, then IQE is close to 1. It is the same as $R_r \gg R_{nr}$ and this condition becomes valid at low cryogenic temperatures. Therefore, if the radiative recombination rate is dominant over nonradiative recombination rate and nonradiative recombination rate does not changes with temperature, IQE can be estimated from the PL intensity variation with temperature [74, 75, 76, 77]:

$$\mathrm{IQE} = \frac{I_{PL}(T)}{I_{PL}(T \to 0)}. \tag{2.12}$$

The nature of the nonradiative centres is point defects, impurity-related defects, threading dislocations and stacking faults [79]. The point defects are dislocations of native atoms from their position in the lattice grating, for example Zn vacancies (V_{Zn}) or oxygen vacancies (V_O). The impurity-related defects are created by presents of different nature atoms in the lattice causing local deviations from crystal periodicity. In ZnO, common impurities are N, Cu, Pb, Fe, S and other coming in the process of Zn excavation and purification. Threading dislocations are typical defects of heteroepitaxial

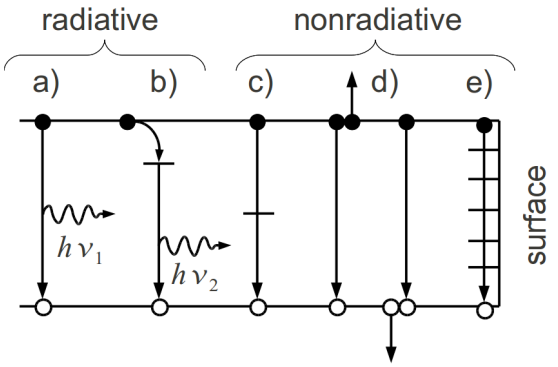

Figure 2.10: Schematic drawing of the possible radiative and nonradiative processes in the semiconductors: a) the band-to-band radiative recombination; b) radiative recombination through the defect levels; c) the nonradiative recombination through the deep defect levels; d) the nonraditive Auger recombination; e) nonradiative surface recombination. [78]

growth arising at the epitaxial layer and substrate interface due to lattice mismatch. Stacking faults are the inclusions of different politypes of the same crystal only with different lattice structure.

2.8 PL intensity dependence on excitation power

The PL intensity is proportional to excitation power density as $I_{PL} \propto P_{exc}^{\beta}$, where exponent β can be of various values depending on the recombination mechanism. This can be determined by solving the rate equations of carriers recombination. The case of radiative free carriers and excitons recombination is well described in ref. [74], for example. In thermodynamic equilibrium of the recombination and the generation, the recombination rate R is proportional to the excitation power density P_{exc}. For a bimolecular recombination of free electrons and holes, the equation yields

$$P_{exc} \propto G = R = An + Bn^2, \tag{2.13}$$

where G is generation rate, n is the excess charge carrier density. (An) describes the nonradiative rate, and (Bn^2) the bimolecular radiative rate. Note, that Auger recombination, which is proportional to n^3, is neglected.

The PL intensity I_{PL} is proportional to the radiative rate:

$$I_{PL} \propto Bn^2. \tag{2.14}$$

Therefore the excitation power density

$$P_{exc} \propto A' I_{PL}^{0.5} + B' I_{PL}. \tag{2.15}$$

For excitons the equations yield

$$P_{exc} \propto G = R = An_{ex} + B_{ex} n_{ex}, \tag{2.16}$$

$$I_{PL} \propto B_{ex} n_{ex}, \tag{2.17}$$

$$P_{exc} \propto A' I_{PL} + B'_{ex} I_{PL}. \tag{2.18}$$

When the recombination is dominated by radiative processes, $\beta = 1$ is expected for both a monomolecular exciton recombination process and a bimolecular recombination of uncorrelated electron-hole pairs. Due to large exciton binding energy E_x^b of ZnO and its compounds at excitation density lower than Mott density of photogenerated carriers the radiative recombination can always be assumed to have excitonic nature.

At low temperature the recombination is dominated by radiative process. When the temperature is increased, the monomolecular nonradiative recombination has to be considered. In the limit of a dominant nonradiative recombination, the rate equations yield $\beta = 2$ in the case of uncorrelated electron-hole pairs. For excitonic recombination $\beta = 1$ whether radiative or nonradiative recombination dominates [80]. The dependence index β equals to 1 in case of DRC transitions under low and medium excitation conditions, while it decreases to 0.5 for high excitations [24].

The integrated intensity grows linearly with excitation power as is expected for any emission with a quantum efficiency near unity [64]. A decrease of β parameter for higher excitation conditions can be due to the saturation effect and/or the local thermal heating of the sample [80].

3 Experimental techniques

Number of spectroscopy and structural analysis techniques were applied in this work. Although few of these may look similar or closely related, it may give different approach to the subject in question. Therefore, the data acquired by several spectroscopic techniques would sum up providing the deeper insight to the processes which take place in the semiconductor structures under investigation. The four main groups of the techniques are (i) the spectrally resolved time-integrated PL and absorption spectroscopy, (ii) the time-resolved spectrally resolved PL spectroscopy, (iii) advanced spectroscopy techniques, i.e. SNOM and LITG, and (iv) crystal structure and composition determination methods. In this chapter, all applied experimental techniques are described paying attention to the advantages and limitations.

3.1 Photoluminescence and absorption spectroscopy

A spectroscopy experimental setup would always consist of three main elements: (i) excitation source, (ii) light dispersing device, and (iii) light registration device.

There are two major types of excitation sources: with broad continuous spectrum for absorption, refraction, and photo-excitation spectroscopy and with monochromatic discrete spectrum for PL spectroscopy. As former light sources the deuterium, tungsten halogen or mercury vapour lamps are used. As monochromatic excitation sources lasers are used exceptionally. There is a vast variety of lasers available depending on the spectral region of interest and excitation power required. However, in the sense of PL registration approach lasers can be distinguished between CW and pulsed.

As light dispersing devices the monochromators with the holographic

gratings are used. For the best performance in most monochromators two holographic gratings are aligned with 1200, 600 or 300 grooves/mm in pairs for sufficient spatial resolution required in experiments. The characteristic quantity for monochromator is a focal length. It is the distance from an entrance slits to the exit slits of monochromator measured in meters. With the grater focal length the better spatial resolution can be achieved, although the loses of the PL signal increase. On the other hand, the small focal length monochromator ensure strong PL signal with lower spatial resolution.

As the light detectors the photodiodes, PMTs and CCDs are used. The photodiode is an semiconductor *p*-*n* junction plate with an applied voltage. The absorbed photons generate electron-hole pars and photocurrent is induced, which is proportional to light intensity exposed on the photodiode. The PMT is an vacuum tube with a photosensitive emulsion cathode. Due to the photoeffect the electrons are generated on the cathode and applied high voltage accelerates electrons along the tube and initial number of electrons is multiplied thousand of times in the cascade of photosensitive emulsion barriers to produce the measurable electrical signal. Therefore PMTs are highly sensitive light detection devices, although the avalanche photodiodes reach the sensitivity of a regular PMT. The CCDs however have advantage over the photodiodes and PMTs. It can measure the whole spectrum at once taking significantly less time for the experiment. The CCD is an array of photosensitive MOS diodes connected into single circuit. After the spatially resolved light exposure on the array, each element saves the amount of photogenerated charge, which is proportional to light intensity. The charge is read out from the elements one after another gathering the light intensity distribution over the photon energy. The CCDs are fast, however has limited spectral resolution. Often the light detectors are cool down below the RT to effectively reduce the signal-to-noise ratio.

3.1.1 Stationary PL measurement technique

The time-integrated spectrally resolved PL experiments were carried out applying photon-counting technique. This technique is most straight-forward method to measure PL. The CW excitation creates the stationary condition in the semiconductor sample: the carrier generation and recombination rates are equal and constant with time. Thus carrier concentration has no

time dependence. The PL signal is measured over the exposure time. The PL registration system integrates the signal over the whole exposure time, therefore weak PL signal can be measured by setting large exposure time. Because PL intensity depends on the exposure time the resulting PL intensity has to be given per time unit, i.e. per second.

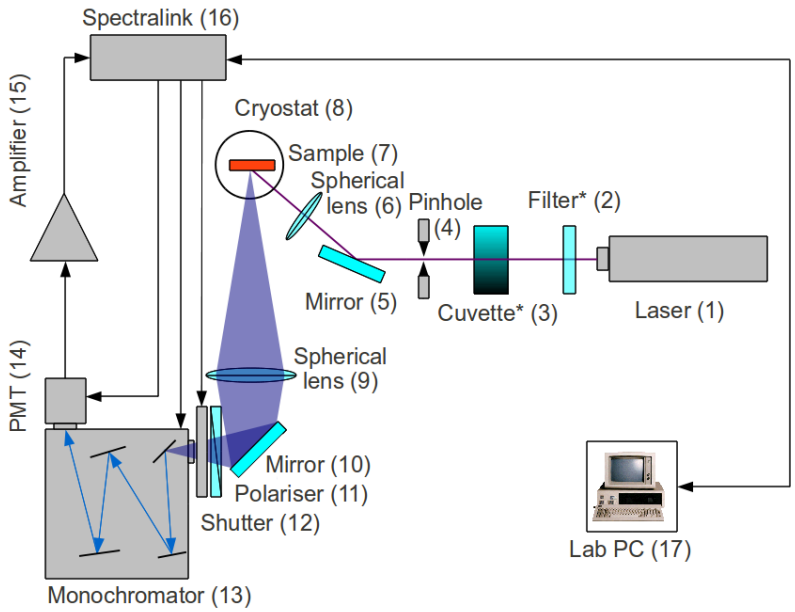

Figure 3.1: Schematic experimental setup for the photon-counting technique: 1- laser; 2- filter (with He-Cd laser); 3- cuvette with ink (in excitation dependent experiments); 4- diaphragm; 5- metal surface mirror; 6- spherical lens; 7- sample; 8- closed circuit He cryostat; 9- spherical lens; 10- collective mirror; 11- light polariser; 12- electromechanical shutter; 13- monochromator; 14- PMT; 15- amplifier; 16- equipment-computer interface "Spectralink"; 17- lab's personal computer with PL spectra recording and experiment controlling software.

The schematic experimental setup with CW laser (1) as an PL excitation source is shown in Fig. 3.1. The He-Cd laser (*Plasma*, HCCL-4UM) was used with excitation wavelength $\lambda_{exc} = 325$ nm and maximum output power $P_{out} = 6$ mW. The laser beam was filtered out from additional lines situated in the spectral range of interest using UFS-2 filter (2). Instead of He-Cd laser, for selective excitation of MQWs structures the CW violet

semiconductor LD (*Alphalas*, Monopower-405-150-MM) was used with the measured excitation wavelength $\lambda_{exc} = 403$ nm and the average excitation power $P_{exc} = 12$ mW after the losses in optical setup.

The laser beam was focused on the sample surface using spherical lens with focal length $f = 15$ cm (6). The variable excitation spot diameter results variation of excitation power density P_{exc}. The smallest diameter of the excitation spot was about 200 µm and that gives maximum excitation power density about $P_{exc} = 19$ W/cm^2 for He-Cd laser and about $P_{exc} = 38$ W/cm^2 for semiconductor diode laser. However, in excitation dependent measurements the fused quartz cuvette with water ink mixture of variable ratio (3) was used to attenuate excitation power. The laser power was measured using power meter (*Ophyr*, Nova Display) equipped with the silicon photodiode (*Ophyr*, PD300-UV).

For temperature dependent PL experiment samples (7) were placed in an optical cryostat (8). The closed-circuit liquid He cryostat (*CTI-Cryogenics*, model 22) allows temperature stabilization in the range from 8 K to 300 K using temperature control unit with a proportional-integral-derivative controller (*Lake Shore Cryotronics*, 331).

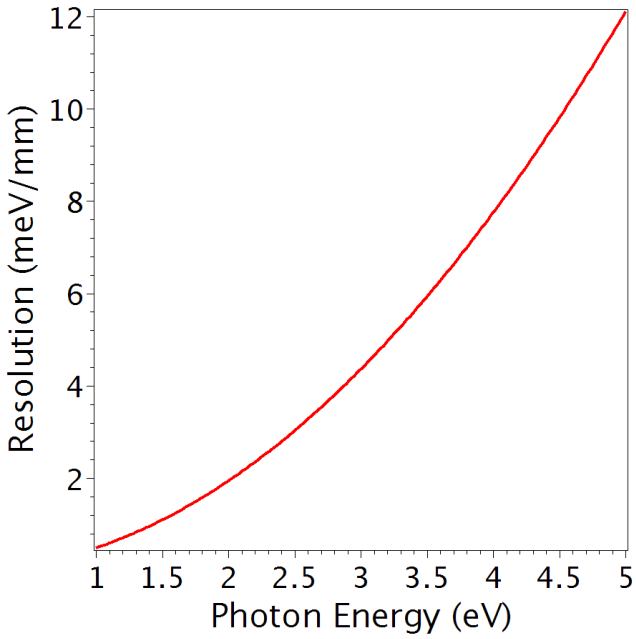

Figure 3.2: System resolution R_E for the PL measurements as a function of photon energy $h\nu$.

The PL signal from the sample was collected using the wide-diameter lens with focal length $f = 20$ cm (9) and front mirror of adjustable angle (10) to the monochromator (13). The vertically adjusted polariser (11) was used in most of the experiments resulting uniform signal response. The double monochromator (*Jobin-Yvon*, HRD1) with focal length of 0.6 m was equipped with two 1200 grooves/mm holographic gratings. The system spectral resolution R_λ determined by monochromator was 0.6 Å/mm. To evaluate the resolution R_E in meV/mm the relation was used:

$$R_E = \frac{4 \cdot (h\nu)^2 R_\lambda}{4 \cdot 1239.5 - h\nu R_\lambda}, \tag{3.1}$$

where $h\nu$ is the photon energy. The $R_E(h\nu)$ function graph is shown in Fig. 3.2. In the spectral region of interest, the system resolution was less than 5 meV for most of the experiments when the entrance and exit slits of the monochromator was set to the maximum 2 mm width. However, the better resolution less than 1 meV was achieved for experiments with specific purposes.

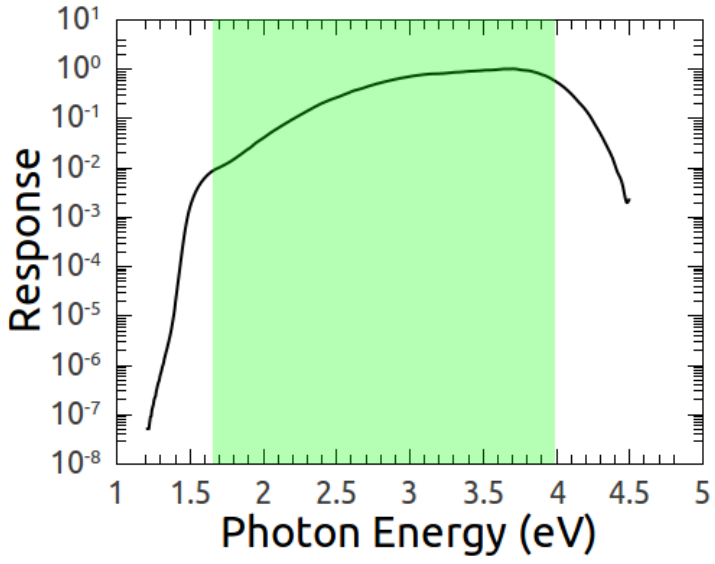

Figure 3.3: PL detection system response curve for the vertically polarised light. The system has a sensitivity peak at 3.71 eV (333 nm). The filled area denotes the range of interest for ZnO, CdZnO and MgZnO PL properties.

The PL signal was detected using PMT (14). The UV range sensitive PMT (*Hamamatsu*, R1463P) was cooled down to 5°C temperature using Peltier elements to reduce the signal-to-noise ratio. The electrical signal was amplified (15) and through the equipment-computer interface (16) transmitted to the lab's personal computer (17) for analysis and storage. The measured PL spectra were corrected according to the PL detection system response. The system response curve was measured using the continuous spectrum calibration light source (*Bentham*) equipped with halogen lamp CL2 for spectral range from 300 nm to 800 nm and deuterium arc lamp CL3 for spectral range from 200 nm to 400 nm. PL detection system response curve for the vertically polarized light is depicted in Fig. 3.3.

The precise calibration of the spectrometer was accomplished using the discrete spectrum calibration light source (*omt*, Iscal) equipped with the mercury and argon lamps emitting the lines from 254 nm to 922 nm. The lines at 435.84, 407.78 and 404.66 nm were used for calibration in the area of NBE PL of ZnO with the tolerable deviation of 0.5 meV.

3.1.2 Quasi-stationary excitation technique

The CW lasers are limited excitation sources in the sense of generated excitation power. If the He-Cd laser can produce the maximum output power of $P_{exc} = 10$ mW, one can estimate the photogenerated exciton density n_{ex} [81]:

$$n_{ex} = \frac{P_{exc}\alpha\tau}{h\nu\pi r^2}, \tag{3.2}$$

where α is the absorption coefficient of medium (i.e. ZnO), τ is the exciton lifetime, $h\nu$ is the photon energy of the incoming light, and r is the excitation spot radius on the sample surface. In the best case, the photogenerated exciton density in the sample is not more than 2.5×10^{16} cm^{-3}. Such excitation level is considered as medium or low excitation power densities for undoped or doped samples, respectively. The low-level excitation is defined with the condition $\Delta n \ll (n_0 + p_0)$, where Δn is the photoexcited carrier concentration and the n_0 and p_0 are the equilibrium concentration of electrons and holes, respectively. The high-level excitation is considered if condition $\Delta n \gg (n_0 + p_0)$ is fulfilled [78]. For example, in the undoped ZnO epitaxial layers typical electron concentrations are from 10^{17} cm^{-3} in

the poorer quality crystals to 10^{15} cm^{-3} in the better quality crystals [16].

To reach high excitation conditions, the pulsed lasers are used. Pulsed laser generates significantly more energy than CW laser as the output energy is concentrated in short period of time. After absorption of the laser pulse the photogenerated excess carriers in the semiconductor sample start to recombine to the ground states. Once the excitation pulse exposure is over, the PL signal is decaying exponentially with time constant τ_{PL}. At that time the PL detection system starts to measure the signal from the sample. Therefore synchronization of the PL detection system with the laser pulse generation must be accomplished so that PL registration device would measure the PL signal after every incident laser pulse at the laser repetition rate f_{rep}. When excitation pulse duration $\tau_{exc} \geq \tau_{PL}$, the PL excitation regime is called quasi-stationary suggesting that similar to stationary excitation conditions are achieved with pulsed excitation source. The schematic experimental setup of PL measurement in quasi-stationary excitation regime used in this work is shown in Fig. 3.4.

The fourth ($\lambda_{exc} = 266$ nm) and the third ($\lambda_{exc} = 355$ nm) harmonics of the Q-switched Nd:YAG^{3+} laser (*Ekspla*, NL301) were used with pulse duration $\tau_{exc} = 4$ ns and repetition rate $f_{rep} = 10$ Hz. The initial 1064 nm radiation of the pulsed laser (1) was mixed with second harmonic 532 nm radiation in non-linear optical crystal (2) for third or fourth harmonic generation. The maximum pulse energy generated in third and fourth harmonic non-linear optical crystals (3) was 80 µJ and 30 µJ, respectively. To reduce the output power of the excitation beam, the 4% of initial power was reflected using Bragg mirror (4) and excess power was collected into the dumper (5). Moreover, the excitation radiation power was reduced using the reflected beam from the surface of quartz prism (6), that is 10% of incident power. To this stage the generated optical output power from the laser was reduced 250 times. The fine adjustment of excitation power was accomplished using two α-GLAN polarisers (7,9) and $\lambda/2$ plate (8) in between. Such attenuator allows to adjust the optical power of excitation beam in the range of 4 orders of magnitude. The excitation power was measured using power meter (*Ophyr*, Nova Display) equipped with the photodiode (*Ophyr*, PD10-SH).

The same PL detection system as described in section 3.1.1 was used. However in quasi-stationary excitation regime, the PL signal is integrated over sufficient number of excitation pulses in stroboscopic mode. This is ac-

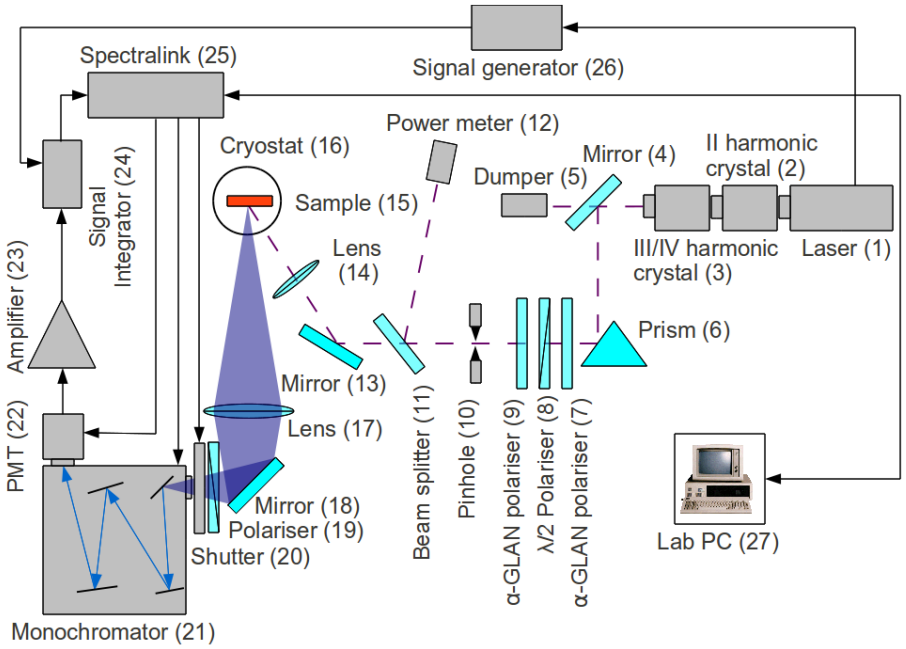

Figure 3.4: Schematic experimental setup for quasi-stationary excitation technique: 1- pulsed YAG:Nd^{3+} laser; 2- II harmonic crystal; 3- III or IV harmonic crystals; 4- diffraction mirror; 5- excess power dumper; 6- quartz prism; 7- front α-GLAN polariser; 8- $\lambda/2$ wave plate; 9- rear α-GLAN polariser; 10- diaphragm; 11- quartz beam splitter; 12- power meter; 13- dielectric mirror; 14- spherical lens; 15- sample; 16- closed circuit He cryostat; 17- spherical lens; 18- front mirror; 19- polariser; 20- shutter; 21- monochromator; 22- PMT; 23- amplifier; 24- boxcar signal integrator; 25- equipment-computer interface "Spectralink"; 26- signal generator; 27- lab's personal computer with PL spectra recording and experiment controlling software.

complished with boxcar integrator (24). It is synchronized with the pulsed laser through the laser triggered electrical signal delay unit (26). The delayed turn-on signal starts the boxcar integrator to acquire the amplified signal from the PMT (22) within the time window determined by the duration of the turn-on signal.

Even thought boxcar integration method allows to measure semiconductor structures under high excitation levels, the PL signal acquisition in stroboscopic mode increase the noise level in the detection system. One source is the laser pulse energy deviation, which was not more than 4% in the experiments. Although the averaging of the measured PL signal by the boxcar integrator reduces the deviation, the signal-to-noise level of boxcar technique is significantly higher if compare to photon-counting technique.

3.1.3 Variable stripe length technique

Different geometrical configurations can be used in the PL experiments. The most common is back-scattering configuration. In this geometry the excitation beam is focused by spherical lens to the sample surface and the PL signal is collected from the same side as it was excited with slightly different angle as shown in Fig. 3.5 a). Other possible geometry is to excite the sample from one side and collect the PL signal from the other side of the sample as shown in Fig. 3.5 b). This configuration has few advantages over back-scattering. For example, the spatially resolved PL signal distortion due to the interference of light in the multilayer samples may be significantly reduced because of the light scattering in dispersive medium. However in the case of epitaxial layer stacks, other side of the samples contains the thick substrates and epitaxial layers of different refractive index. Therefore the significant loss in PL signal intensity occurs even if the underlying stack and substrate are transparent.

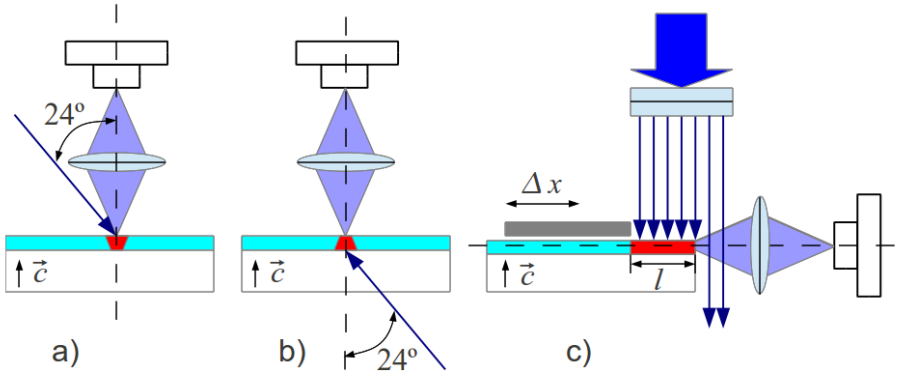

Figure 3.5: PL measurement configurations: a) back-scattering detection, b) forward detection, c) side emission detection.

In side-emitted PL configuration the PL is measured from the sample side parallel and excited perpendicular to the sample surface as it can be seen in Fig. 3.5 c). The use of cylindrical lens allows to create the thin excitation stripe on the sample surface. Edge PL configuration with the long, thin excitation stripe is one of few techniques to measure the OG coefficient in the semiconductors as active media for light amplification.

The OG can be measured using pump-probe technique [56, 82]. It is the most straight-forward method to measure the OG coefficient directly with time domain by observing the change in transmittance spectra after pump pulse with time delayed probe beam. The limitation of the method arises due to the necessity to use thin transparent films and can not be applied for the epitaxial layer stacks. The Hakki-Paoli method allows to measure the gain and current-induced phase shift in the low (below SE threshold) current density regime of the electrically driven structure [83, 84]. Therefore, to apply this method the completed structures for laser diodes with Fabry-Perrot cavity are used. However, in most cases the samples under investigation can not be processed to the required stage.

The VSL technique was employed for OG measurements. This technique demands few experimental conditions to be ensured strictly [85]. Otherwise the measured OG coefficient value or spectrum can be incorrect and lead to erroneous interpretation. If the demand for geometry of excitation stripe is not fulfilled, the SE can escape from the excited area to any direction and miss the PL detector. This is the case of the extremely large OG coefficient values, when the interval of l for unsaturated OG is only few tens of µm, as was shown for GaN epilayers by Mickevicius *et al.* in [86]. To create the narrow excitation stripe the excitation beam was focused onto the sample surface using cylindrical lens. The width of the excitation stripe (~ 20 µm) was estimated using a knife-edge technique. Lateral PL from the sample edge was measured using different excitation stripe length, which had been adjusted using a moving metal plate attached to the step motor with the step of 1.25 µm and travelling length of 2 mm. The OG spectra were obtained by analysing the measured edge PL spectra using formula:

$$g(h\nu) = \frac{1}{l} \ln\left(\frac{I_{2l}(h\nu)}{I_l(h\nu)} - 1\right), \tag{3.3}$$

where $g(h\nu)$ is the OG coefficient spectrum, l is the excitation stripe length, $I_l(h\nu)$ and $I_{2l}(h\nu)$ are the edge PL spectra measured at l and $2l$ excitation stripe lengths.

In case of high noise level, which arises due to non-linear nature of stimulated emission, the spectra were smoothed using the adjacent averaging algorithm. All measurements in side-emission configuration were carried out at RT.

3.1.4 Absorption spectroscopy

The absorption spectra were measured using the commercial UV, visible and NIR spectrometer (*Perkin Elmer*, LAMBDA 950). Two light sources are assembled in the spectrometer to cover the wide spectral range from 175 nm to 3300 nm. The light source for the UV and visible spectral range is deuterium lamp with continuous spectrum from 175 nm to 350 nm wavelength. For the visible and NIR spectral range the tungsten halogen lamp is used with continuous spectrum from 350 nm to 3300 nm wavelength. For measurements below 185 nm the N_2 purging must be applied to the spectrometer for removing the atmospheric O_2.

The spectrometer contains the double monochromator with holographic gratings of 1440 grooves/mm for UV and visible spectral range and 360 grooves/mm for NIR spectral range with reflection peaks at 240 nm and 1100 nm, respectively. The monochromator resolution for UV and visible spectral range is up to 0.05 nm and for NIR spectral range is up to 0.2 nm. All reflecting optic elements are quartz.

The beam splitting is achieved with rotating chopper at around 46 Hz frequency. The chopper produces the dark/sample/dark/reference cycle and transmits the radiation to sample or to reference compartments in sequence. The transmitted radiation through the reference compartment $I_0(\lambda)$ and through the sample compartment $I(\lambda)$ is directed to the same detector and alternately recorded. Then the transmittance $T(\lambda)$ is calculated as

$$T(\lambda) = \frac{I(\lambda)}{I_0(\lambda)} \tag{3.4}$$

and the optical density ρ_O is depicted as a function of wavelength

$$\rho_O(\lambda) = -\log_{10} T(\lambda). \tag{3.5}$$

Therefore, the absorption coefficient spectrum of the sample is calculated

$$\alpha(\lambda) = \frac{\rho_O(\lambda) \cdot \ln(10)}{d}, \tag{3.6}$$

where d is the sample thickness.

As a detector, the PMT R6872 is used for UV and visible spectral range from 175 nm to 800 nm. For NIR spectral range, the Peltier-cooled PbS photodiode is used from 800 nm to 3300 nm wavelength.

3.2 Time-resolved PL spectroscopy

3.2.1 Time correlated single photon counting

The time correlated single photon counting (TCSPC) technique is a method to record low level light signals with picosecond time resolution. The commercial available TCSPC spectrometer (*Picoquant*, Picoharp 300) was utilized. As an excitation source the semiconductor laser (*Picoquant*, PLD 800-B) at $\lambda_{exc} = 371$ nm wavelength with pulse duration $\tau_{exc} = 70$ ps and repetition rate $f_{rep} = 10$ kHz was used. The maximum output power of the laser was $P_{out} = 0.43$ mW. The PL is dispersed in the grating monochromator *Acton*. For the PL registration the CCD camera is equipped in the spectrometer.

The TCSPC technique is based on time-to-amplitude converter and statistical measurement of arrival time of PL photons. As the laser generates the light pulse for PL excitation, it simultaneously transmits the signal for time-to-amplitude converter. The signal starts the steadily increasing voltage in time-to-amplitude converter immediately while the sample after excitation emits the PL photons. The first PL photon that reaches the detector stops the increasing voltage amplitude. The measured voltage amplitude is transmitted through the analogue-to-digital signal converter to the analyser with digital memory. The analyser sorts the data by voltage values and adds the results of the same value. After the statistical processing of collected data for around 10 000 photons the results are presented as photon number dependence on time and allows to estimate the PL decay time τ_{PL}.

3.2.2 Time-resolved PL with Kerr shutter

In time-resolved PL experiment, the hybrid mode-locked YAG:Nd^{3+} laser (*Ekspla*) at $\lambda = 1064$ nm wavelength with pulse duration $\tau_{exc} = 27$ ps and repetition rate $f_{rep} = 10$ Hz was used as an excitation source. The laser generated radiation was amplified in the optical amplifier and directed to the non-linear optical crystals for generation of second harmonic at $\lambda_{exc} = 532$ nm and fourth harmonic at $\lambda_{exc} = 266$ nm wavelength. The fourth harmonic laser beam was aimed to the sample. The size of the excitation spot on the sample surface was about 1 mm. The maximum excitation

power density P_{exc} was reached up to 1 GW/cm^2.

The PL from the sample was collected in back-scattering geometry and dispersed by the 0.4 m focal length grating monochromator. The PL was registered using the cooled PMT. The PL detection system is sensitive in the spectral range from 1.6 to 4.0 eV photon energy and the maximum 1 meV step can be used for spectra measurement.

For time-integrated PL spectra, the GLAN polarisers were set in parallel position to each other. In this case, the maximum of PL signal was exposed to monochromator entrance slit. For the time resolved mode, the GLAN polarisers were set in perpendicular position that the PL signal was screened. The toluene optical Kerr shutter was placed between the polarisers. The exposure of stroboscopic first harmonic laser pulse on Kerr shutter caused the change of refractive index proportional to light intensity. As a result, the PL signal was elliptically polarised in the Kerr shutter therefore could pass the screening GLAN polariser and enter the PL detection system. The temporal resolution is limited by laser pulse duration.

For low temperature experiments the samples were placed in the liquid argon cryostat (*Cryo Con*). The measurements were carried out in the temperature range from 80 K to 323 K.

3.2.3 Streak camera

Streak camera is a high-speed detector which captures light emission occurring in extremely short time periods. The streak camera measures light intensity variation with pico- and nano-second temporal resolution and simultaneously measures the spatial distribution.

The light pulse to be measured is projected onto the slit of monochromator and is focused by the input optics on the photocathode of the streak tube. The photons are converted into a number of electrons proportional to the intensity of the incident light. The electrons are accelerated and conducted towards the sweep electrodes. As the group of electrons created from the light pulse passes between a pair of sweep electrodes, a high voltage is applied resulting in a high-speed sweep. The electrons are deflected at different times and at slightly different angles in the perpendicular direction. Then the electrons are conducted to the micro-channel plate, where they are multiplied several thousands of times. The amplified electrons are

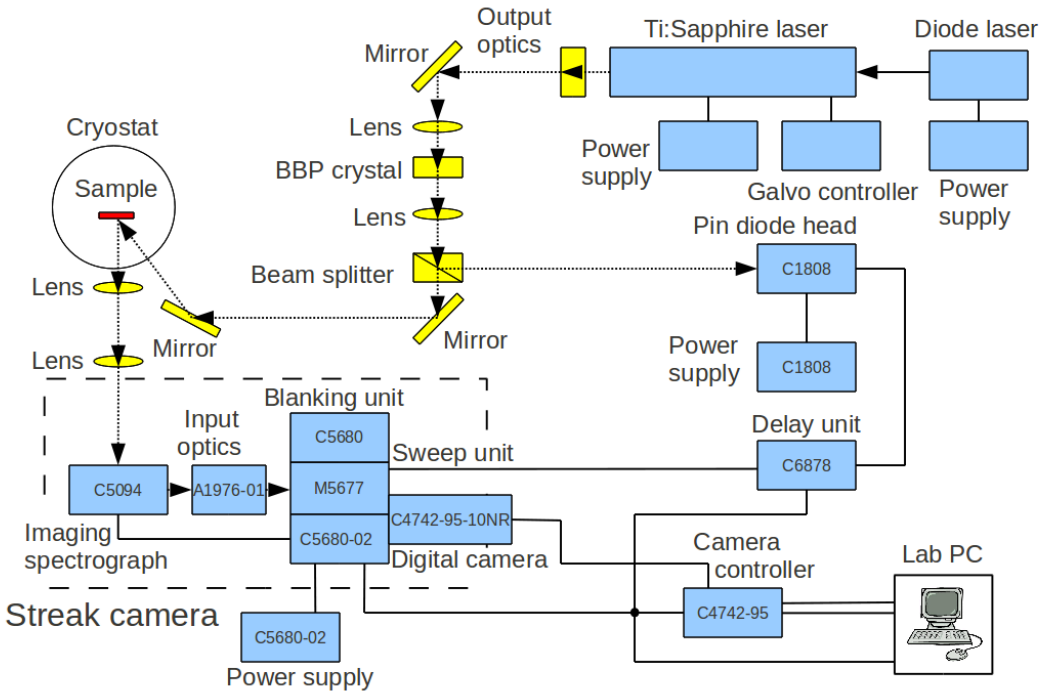

Figure 3.6: Time-resolved PL experimental setup with the streak camera (*Hamamatsu*, C5680-02).

bombarded against the phosphor screen, where they are converted back into light. The axis in the perpendicular direction of the fluorescence image is the temporal axis. The position in the horizontal direction on the phosphor screen correspond to the spatial axis. The brightness of the fluorescence image is proportional to the intensity of the incident light pulse.

The schematic drawing of the time-resolved PL setup with streak camera as a PL signal registration device is shown in Fig. 3.6. As an excitation source the frequency doubled of mode-locked Ti:sapphire laser (*Coherent*, Mira 900) was used with $\lambda_{exc} = 390$ nm wavelength for excitation of MQWs selectively, that means avoiding excitation of barriers. The pulse duration τ_{exc} was 3 ps with repetition rate $f_{rep} = 76$ MHz. The output power of the laser P_{out} after second harmonic generation was around 12 mW. The laser beam was focused on the sample surface to the spot of the focalization diameter about 200 µm. The excitation power density P_{exc} was around 38 W/cm^2 and the excitation energy density per pulse $I_{exc} = 8.5$ mJ/cm^2 achieved.

3.3 Advanced spectroscopy techniques

3.3.1 Light-induced transient gratings technique

The light-induced transient grating (LITG) is a powerful technique to study the non-equilibrium carrier dynamics in semiconductors. LITG allows to measure the carrier lifetime τ_R, diffusion coefficient D, and surface recombination velocity σ. The principle of this technique is to pump the sample with two coherent light beams to create the interference gratings on the sample surface. Two third harmonic laser beams at $\lambda_{exc} = 355$ nm wavelength of mode-locked YAG:Nd^{3+} laser was used for creation of the gratings. The pulse duration of the laser beams was 25 ps.

The absorbed light excites the carriers spatially distributed in lateral direction x as $N(x) = N_0 + \Delta N \cos(2\pi x/\Lambda)$, where the N_0 is the equilibrium carriers, ΔN is the photo-excited carriers and Λ is interference period. The modulation of carrier density results in modulation of refractive index change δn. The sample is probed with the other laser beam, which propagates through the sample without absorption. The time delayed first harmonic laser beam at $\lambda = 1064$ nm of the same laser was used for probing. The variable delayed probe beam monitors the dynamics of induced modulation of the refractive index by diffraction on the grating. The diffraction efficiency $\eta_d(t)$ is proportional to squared carrier density, and it is related with decay of ΔN as

$$\eta_d(t) \propto \exp\left(-\frac{2t}{\tau_G}\right), \tag{3.7}$$

where τ_G is the characteristic time of the experimentally observed grating decay.

The exponential decay of diffraction grating is caused by two effects. One is the recombination of the ΔN and the other is the diffusion of ΔN. The grating decay time τ_G can be expressed through the ambipolar diffusion D_a and recombination time τ_R as

$$\frac{1}{\tau_G} = \frac{1}{\tau_R} + \frac{4\pi^2 D_a}{\Lambda^2}. \tag{3.8}$$

Thus, a linear plot of $1/\tau_G$ versus $1/\Lambda^2$ allows one to find both τ_R and D_a simultaneously by measuring decay of the grating efficiency at different Λ.

3.3.2 Scanning near optical field microscopy

The scanning near optical field microscopy (SNOM) results gives detailed and direct information on local, growth correlated variations of the band gap potential in semiconductor nanostructures on a subwavelength length scale, and carrier exchange processes between system of different dimensionality [87].

High spatial resolution PL measurements were performed by the SNOM apparatus based on the tuning fork technique. The illumination-collection operating mode was used. An uncoated multimode fibre tips were used for SNOM probes with average diameter of about 100 nm. Therefore the spatial resolution of the measurements was evaluated to be around this value. A third harmonic of the femtosecond Ti:Sapphire laser with wavelength 280 nm was used for excitation. PL signal from the fibre was measured by the liquid nitrogen cooled CCD camera. For the near field PL extraction the PL signal measured with the slightly retraced tip was subtracted from the PL signal with tip in contact.

3.4 Crystal quality investigation techniques

3.4.1 Atomic force microscopy

The AFM measurements were accomplished using *WITec* Alpha 300 S system. The AFM uses a probe to obtain surface topography images. Commercially available AFM probes with 10 nm tip diameter was used in the experiment; thus, providing a lateral resolution around 10 nm. The probe is placed in contact with sample and is scanned line by line until whole area of interest is scanned. Typical dimensions of scanned area are from 1×1 µm^2 to 30×30 µm^2.

3.4.2 Energy dispersive X-ray spectroscopy

The energy dispersive X-ray (EDX) spectroscopy is an analytical nondestructive technique used for elemental analysis or chemical composition characterization. After the irradiation in the scanning electron microscope with electron beam the sample emits X-rays due to the transition of excited shell electrons to the ground states. The emitted X-rays can be collected

and registered using X-ray detector. The measured energy of the emitted X-rays allows to determine the chemical composition of the sample and the measured intensity gives the information of the amount of chemical elements.

The acceleration voltage of exciting electron beam results the penetration depth of the electrons into the sample. Therefore the acceleration voltage can be chosen with respect to the thickness of the epitaxial layers of interest.

In this work, the EDX experiment was carried out using *CamScan* Apollo 300 thermal field emission SEM with attached *Oxford Instruments* X-Max SD X-ray detector of 50 mm^2 active area to estimate the Mg content x in the $Mg_xZn_{1-x}O$ alloys. The images were recorded under 4 kV electron accelerating voltage, resulting the electron energy of 4 keV. Therefore, the penetration depth of electrons into the sample was about 100 nm not exceeding the thickness of $\sim$ 120 nm thick MgZnO epitaxial layers.

4 Optical properties of undoped, Ga- and N-doped ZnO layers

In this chapter, the optical properties of the set of undoped ZnO (National Taiwan University), highly Ga doped ZnO epitaxial layers (Virginia Commonwealth University) grown by MBE, and N-doped ZnO thin films grown by DC magnetron sputtering (Kaunas University of Technology) are presented. In the beginning of each section, the basic optical properties are discussed briefly. Although it is at the most well described issues [4, 5, 16], there is a necessity to build the background for further discussion. Next, the subject is switched to the analysis of unique problems of each group of samples.

In the first section, the optical properties of undoped ZnO epitaxial layers are presented. This includes the PL analysis under stationary, quasi-stationary and pulse (nano- and pico-second) excitations, as well as SE investigations and OG measurements. The second section is addressed to the original model of the free exciton interaction with bound exciton forming the P-band in ZnO. In the third section, the optical properties of highly Ga-doped ZnO layers for transparent n-type contacts are presented. Finally in the fourth section, the optical characterisation results of N-doped ZnO films are presented, as the p-type conductive layers are of highly importance in research on ZnO.

4.1 Optical properties of ZnO epitaxial layers grown by MBE technique

The schematic structure of the samples is depicted in Fig. 4.1. The samples A1 and A2 contain undoped ZnO epitaxial layers grown by MBE technique (National Taiwan University) on sapphire (0001) substrate directly (sample A1) and with 2 µm thick GaN buffer layer in between (sample A2). The thickness of ZnO epitaxial layers is 650 and 340 µm for samples A1 and A2, respectively. The XRD experiment revealed the FWHM of ZnO (0002) plane diffraction line 800 and 200 arc sec for samples A1 and A2, respectively. The narrower line means the better structural crystal quality of ZnO epitaxil layer. The surface roughness was extracted from AFM scanned surface topography and it is 6.8 nm and 6.2 nm for samples A1 and A2, respectively. The crystal structure analysis by XRD showed that crystal quality of ZnO epitaxial layer on GaN buffer is better due to smaller in-plane lattice mismatch of ZnO with GaN (about 2%) than ZnO with sapphire (18%) [10]. However, the AFM results show that due to the relatively thick epitaxial layers, the surface quality is the same.

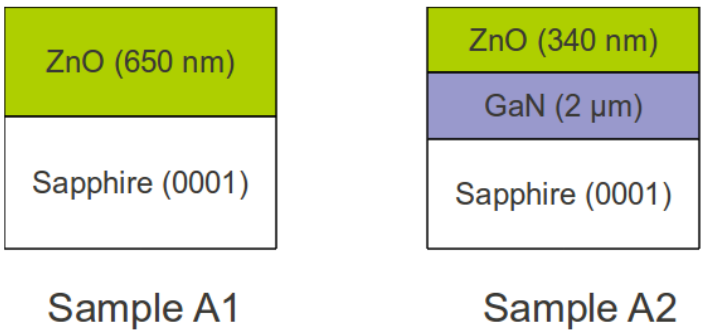

Figure 4.1: Schematic structure of samples with undoped ZnO epitaxial layers. Sample A1 is grown on the c-plane sapphire directly and sample A2 is grown on GaN buffer layer.

In Fig. 4.2 (a), low excitation PL spectra of ZnO epitaxial layers at RT are shown. For comparison, PL spectrum of bulk ZnO crystal grown by hydrothermal method (HT) is depicted. Typically spectra consist of two luminescence bands. More intense band is located in UV spectral region

at NBE of ZnO around 3.3 eV photon energy and is caused by free exciton annihilation. Also it may be the free-exciton annihilation with emission of one longitudinal optical phonon (1LO), as it is discussed in [88] and is quite probable process at RT. Second wide PL band dominates in the visible green spectral region and is originated from radiative recombination through the DRC caused by various crystal defects. In Fig. 4.2 (b) integrated NBE PL band intensity dependence on excitation power density is shown. Linear dependence in double logarithmic scale was fitted with the function $I_{PL} \propto P_{exc}^{\beta}$. The extracted dependence index is $\beta = 1.08$ for the NBE PL band showing the excitonic nature of the recombination. The integrated PL intensity of the DRC band increases sublinearly with the fitted exponent $\beta = 0.6$ supporting the recombination mechanism through the radiative DRC.

In the case of sample A1, the DRC band contains two spectral bands peaked at 2.16 eV and 2.49 eV photon energy and with FWHM of 610 meV and 150 meV, respectively. The DRC line of sample A2 is significantly suppressed and has the single peak at 2.16 eV photon energy with FWHM of 660 meV. Interestingly, the bulk ZnO crystal shows single DRC band peaked at 2.3 eV photon energy and with FWHM of 570 meV. As a result,

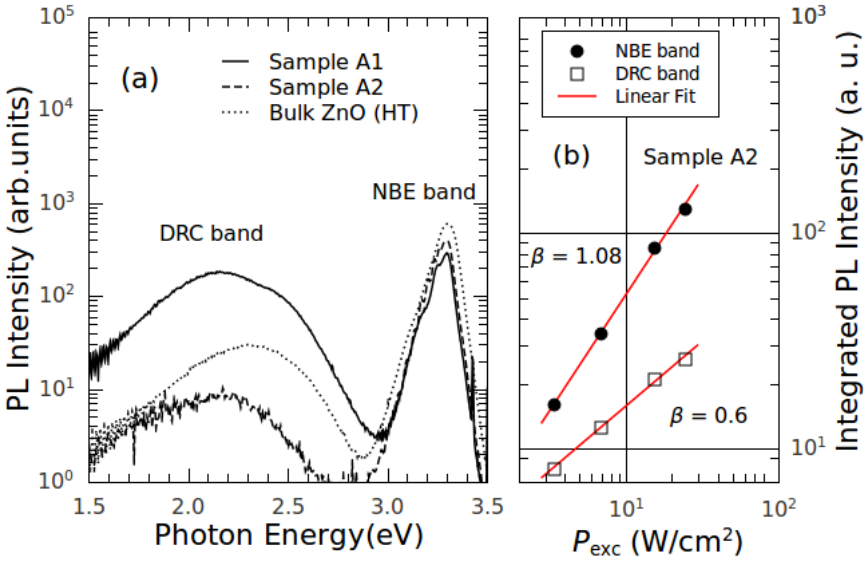

Figure 4.2: RT PL spectra of the samples A1 and A2 together with PL spectrum of bulk undoped ZnO crystal grown by hydrothermal method (a). Integrated PL intensity dependence on excitation power density for sample A2 (b) in low excitation conditions for NBE and DRC bands.

there is a difference in the DRC spectrum of bulk and epitaxial layers. The bulk ZnO crystal has dominant DRC line at higher energy, the epitaxial layer A1 has two well pronounced DRC bands, and the epitaxial layer A2, which has better crystal quality due to GaN buffer layer, has lower energy DRC band peaked at 2.16 eV photon energy. First-principles calculations shows that the most stable intrinsic defects are Zn and O vacancies and these defects can be related to the two DRC emission bands [67]. The lower and higher energy DRC PL bands at around 2.0 and 2.45 eV photon energy are related to V_{Zn} and V_O point defects.

Table 4.1: Low excitation spectra parameters of the ZnO heteroepitaxial layers and bulk ZnO crystal. I_{NBE} and I_{DRC} are the integrated intensities of near band edge and deep radiative centres bands.

Sample	A1			A2		bulk ZnO	
PL emission	NBE	DRC 1	DRC 2	NBE	DRC	NBE	DRC
Peak position (eV)	3.302	2.49	2.16	3.30	2.16	3.306	2.3
FWHM (meV)	102	150	610	105	570	112	570
I_{DRC}/I_{NBE}		3.34		0.12		0.23	

The ratios of the DRC to NBE luminescence integrated intensities are 3.34, 0.12, and 0.23 for samples A1, A2, and bulk ZnO, respectively. The significantly lower ratio for the sample with GaN buffer means the improved crystal quality of the ZnO epitaxial layer with reduced point defect concentration. The PL spectra parameters are summarized for comparison in Table 4.1.

The low excitation PL spectra measured at low temperature revealed more spectral features related to the crystal properties. The 8 K temperature PL spectra are depicted in Fig. 4.3. The most intense PL line is the prominent neutral donor bound exciton (D^0X) recombination at 3.360 eV and 3.358 eV. These lines are related to Al and Ga defects in ZnO and denoted as I_6 and I_8, respectively. To the same group of lines the I_{11} line at around 3.346 eV photon energy should be added, however the chemical identity of the spectral line is unknown [15].

To the higher energy side from the dominant D^0X line the free exciton recombination (FX) lines situate. The free exciton recombination to the

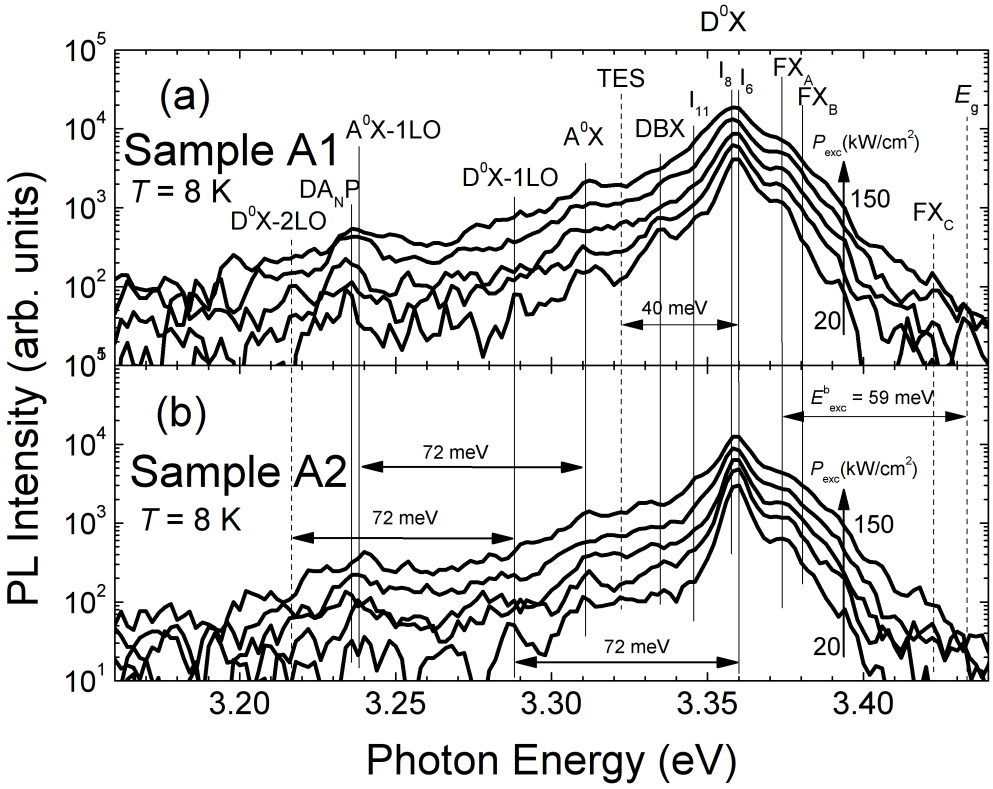

Figure 4.3: Low temperature PL spectra at low excitations (in the range from 20 to 150 kW/cm^2) for sample A1 (a) and A2 (b). The dependence on excitation power density is shown in order to clarify spectral lines as the spectral lines repeat in the spectra.

A valence band (FX_A) of the Γ_7 symmetry is situated at 3.374 eV photon energy. Duo to the spin-orbit splitting of the valence band the B exciton recombination can be expected around 8 meV apart the FX_A line. Indeed, the shoulder can be found 5 meV apart from the FX_A line to the higher energy side and it is attributed to the transition of free exciton to the B valence band of Γ_9 symmetry. The free exciton recombination to the C valence band of the Γ_7 symmetry is around 43 meV apart from the FX_B line and can be resolved at 3.422 eV photon energy. Even if this transition is forbidden for *c*-axis oriented epitaxial layers, due to the violation of crystal symmetry with defects and dislocations, the transition to the C valence band may occur.

To the lower energy side from the most intense D^0X line (the overlapped I_6 and I_8 and I_{11} lines) the DBX line is observed at 3.334 eV photon energy. The line is named after the study about its nature in ref. [15]. The line was

attributed to recombination of excitons bound at structural defects similar to recombination at 3.41 eV photon energy in GaN [89]. The spectral line at 3.322 eV is attributed to two electron satellite (TES) transition of the D^0X transition with the distance of 40 meV. The excitation of neutral donor from initial state to excited $1S$ state during the radiative recombination of the donor bound exciton (also possible $2S$ or $2P$ final states with the result of more adequate TES lines in PL spectra) is the mechanism behind this PL line. The spectral range for TES transitions to occur is considered from 3.34 to 3.31 eV. However, the PL line at 3.31 eV is neutral acceptor bound exciton (A^0X) recombination related with the presence of N in the ZnO [90] and this line may be dominant in N doped ZnO epitaxial layers. Other spectral line related to acceptor states in ZnO created by N is at the 3.236 eV photon energy. This line coincide with the spectral line of N doped ZnO epitaxial layers described in ref. [15]. There was shown the increase of the intensity of the line after annealing of the sample in the N_2 gas ambient. On the other hand, at the photon energy of 3.238 eV the first longitudinal phonon (1LO) replica of the A^0X line can be expected, as it is 72 meV apart from the main line. The two spectral lines are very close to each other and therefore hard to distinguish due to low intensity. Also the coexistence of the lines may be the case. The first and second longitudinal phonon (1LO and 2LO) replicas of the D^0X line are also marked in the Fig. 4.3 apart from the D^0X peak by 72 and 144 meV. These lines are very common in the low temperature PL spectra of good quality ZnO crystals (bulks and epitaxial layers) and get more intense with increase of temperature.

The PL peak position as a function of temperature was measured for ZnO epitaxial layers and is depicted in Fig. 4.4. The measurements were carried out under high excitation applying quasi-stationary excitation method. The experimental data are fitted using two approaches, namely, the empirical Varshni function [91]

$$E_0(T) = E_0(0) - \frac{\alpha T^2}{\beta + T}, \tag{4.1}$$

where $E_0(0)$ is PL peak energy at 0 K temperature, α and β are Varshni fitting parameters. Another function is the Bose-Einstein-like function

$$E_0(T) = E_0(0) - \frac{k}{e^{\theta/T} - 1}, \tag{4.2}$$

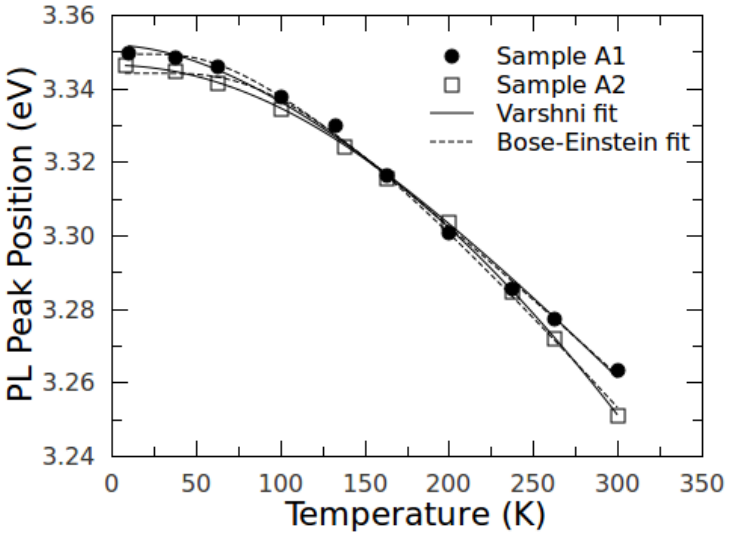

Figure 4.4: PL peak position dependence on temperature. The experimental points are fitted using Varshni and Bose-Einstein-like functions.

where k and θ are Bose-Einstein fitting parameters.

The fitting parameters are summarized in Table 4.2. The parameters are reasonable similar for both samples in case of both approximations. The only exception is Varshni function parameter β, which is proportional to Debye temperature. It is significantly higher for sample A2 than for sample A1.

Table 4.2: Fitting parameters for PL peak position dependence on temperature in samples A1 and A2 under high excitation level.

Samples	Varshni			Bose-Einstein like		
	$E_0(0)$ (eV)	α (meV/K)	β (K)	$E_0(0)$ (eV)	k (meV)	θ (K)
A1	3.35	0.6	281	3.35	0.1	226
A2	3.35	2.4	2008	3.35	0.18	326

The PL intensity decay time has been measured at different photon energies of the spectrum at RT. Typically rather long luminescence decay time of $\tau_{PL} = 6$ ns for ZnO NBE luminescence band evidences good quality of ZnO epitaxial layers. As it is shown in Fig. 4.5, the gradually increase of luminescence decay time up to $\tau_{PL} = 11$ ns with the decrease of photon

energy is measured for sample A1 and very similar decay time dependence on photon energy is measured for sample A2. This can be explained by involvement of the radiative recombination through the deep defect states, which is much slower process than band-to-band recombination.

The high crystal quality of the ZnO epitaxial layers is also confirmed by observation of SE at high injection levels of nonequilibrium carriers. Under CW excitation regime free exciton recombination line dominates the spectrum, whereas under quasi-state high excitation new line on the long-wave side of the spectrum appears. The new line can be explained by nonelastic exciton-exciton interaction as well as by SE in EHP if density of photogenerated carriers exceeds the the Mott density.

Indeed, as it is shown in Fig. 4.6 and 4.7 for samples A1 and A2, respectively, at excitation level of $P_{exc} = 350$ kW/cm^2 spontaneous excitonic luminescence of ZnO dominates the spectrum. It is shifted to 3.23 eV due to many body effect caused band gap shrinkage. When a particular excitation threshold is exceeded a new SE line appears at 3.17 eV due to exciton-exciton scattering [26, 92]. When excitation density exceeds the Mott density, SE of the EHP is observed at 3.15 eV photon energy. The EHP SE threshold is marked by the break point in the PL intensity dependence on excitation power density (Fig. 4.6(b) and Fig. 4.7(b)). One can observe the sudden change of dependence index value β from 1.4 to 4. The SE threshold was measured 1.9 MW/cm^2 and 2.75 MW/cm^2 for sam-

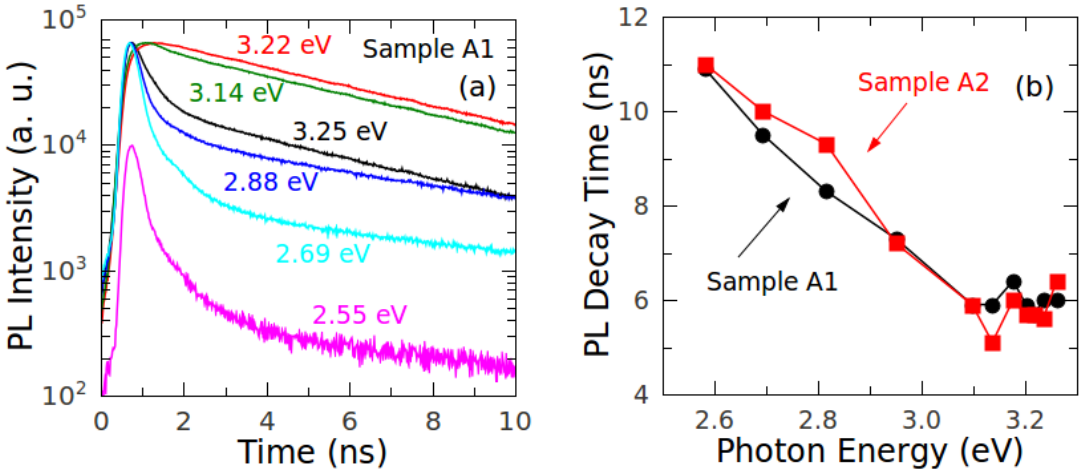

Figure 4.5: PL decay of sample A1 at fixated photon energies (a) and PL decay time dependence on photon energy for samples A1 and A2 (b) measured using TCSPC technique at RT.

ples A1 and A2, respectively. The SE threshold P_{th} is considered as optical characteristic for semiconductor structures as it is closely related with the crystal quality [23, 27]. As we can see, the SE threshold is lower for sample without GaN buffer layer, what contradicts to XRD results presented in the beginning of section 4.1.

Consequently, one can say that crystal quality of active layers itself is not the only characteristic affecting luminescence quantitative properties of ZnO epitaxial layers. However, the SE in epitaxial layers occur near the surface in the depth of few tens of µm. The AFM scan revealed very similar surface roughness for both samples. Therefore, due to the sufficient thickness of epitaxial layers, the substrate does not play important role for the optical characteristics of layers near the surface.

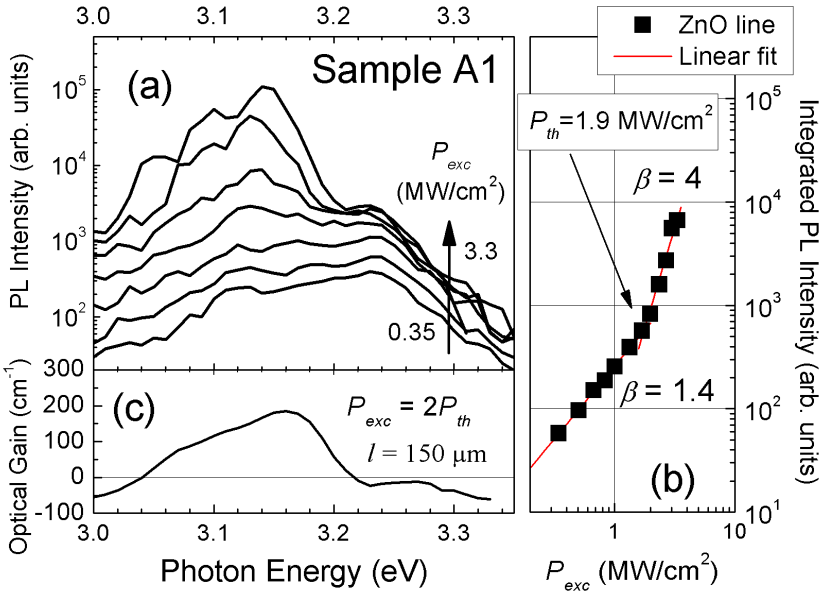

Figure 4.6: PL spectra dependence on excitation power density (a), integrated PL intensity as a function of excitation power density (b), and OG coefficient spectrum (c) for sample A1.

Furthermore, the OG coefficient spectra were also measured in VSL technique. The optimal OG coefficient spectra for samples A1 and A2 are shown in the Fig. 4.6(c) and 4.7(c). The OG spectrum has a peak value of 200 cm^{-1} at 3.16 eV photon energy in case of sample A1 and same peak

value of 200 cm^{-1} at about 3.18 eV photon energy in case of sample A2 in the similar experimental conditions. The measured OG coefficient values are consistent with the reported in the scientific literature. Y. Chen *et al.* reported the peak OG coefficient 177 cm^{-1} for the stimulated exciton-exciton scattering process and more than 500 cm^{-1} for EHP SE measured in the VSL technique [29]. The shape of the OG spectra for samples A1 and A2 significantly differ. The OG is positive from 3.04 to 3.22 eV and is asymmetric with long shoulder at lower energy side in case of sample A1. In case of the sample A2, the positive OG spectrum is narrower from 3.125 to 3.22 eV. At the same time it is more symmetric and has the peak shift to higher energy side within 30 meV. This can be explained by the different SE mechanism. As it is pointed out in [29], the symmetric and blue-shifted OG is a signature of stimulated inelastic exciton-exciton collision mechanism and the red-shifted OG spectrum with higher asymmetry are the characteristics for EHP caused OG. Note that, the excitation level for both samples are different due to difference in P_{th}.

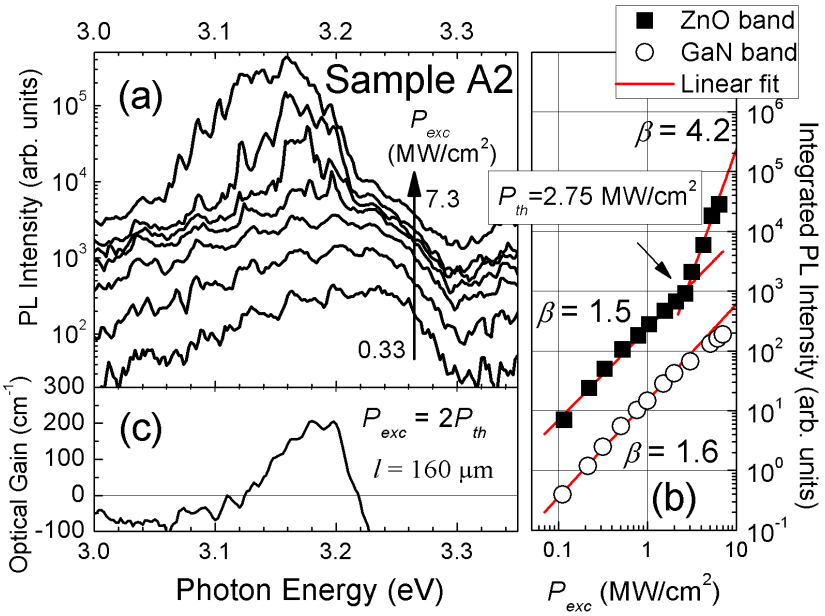

Figure 4.7: PL spectra dependence on excitation power density (a), integrated PL intensity as a function of excitation power density (b), and OG coefficient spectrum (c) for sample A2.

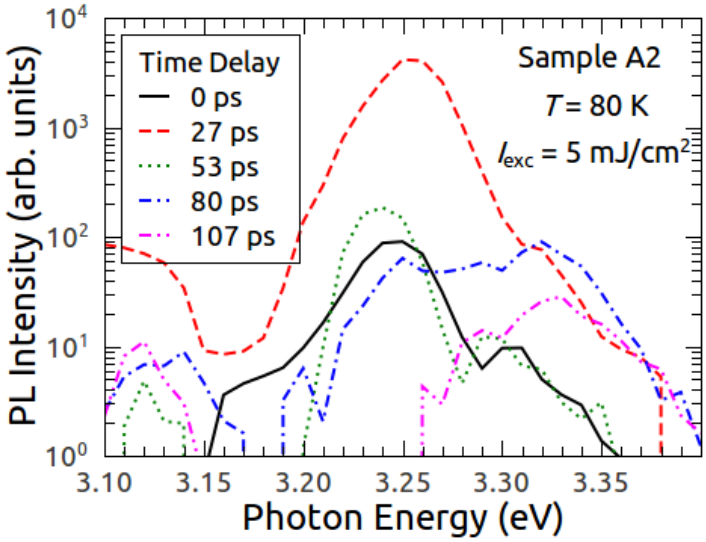

Figure 4.8: PL spectra of the sample A2 at different delay time. Spectra are measured at 80 K temperature with the excitation energy density of $I_{exc} = 5$ mJ/cm^2.

Fig. 4.8 shows time-resolved luminescence spectra of sample A1 in the spectral range of NBE emission. The measurement was carried out at 80 K temperature with excitation energy density of 5 mJ/cm^2 applying the time-resolved PL technique with the Kerr shutter. The time dynamics of the PL spectra clearly shows the co-existence of the exciton recombination band with the P-band, as these bands separate due to different recombination times. The P-band dominates the spectrum with the peak around 3.25 eV photon energy and decays completely within the first 80 ps of the delay time. The PL band of excitonic recombination at around 3.32 eV photon energy has slower decay time, therefore it remains at longer delay time. The energy difference between the peak position of two PL bands is close to 70 meV, what is more than exciton binding energy.

4.2 Model of inelastic interaction among free and localized excitons

The inelastic exciton-exciton collision caused P-band in the ZnO PL spectrum is usually overlapped with the PL bands of the other recombination mechanisms what makes difficult to unambiguously identify this spectral

line. The peak position reported in number of papers differs by value in the spectral range of around 3.1 ± 0.1 eV [93]. To identify the P-band in highly excited PL spectra of ZnO epitaxial layers the theoretical model of inelastic exciton-exciton collision was used [94]. The calculated P-band for ZnO is compared with the experimentally measured PL spectra. Theoretically, the P-band of inelastic exciton-exciton collision is expected in exact energy position: it is red-shifted at the distance of twice exciton binding energy from ZnO band gap energy E_g. However, there is an experimental fact of high diversity of the P-band's peak position energy in ZnO varying from sample to sample. The reported peak position values of P-band at different temperature are listed in the Table 4.3.

The experimental PL peak position energy values of P_2- and P-bands at different temperatures reported in number of papers are depicted in Fig. 4.9 according to the data presented in Table 4.3. Quite broad deviation from

Table 4.3: PL peak energy E_{PL} values of P-band at various temperatures T reported in the literature. The data is visualized in Fig. 4.9.

Emission band	E_{PL} (eV)	T (K)	P_{th} (kW/cm^2)	References
P-band	3.181	RT	400	Bagnall *et al.* [3]
EHP	3.14	RT	800	Bagnall *et al.* [3]
P-band	3.048	550	1200	Chen *et al.* [6]
P_2-band	3.20	RT	30	He *et al.* [60]
P-band	3.315	77	1900	Inagaki *et al.* [61]
P_2-band	3.332	77	1000	Inagaki *et al.* [61]
P-band	3.32	77	0.47	Ko *et al.* [63]
P-band	3.31	10	47	Pan *et al.* [62]
P-band	3.2	RT	260	Lu *et al.* [13]
P_2-band	3.22	RT	200	Lu *et al.* [13]
EHP	3.16	RT	580	Lu *et al.* [13]
P-band	3.18	RT	120	Ohashi *et al.* [95]
P-band	3.165	RT	64	Chen *et al.* [29]
P-band	3.20	RT	9000	Cho *et al.* [96]
P_2-band	3.067	RT	240	Bagnall *et al.* [28]
EHP	3.032	RT	1320	Bagnall *et al.* [28]
P-band	3.17	RT	–	Yu *et al.* [97]
P-band	3.315	10	0.27	Klingshirn *et al.* [35]
P-band	3.32	77	0.47	Yamamoto *et al.* [10]
P-band	3.26	RT	–	Cho *et al.* [98]

calculated theoretical peak position dependence on temperature using relation (2.3) is evident. The most aberrant values may be due to the misinterpretation of the band origin itself or possible calibration deviation of the PL detection systems in various experiment setups. Nevertheless, the unambiguous determination of the P-band in the PL spectra of ZnO is a difficult task.

As it was discussed in the section 4.1, the three bands coexists near the excitation levels of SE threshold. The spontaneous PL band of radiative exciton recombination is red-shifted due to the band gap renormalization effect and usually has a peak at 3.24 – 3.26 eV. The P-band may arise at the elevated excitation densities in case of good crystal quality ZnO. This band can also become stimulated prior to the appearance of the EHP SE. However, the spontaneous P-band and stimulated P-band have the same peak position, which does not depend on excitation power density. However, it deviates in different samples. The peak position of the P-band is usually in the interval from 3.14 – 3.2 eV. After the transition through the Mott density, the EHP SE line appears at around 3.13 eV and it has strong dependence on excitation power density to shift to lower energy side of the spectrum. Therefore, the identification of stimulated P-band is sometimes difficult task, as it is the case in section 4.1.

The same issue is discussed by J. Fallert *et al.* [93]. The overlapping of the P-band's energy position with the EHP SE line's energy position, especially just above the threshold excitation power density, is very possible. However, as it can be observed in Fig. 4.9 the deviation from the theoretical curve is mostly to the lower photon energy side and the energy difference becomes greater with the temperature increase.

We speculate, that the broad distribution of P-band's peak position can be the result of the free excitons interaction with defect bound excitons with lower energy by the value of ionization energy. To support our speculation based on experimental observations the model of inelastic exciton-exciton interaction is developed with the Dirac $\boldsymbol{\delta}$ wave function of one of two interacting excitons. The P-band spectra were calculated using ZnO material parameters and compared with the experimental PL spectra.

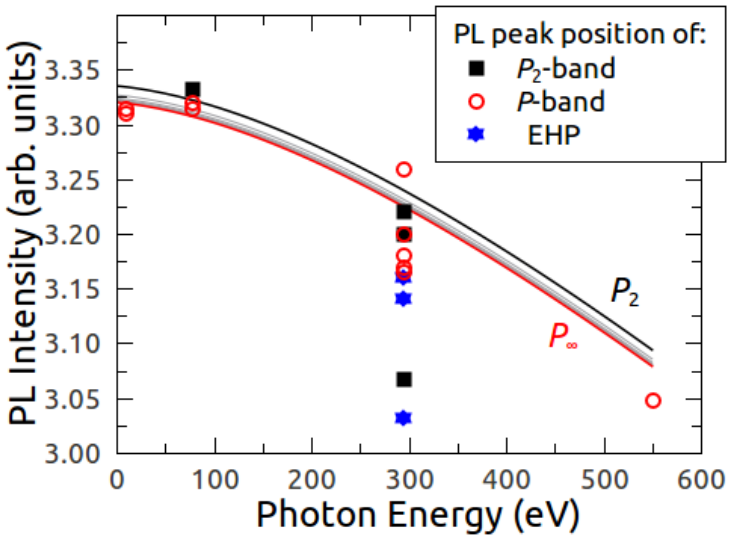

Figure 4.9: PL peak position energy of the P-band versus temperature. The lines represent the P-band's peak position energy dependence on temperature calculated using relation (2.3). The points show the experimental P-band's peak position energy reported in literature. The references are listed in the Table 4.3.

The collision of free excitons

According to the paper [94], there are four possible interaction mechanisms for excitons that may produce the luminescence. These processes can be expressed as follows:

(i) $(E_{\mathbf{K}}^{1S}, E_{\mathbf{K}'}^{1S}) \rightarrow (h\nu, e-h)$;

(ii) $(E_{\mathbf{K}}^{1S}, E_{\mathbf{K}'}^{2S,2P}) \rightarrow (h\nu, e-h)$;

(iii) $(E_{\mathbf{K}}^{1S}, E_{\mathbf{K}'}^{1S}) \rightarrow (h\nu, E_{\mathbf{K}''}^{1S})$;

(iv) $(E_{\mathbf{K}}^{1S}, E_{\mathbf{K}'}^{1S}) \rightarrow (h\nu, E_{\mathbf{K}''}^{2S,2P})$,

where $h\nu$ is the photon energy, $E_{\mathbf{K}}^{1S,2S,2P}$ is the energies of the $1S$, $2S$, $2P$ excitons with momentum $\hbar\mathbf{K}$, and $e-h$ is the energy of an electron-hole pair in the continuum state. The schematic diagram of the process (i) is depicted in Fig. 4.10 a). The process (i) is described as a radiative scattering via the exciton-exciton and exciton-photon interaction with the initial intermediate and final states, as shown in Fig. 4.10 b). The other three processes can also be described in exactly the same way.

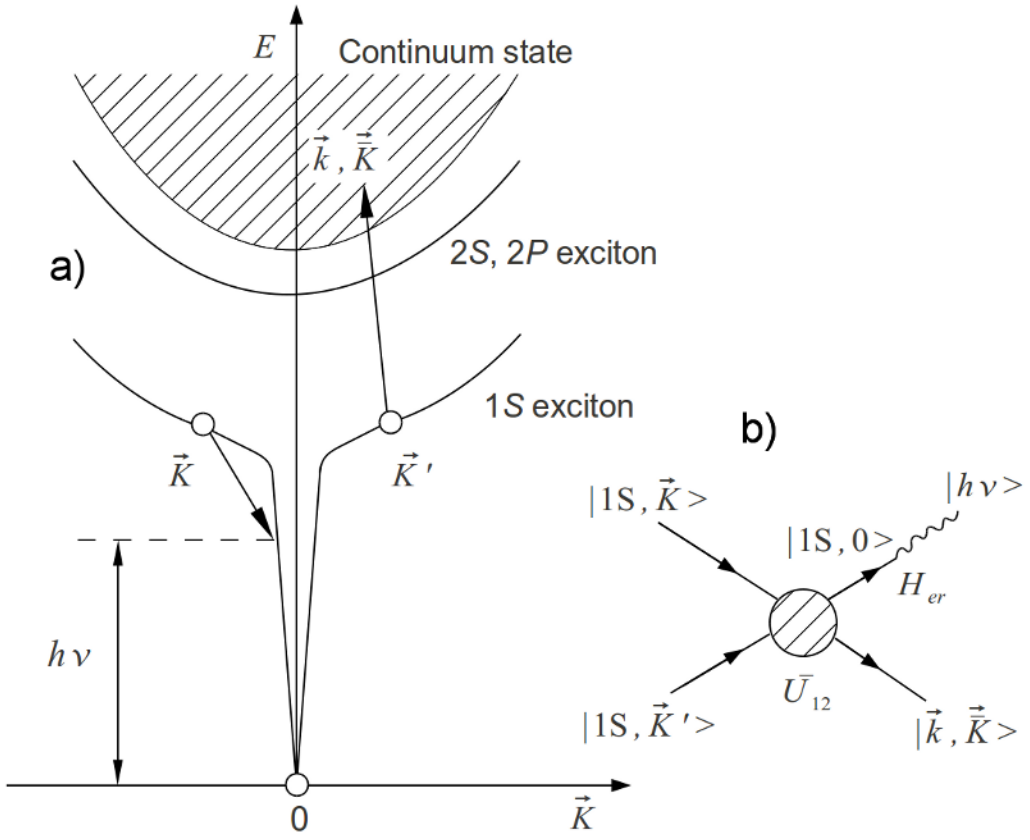

Figure 4.10: Schema of inelastic exciton-exciton interaction denoted symbolically as $(E^{1S}_{\mathbf{K}}, E^{1S}_{\mathbf{K}'} \rightarrow (h\nu, e-h)$ in the exciton states diagram (a). The diagram of the radiative exciton-exciton collision, where $\overline{U}_{12}$ is the interaction potential between the two excitons and H_{er} is the exciton-photon interaction Hamiltonian (b). [58, 94]

By the use of the second order perturbation theory the radiation power spontaneously emitted at $h\nu$ is given as

$$I(h\nu) = \frac{2\pi}{\hbar} \sum_{\mathbf{K},\mathbf{K}',\mathbf{k},\overline{\mathbf{K}}} \left| \frac{\langle 0|H_{er}|1S,0\rangle \langle \mathbf{k},\overline{\mathbf{K}}|\langle 1S,0|\overline{U}_{12}|1S,\mathbf{K}\rangle|1S,\mathbf{K}'\rangle}{E_0^{1S} - h\nu} \right|^2 h\nu\rho(h\nu)$$
$$\times n^{1S}_{\mathbf{K}} n^{1S}_{\mathbf{K}'} \delta\left(E_0^{1S} - E_x^b - h\nu + \frac{\hbar^2\mathbf{K}^2}{2M} + \frac{\hbar^2\mathbf{K}'^2}{2M} - \frac{\hbar^2\mathbf{k}^2}{2\mu} - \frac{\hbar^2\overline{\mathbf{K}}^2}{2M} \right). \tag{4.3}$$

where H_{er} is the exciton-photon interaction Hamiltonian, $|0\rangle$ is the ground state of the crystal, $\rho(h\nu)$ is the number of photon modes, $n^{1S}_{\mathbf{K}}$ and $n^{1S}_{\mathbf{K}'}$ are the mean occupation numbers of the $1S$ excitons with momentum $\mathbf{K}$ and

$\mathbf{K}'$, respectively, E_0^{1S} is the energy of $1S$ exciton at $\mathbf{K}=0$, E_x^b is the binding energy of the exciton, the reduced mass μ is given by $\mu^{-1}=m_e^{-1}+m_h^{-1}$, M is the translation motion mass of exciton $M=m_e+m_h$, and the $\overline{U}_{12}$ is the effective interaction potential between the two interacting excitons.

The argument of δ function reflects energy conservation, what is more clear when all cancelled terms are written

$$\left(E_0^{1S}+\frac{\hbar^2\mathbf{K}^2}{2M}\right)+\left(E_0^{1S}+\frac{\hbar^2\mathbf{K}'^2}{2M}\right)=h\nu+\left(E_0^{1S}+E_x^b+\frac{\hbar^2\mathbf{k}^2}{2M}+\frac{\hbar^2\overline{\mathbf{K}}^2}{2M}\right). \quad (4.4)$$

The optical matrix element is denoted as $\langle 0|H_{er}|1S,0\rangle = A$ and it does not have specific structure. Since we know that the occupation numbers are much smaller than unity, Boltzmann distribution is a good approximation for excitons:

$$n_{\mathbf{K}}^{1S}=N_{1S}\left(\frac{2\pi\hbar^2}{Mk_BT}\right)^{3/2}\exp\left(-\frac{\hbar^2\mathbf{K}^2}{2Mk_BT}\right). \quad (4.5)$$

To evaluate the radiation power $I(h\nu)$ we need to:

(i) calculate the matrix element of the Coulomb interaction,

(ii) perform the quadruple sum over the intermediate wave vectors.

The matrix element of the Coulomb interaction

The matrix element of Coulomb interaction was calculated by T. Moriya and T. Kushida [94] for two interacting free excitons in the form of

$$\mathcal{C}=\langle\mathbf{k},\overline{\mathbf{K}}|\langle 1S,0|\overline{U}_{12}|1S,\mathbf{K}\rangle|1S,\mathbf{K}'\rangle=\frac{32\pi^{3/2}a_0^{3/2}\hbar^2\overline{a}}{MV^{3/2}}\frac{1}{\left(1+a_0^2\mathbf{k}^2\right)^2}\delta_{\overline{\mathbf{K}},\mathbf{K}+\mathbf{K}'}, \quad (4.6)$$

where a_0 is the Bohr radius of the $1S$ exciton. The goal is to rebuild the intermediate steps omitted in the paper in order to understand the evaluation process.

The initial state is the product of the two $1S$ exciton wave functions with the wave vectors $\mathbf{K}$ and $\mathbf{K}'$. These exciton wave functions are the product

of the plain wave with centre of masses and hydrogen-like $1S$ function with relative coordinate

$$|1S,\mathbf{K}\rangle|1S,\mathbf{K}'\rangle = \frac{1}{\sqrt{V}}\mathrm{e}^{i\mathbf{K}\mathbf{R}_1}\varphi_{1S}(\mathbf{r}_1)\cdot\frac{1}{\sqrt{V}}\mathrm{e}^{i\mathbf{K}'\mathbf{R}_2}\varphi_{1S}(\mathbf{r}_2), \tag{4.7}$$

where V is crystal volume and φ_{1S} is the envelope function of the $1S$ exciton. From the analogy, the final state after collision is

$$|1S,0\rangle|\mathbf{k},\overline{\mathbf{K}}\rangle = \frac{1}{\sqrt{V}}\varphi_{1S}(\mathbf{r}_1)\cdot\frac{1}{\sqrt{V}}\mathrm{e}^{i\overline{\mathbf{K}}\mathbf{R}_2}\frac{1}{\sqrt{V}}\mathrm{e}^{i\mathbf{k}\mathbf{r}_2}. \tag{4.8}$$

As the result, we have to get the still exciton with zero momentum of the mass center, which later emits the photon, and electron-hole pair, which is described by its mass centre and relative momenta $\overline{\mathbf{K}}$ and $\mathbf{k}$. Hydrogen-like wave function is a normalized exponent function

$$\varphi_{1S}(\mathbf{r}) = \frac{a_0^{-3/2}}{\sqrt{\pi}}\mathrm{e}^{-\mathbf{r}/a_0}, \tag{4.9}$$

while the Coulomb interaction is approximated to δ function

$$\overline{U}_{12} = \frac{4\pi\hbar^2}{M}\overline{a}\delta(\mathbf{R}_1-\mathbf{R}_2), \tag{4.10}$$

where $\mathbf{R}_1$ and $\mathbf{R}_2$ are the center-of-mass coordinates of the two excitons with $\mathbf{R}_{12} = |\mathbf{R}_1-\mathbf{R}_2|$, and $\overline{a}$ is the scattering length of the excitons.

The product of wave functions and interaction potential have to be integrated over the coordinates of all particles:

$$\int \mathrm{d}^3\mathbf{R}_1\int \mathrm{d}^3\mathbf{R}_2\int \mathrm{d}^3\mathbf{r}_1\int \mathrm{d}^3\mathbf{r}_2. \tag{4.11}$$

However, the δ function eliminates the integral over $\mathbf{R}_2$ and we have simplified intermediate result

$$\mathcal{C} = \frac{4\pi\hbar^2\overline{a}}{MV^{5/2}}\int \mathrm{d}^3\mathbf{R}_1\,\mathrm{e}^{i(-\overline{\mathbf{K}}+\mathbf{K}+\mathbf{K}')\cdot\mathbf{R}_1}\int \mathrm{d}^3\mathbf{r}_1\,\varphi^*_{1S}(\mathbf{r}_1)\varphi_{1S}(\mathbf{r}_1)\int \mathrm{d}^3\mathbf{r}_2\,\mathrm{e}^{-i\mathbf{k}\mathbf{r}_2}\varphi_{1S}(\mathbf{r}_2). \tag{4.12}$$

First two integrals are trivial

$$\int \mathrm{d}^3\mathbf{R}_1\,\mathrm{e}^{i\left(-\overline{\mathbf{K}}+\mathbf{K}+\mathbf{K}'\right)\cdot\mathbf{R}_1} = V\delta_{\overline{\mathbf{K}},\mathbf{K}+\mathbf{K}'}, \tag{4.13}$$

$$\int \mathrm{d}^3\mathbf{r}_1\, \varphi_{1S}^*(\mathbf{r}_1)\varphi_{1S}(\mathbf{r}_1) = 1. \tag{4.14}$$

while the third integral can be simplified by applying the cylindrical symmetry, i.e. by using spherical coordinates

$$\int \mathrm{d}^3\mathbf{r}_2 \longrightarrow 2\pi \int_0^\infty \mathrm{d}\mathbf{r}\, \mathbf{r}^2 \int_0^\pi \mathrm{d}\theta\, \sin\theta. \tag{4.15}$$

We introduce dimensionless coordinate $\mathbf{r} \to a_0\mathbf{r}$ and assign $\nu = \cos\theta$. Then we have

$$\mathcal{C} = \delta_{\overline{\mathbf{K}},\mathbf{K}+\mathbf{K}'} \frac{8\pi^{3/2}\hbar^2\overline{a}a_0^{3/2}}{MV^{3/2}} \int_0^\infty \mathrm{d}\mathbf{r}\, \mathbf{r}^2 \mathrm{e}^{-\mathbf{r}} \int_{-1}^1 \mathrm{d}\nu\, \mathrm{e}^{-i\mathbf{k}\mathbf{r}a_0\nu}. \tag{4.16}$$

The integral over the angles equals to

$$\int_{-1}^1 \mathrm{d}\nu\, \mathrm{e}^{-i\mathbf{k}\mathbf{r}a_0\nu} = \frac{2}{\mathbf{k}\mathbf{r}a_0} \sin(\mathbf{k}\mathbf{r}a_0), \tag{4.17}$$

therefore

$$\mathcal{C} = \frac{16\pi^{3/2}\hbar^2\overline{a}a_0^{1/2}}{MV^{3/2}} \delta_{\overline{\mathbf{K}},\mathbf{K}+\mathbf{K}'} \frac{1}{\mathbf{k}} \int_0^\infty \mathrm{d}\mathbf{r}\, \mathbf{r}\mathrm{e}^{-\mathbf{r}} \sin(\mathbf{k}\mathbf{r}a_0). \tag{4.18}$$

The last integral is a standard integral, that can be found in the tables of integrals, and it equals to

$$\int_0^\infty \mathrm{d}\mathbf{r}\, \mathbf{r}\mathrm{e}^{-\mathbf{r}} \sin(\mathbf{k}\mathbf{r}a_0) = \frac{2\mathbf{k}a_0}{\left(1+a_0^2\mathbf{k}^2\right)^2}. \tag{4.19}$$

Therefore the final result is

$$\mathcal{C} = \frac{32\pi^{3/2}a_0^{3/2}\hbar^2\overline{a}}{MV^{3/2}} \frac{1}{\left(1+a_0^2\mathbf{k}^2\right)^2} \cdot \delta_{\overline{\mathbf{K}},\mathbf{K}+\mathbf{K}'}. \tag{4.20}$$

The quadruple sum over the intermediate wave vectors

Further we deal with the quadruple sum over the intermediate wave vectors in order to derive the integrated form of the radiation power $I(h\nu)$. We use the expression of the matrix element of Coulomb interaction (4.20) derived

in the previous section. The radiation power expression (4.3) now become

$$I(h\nu) = \frac{2\pi}{\hbar}\frac{1}{\left(E_0^{1S}-h\nu\right)^2}h\nu\rho(h\nu)A^2N_{1S}^2\frac{2^6\pi a_0^3\overline{a}^2}{V^3}\frac{16\pi^2\hbar^4}{M^2}\left(\frac{2\pi\hbar^2}{Mk_BT}\right)^3$$
$$\times\sum_{\mathbf{K}}\sum_{\mathbf{K}'}\sum_{\mathbf{k}}\sum_{\overline{\mathbf{K}}}\frac{1}{\left(1+a_0^2\mathbf{k}^2\right)^4}\,\delta_{\overline{\mathbf{K}},\mathbf{K}+\mathbf{K}'}\,\mathrm{e}^{-\hbar^2\mathbf{K}^2/2Mk_BT}\,\mathrm{e}^{-\hbar^2\mathbf{K}'^2/2Mk_BT} \tag{4.21}$$
$$\times\delta\left(E_0^{1S}-E_x^b-h\nu+\frac{\hbar^2\mathbf{K}^2}{2M}+\frac{\hbar^2\mathbf{K}'^2}{2M}-\frac{\hbar^2\mathbf{k}^2}{2\mu}-\frac{\hbar^2\overline{\mathbf{K}}^2}{2M}\right).$$

The first sum over the $\overline{\mathbf{K}}$ can be eliminated due to the Kronecker δ by changing $\overline{\mathbf{K}}=\mathbf{K}+\mathbf{K}'$. Note, that in the argument of δ function the significant simplification occurs

$$\frac{\hbar^2\mathbf{K}^2}{2M}+\frac{\hbar^2\mathbf{K}'^2}{2M}-\frac{\hbar^2\overline{\mathbf{K}}^2}{2M}\longrightarrow-\frac{\hbar^2\mathbf{K}\cdot\mathbf{K}'}{M}. \tag{4.22}$$

The other three sums over the wave vectors are changed to integrals in standard way

$$\sum_{\mathbf{k}}\longrightarrow\frac{V}{8\pi^3}\int\mathrm{d}^3\mathbf{k}. \tag{4.23}$$

The expression of radiative power (4.21) then becomes

$$I(h\nu) = \frac{2\pi}{\hbar}\frac{1}{\left(E_0^{1S}-h\nu\right)^2}\frac{h\nu\rho(h\nu)A^2N_{1S}^2}{M^5V^3\left(k_BT\right)^3}2^9\pi^4a_0^3\overline{a}^2\hbar^{10}\cdot16\pi^2\int\mathrm{d}^3\mathbf{K}\int\mathrm{d}^3\mathbf{k}\int\mathrm{d}^3\mathbf{K}'$$
$$\times\frac{1}{\left(1+a_0^2\mathbf{k}^2\right)^4}\exp\left[-\frac{\hbar^2}{2Mk_BT}\left(\mathbf{K}^2+\mathbf{K}'^2\right)\right]\delta\left(E-\frac{\hbar^2\mathbf{K}\cdot\mathbf{K}'}{M}\right), \tag{4.24}$$

where we have assigned

$$E=E_0^{1S}-E_x^b-h\nu-\frac{\hbar^2\mathbf{k}^2}{2\mu}. \tag{4.25}$$

This quantity does not depend on $\mathbf{K}$ or $\mathbf{K}'$, therefore it is constant for integration over the wave vectors.

The integration over the $\mathbf{K}'$ may be calculated having in mind that δ function cuts out the plane in the three-dimensional space. The calculated

integral is

$$\int \mathrm{d}^3\mathbf{K}'\delta\left(E-\frac{\hbar^2\mathbf{K}\cdot\mathbf{K}'}{M}\right)\mathrm{e}^{-\hbar^2\mathbf{K}'^2/2Mk_BT}=\frac{2\pi M^2k_BT}{\hbar^2\mathbf{K}}\exp\left[-\frac{\hbar^2}{2Mk_BT}\frac{M^2E^2}{\hbar^4\mathbf{K}^2}\right]. \tag{4.26}$$

At this point two triple integrals over the wave vectors $\mathbf{k}$ and $\mathbf{K}$ left. Actually, these integrals are spherically symmetrical therefore the triple integrals can be changed to single. After application of changes we can write

$$\begin{aligned} I(h\nu)=\frac{2}{\pi^2}\frac{h\nu\rho(h\nu)A^2N_{1S}^2}{M^5\left(k_BT\right)^3}16a_0^3\overline{a}^2\hbar^9\frac{1}{\left(E_0^{1S}-h\nu\right)^2} \\ \times\int \mathrm{d}\mathbf{k}\,4\pi\mathbf{k}^2\int \mathrm{d}\mathbf{K}\,4\pi\mathbf{K}^2\left(1+a_0^2\mathbf{k}^2\right)^{-4}\frac{2\pi M^2k_BT}{\hbar^4\mathbf{K}} \\ \times\exp\left[-\frac{\hbar^2\mathbf{K}^2}{2Mk_BT}-\frac{ME^2}{2\hbar^2\mathbf{K}^2k_BT}\right]. \end{aligned} \tag{4.27}$$

After simplifications the expression becomes

$$\begin{aligned} I(h\nu)=\frac{2^{10}\pi\hbar^5a_0^3\overline{a}^2h\nu\rho(h\nu)A^2N_{1S}^2}{M^3\left(k_BT\right)^2}\frac{1}{\left(E_0^{1S}-h\nu\right)^2}\int_0^\infty \mathrm{d}\mathbf{k}\,\mathbf{k}^2\frac{1}{\left(1+a_0^2\mathbf{k}^2\right)^4} \\ \times\int_0^\infty \mathrm{d}\mathbf{K}\,\mathbf{K}\exp\left[-\frac{1}{k_BT}\left(\frac{\hbar^2\mathbf{K}^2}{2M}+\frac{1}{4}\frac{2M}{\hbar^2\mathbf{K}^2}\right)\right]. \end{aligned} \tag{4.28}$$

The integrals that left in the equation are not very complicated, however the variable exchange would simplify the work significantly. Instead of momentum $\mathbf{k}$ we introduce the variable ξ, which has the dimension of energy:

$$\begin{aligned} \xi&=\frac{\hbar^2\mathbf{k}^2}{2\mu}, \\ \mathbf{k}^2&=\frac{2\mu}{\hbar^2}\xi, \\ \mathbf{k}^2\mathrm{d}\mathbf{k}&=\frac{(2\mu)^{3/2}}{2\hbar^3}\xi^{1/2}\mathrm{d}\xi. \end{aligned} \tag{4.29}$$

Instead of momentum $\mathbf{K}$ we introduce dimensionless variable t:

$$\begin{aligned} t \cdot k_B T &= \frac{\hbar^2 \mathbf{K}^2}{2M}, \\ \mathbf{K} &= \frac{1}{\hbar} (2M k_B T)^{1/2} t^{1/2}, \\ \mathbf{K} \mathrm{d}\mathbf{K} &= \frac{1}{2\hbar^2} 2M k_B T \mathrm{d}t. \end{aligned} \tag{4.30}$$

After the introduction of exchanged variables to the expression (4.28) we obtain the final integral form

$$\begin{aligned} I(h\nu) = &\frac{2^9 \pi a_0^3 \overline{a}^2 A^2 h\nu \rho(h\nu) N_{1S}^2 (2\mu)^{3/2}}{M^2 k_B T} \frac{1}{\left(E_0^{1S} - h\nu\right)^2} \\ &\times \int_0^\infty \mathrm{d}\xi \, \frac{\xi^{1/2}}{(1+\xi/E_x^b)^4} \int_0^\infty \mathrm{d}t \, \exp\left[-t - \frac{1}{4t}\left(\frac{E}{k_B T}\right)^2\right]. \end{aligned} \tag{4.31}$$

Theoretically, there may be other types of exciton-exciton inelastic collision processes resulting with emission of photon. As it was noted before, there may be other types of exciton-exciton inelastic collision processes resulting with different state of one of interacting exciton and emitted photon after collision. The equation (4.31) was derived for the process (i). The integrals for other processes are derived in the same way as it was done for process (i), however with some modifications due to the differences in the exciton-exciton interaction. For process (ii), when one of interacting excitons is in excited state $E_{\mathbf{K}'}^{2S,2P}$ before the collision, the solution is the same as (4.31) only with few following replacements: $a_0 \to 2a_0$, $\overline{a} \to 2\overline{a}$, $N_{1S}^2 \to N_{1S} N_{2S,2P}$, and most important $E_x^b \to E_x^b/4$.

In process (iii), the two $E_{\mathbf{K}}^{1S}$ state excitons interact producing the photon and leaving the exciton in the same $E_{\mathbf{K}}^{1S}$ state. The integral solution for this type of interaction is

$$\begin{aligned} I(h\nu) = &\frac{2^5 \pi^2 \hbar^3 \overline{a}^2}{M^2} \cdot \frac{A^2 h\nu \rho(h\nu)}{\left(E_0^{1S} - h\nu\right)^2 + (\pi\alpha/\varepsilon)\left(E_0^{1S}\right)^2} \cdot \frac{N_{1S}^2}{k_B T} \\ &\times \int_0^\infty \mathrm{d}t \, \exp\left[-t - \frac{1}{4t}\left(\frac{E_0^{1S} - h\nu}{k_B T}\right)^2\right]. \end{aligned} \tag{4.32}$$

Note, that the single integration is applied because one of the product particles remain in the same excitonic state. For the process (iv) $(E_{\mathbf{K}}^{1S}, E_{\mathbf{K}'}^{1S}) \rightarrow (h\nu, E_{\mathbf{K}''}^{2S,2P})$, which should correspond to P_2-band, the solution for evaluation of radiative power spectrum is

$$I(h\nu) = \frac{2^5\pi^2\hbar^3\overline{a^*}^2}{M^2} \cdot \frac{A^2 h\nu \rho(h\nu)}{\left(E_0^{1S} - h\nu\right)^2 + (\pi\alpha/\varepsilon)\left(E_0^{1S}\right)^2} \cdot \frac{N_{1S}^2}{k_B T} \times \int_0^\infty \mathrm{d}t \exp\left[-t - \frac{1}{4t}\left(\frac{E_0^{1S} - (3/4)E_x^b - h\nu}{k_B T}\right)^2\right]. \tag{4.33}$$

First of all, the PL spectra for GaAs were calculated with the material parameters listed in Table 4.4 for optimisation of numerical calculation algorithm. The best results were achieved integrating from 10^{-4} to 10^3 eV with the increment of 1 meV. Fig. 4.11 a) shows the process (i) caused PL spectra dependence on temperature in the range from 5.8 to 81.4 K. The PL intensity decreases with temperature and PL peak position shifts to lower energy side. Also the characteristic for the (i) interaction process asymmetric broadening of the PL spectrum is evident with increase of temperature. In the Fig. 4.11 b), all four interaction processes are shown for GaAs, calculated using integral equations (4.31), (4.32) and (4.33). Due to the small GaAs exciton binding energy, the spectra are situated close to each other. The peak position of spectra are situated around the $E_0^{1S} - E_x^b$, $E_0^{1S} - (1/4)E_x^b$, E_0^{1S}, and $E_0^{1S} - (3/4)E_x^b$ for processes (i), (ii), (iii), and (iv), respectively.

The same integrals were evaluated for ZnO using material parameters listed in the Table 4.4. The calculated spectra as a function of temperature due to interaction process (i) are depicted in the Fig. 4.12 a). The evolution of spectrum with increasing temperature is the same as calculated for GaAs. However, as it is observed in the Fig. 4.12 b), due to the large exciton binding energy of ZnO, the calculated PL spectra are situated in the range of 60 meV, from $1S$ state exciton energy at E_0^{1S} to the energy at $E_0^{1S} - E_x^b$, where the process (i) caused PL spectrum is situated. Evidently, the exciton-exciton interaction caused spectral band due to the process (iii) correspond to the exciton radiative recombination spectral position. However, the P-band caused by process (i) is at exact photon energy of two exciton binding

Table 4.4: Parameter values for numerical calculation of radiation power of exciton-exciton collision in ZnO and GaAs.

Parameter	ZnO	Ref.	GaAs	Ref.
E_x^b (eV)	0.06	[2]	0.0041	[94]
E_0^{1S} (eV)	3.3771	[99],[5], [35]	1.5151	[94]
m_e^*	0.24 m_0	[100]	0.0665 m_0	[58]
m_h^*	0.59 m_0	[16]	0.139 m_0	[58]
μ	0.171 m_0		0.058 m_0	[44]
M_{ex}	0.83 m_0		0.267 m_0	
a_0 (Å)	80	[101]	136	[102]
$\pi\alpha/\varepsilon$	2.14×10^{-5}	[5]	3.2×10^{-5}	[94]
m_0 (kg)		9.10938×10^{-31}		
k_B (eV/K)		8.6173×10^{-5}		
$\hbar$ (eV·s)		6.58212×10^{-16}		
π		3.14159		

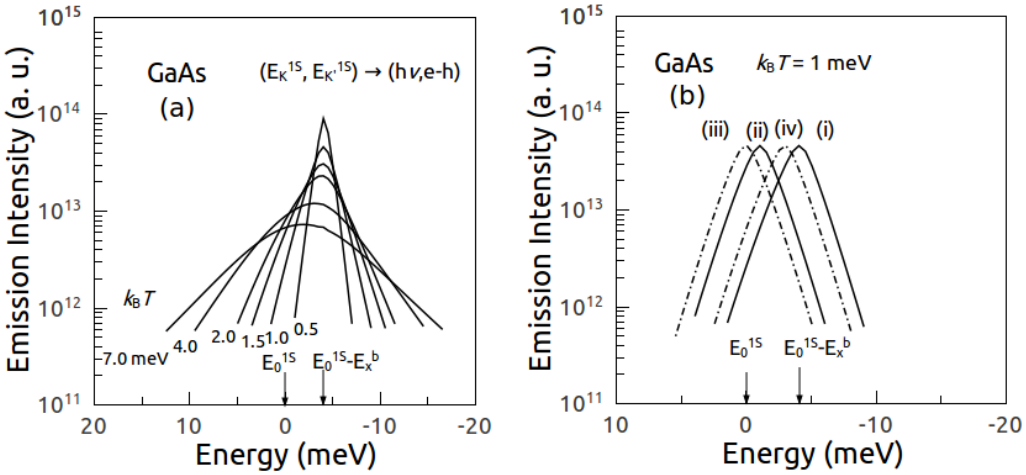

Figure 4.11: Calculated spontaneous emission spectra due to the process (i) at various temperatures for GaAs using equation (4.31) (a). Spontaneous emission spectra calculated for typical exciton-exciton collision processes at $k_BT = 1$ meV (b). The peak intensities are normalized. The photon energy is measured from the exciton energy E_0^{1S}.

energies apart from ZnO band gap E_g. As this spectral region is of our interest, the further discussion will continue on exciton-exciton interaction process (i).

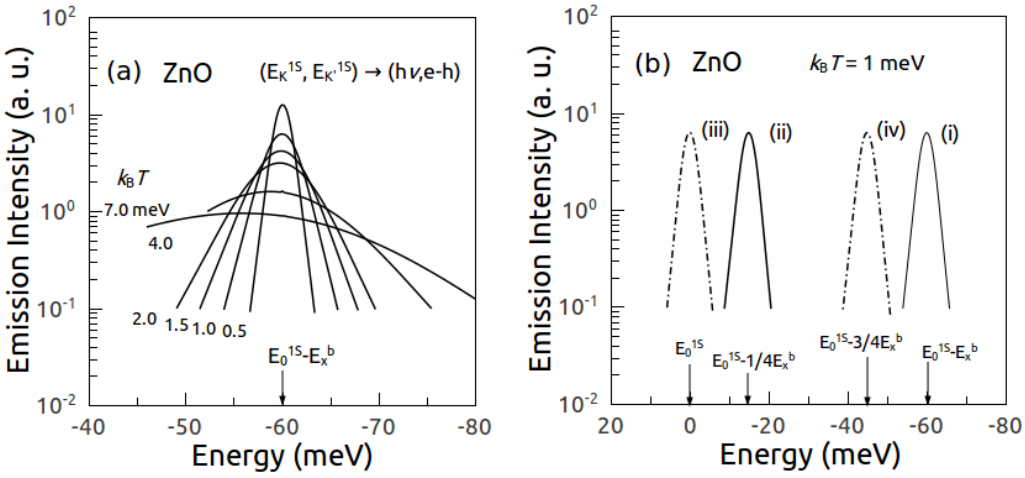

Figure 4.12: Calculated spontaneous emission spectra due to the process (i) at various temperatures for ZnO using equation (4.31) and ZnO material parameters (a). Spontaneous emission spectra calculated for typical exciton-exciton collision processes at $k_BT = 1$ meV (b). The peak intensities are normalized. The photon energy is measured from the exciton energy E_0^{1S}.

The collision of free and localized excitons

Lets repeat the calculation preformed in the recent section with the one of two interacting excitons localized at the centre of coordinates. In this case, the initial state is

$$|1S,\mathbf{K}\rangle|loc\rangle = \frac{1}{\sqrt{V}}\mathrm{e}^{i\mathbf{K}\mathbf{R}_1}\varphi_{1S}(\mathbf{r}_1)\cdot\delta(\mathbf{R}_2)\varphi_{1S}(\mathbf{r}_2), \tag{4.34}$$

where the $|loc\rangle$ is the initial state of localized exciton. The final state after collision of two excitons remains the same as before

$$|1S,0\rangle|\mathbf{k},\overline{\mathbf{K}}\rangle = \frac{1}{\sqrt{V}}\varphi_{1S}(\mathbf{r}_1)\cdot\frac{1}{\sqrt{V}}\mathrm{e}^{i\overline{\mathbf{K}}\mathbf{R}_2}\frac{1}{\sqrt{V}}\mathrm{e}^{i\mathbf{k}\mathbf{r}_2}. \tag{4.35}$$

The calculation of integral is more simple, because two δ functions eliminate the integral over mass centre coordinates. Therefore, using the same normalized integral over $\mathbf{r}_1$ (4.14) we have the new Coulomb matrix element

$$\mathcal{C} = \frac{4\pi\hbar^2\overline{a}}{MV^2}\int \mathrm{d}^3\mathbf{r}_2\,\mathrm{e}^{-i\mathbf{k}\mathbf{r}_2}\varphi_{1S}(\mathbf{r}_2) = \frac{32\pi^{3/2}a_0^{3/2}\hbar^2\overline{a}}{MV^2}\frac{1}{\left(1+a_0^2\mathbf{k}^2\right)^2}. \tag{4.36}$$

By repeating the steps of calculation in case of the interaction of free excitons, we write the radiation power expression for the case of the interaction of free and localized exciton

$$I(h\nu) = \frac{2\pi}{\hbar}\sum_{\overline{\mathbf{K}}}\sum_{\mathbf{K}}\sum_{\mathbf{k}} C^2A^2\frac{1}{\left(E_0^{1S}-h\nu\right)^2}h\nu\rho(h\nu)N_{loc}n_{\mathbf{K}}^{1S} \times\delta\left(E_{loc}+\frac{\hbar^2\mathbf{K}^2}{2M}-E_x^b-\frac{\hbar^2\overline{\mathbf{K}}^2}{2M}-\frac{\hbar^2\mathbf{k}^2}{2\mu}-h\nu\right), \tag{4.37}$$

where N_{loc} is the mean occupation number of localized excitons, and E_{loc} is the total energy of localized exciton $E_{loc} = E_0^{1S} - \Delta E_{loc}$. The ΔE_{loc} energy is the localization energy, what may be up to 10% of E_x^b energy in case of bound exciton. The argument of δ function reflects the energy conservation

$$E_{loc}+\left(E_0^{1S}+\frac{\hbar^2\mathbf{K}^2}{2M}\right) = h\nu+\left(E_0^{1S}+E_x^b+\frac{\hbar^2\mathbf{k}^2}{2\mu}+\frac{\hbar^2\overline{\mathbf{K}}^2}{2M}\right). \tag{4.38}$$

We use the free exciton concentration expression (4.5) and the Coulomb matrix element (4.36). Note, that the summation must be preformed over three momenta because one exciton is localized and its state is described. However, the Coulomb matrix element does not have the Kronecker δ, that reflects the momenta conservation. Therefore the difficulty of the summation over the momenta remains the same.

We have to calculate

$$I(h\nu) = \frac{2\pi}{\hbar}A^2N_{1S}N_{loc}\frac{h\nu\rho(h\nu)}{\left(E_0^{1S}-h\nu\right)^2}\frac{2^{10}\pi^3a_0^3\hbar^4\overline{a}^2}{M^2V^4}\left(\frac{2\pi\hbar^2}{Mk_BT}\right)^{3/2} \times\sum_{\overline{\mathbf{K}}}\sum_{\mathbf{K}}\sum_{\mathbf{k}}\frac{1}{\left(1+a_0^2\mathbf{k}^2\right)^4}\exp\left[-\frac{\hbar^2\mathbf{K}^2}{2Mk_BT}\right] \times\delta\left(E-\frac{\hbar^2\overline{\mathbf{K}}^2}{2M}\right), \tag{4.39}$$

where we denoted

$$E = E_{loc} + \frac{\hbar^2 \overline{\mathbf{K}}^2}{2M} - E_x^b - \frac{\hbar^2 \mathbf{k}^2}{2\mu} - h\nu. \tag{4.40}$$

First, we perform integration over $\overline{\mathbf{K}}$

$$\frac{V}{8\pi^3} \int \mathrm{d}^3\overline{\mathbf{K}}\, \delta\left(E - \frac{\hbar^2 \overline{\mathbf{K}}^2}{2M}\right) = \frac{VM^{3/2}E^{1/2}}{\sqrt{2}\pi^2\hbar^3}. \tag{4.41}$$

Second, we introduce the variable exchange as before. Instead of momentum $\mathbf{k}$ we introduce the variable ξ with the energy dimension and instead of the momentum $\mathbf{K}$ we introduce the dimensionless variable t:

$$\begin{aligned} \xi &= \frac{\hbar^2 \mathbf{k}^2}{2\mu}, \\ t \cdot k_B T &= \frac{\hbar^2 \mathbf{K}^2}{2M}. \end{aligned} \tag{4.42}$$

Then the final result is

$$\begin{aligned} I(h\nu) = \frac{2^{11}}{\sqrt{\pi}\hbar^3} \frac{\mu^{3/2}}{VM^{1/2}} a_0^3 \overline{a}^2 N_{1S} N_{loc} A^2 \frac{h\nu\rho(h\nu)}{\left(E_0^{1S} - h\nu\right)^2} \\ \times \int_0^\infty \mathrm{d}\xi\, \xi^{1/2} \frac{1}{\left(1 + \xi/E_x^b\right)^4} \int_0^\infty \mathrm{d}t\, t^{1/2} \mathrm{e}^{-t} \sqrt{E_{loc} - E_x^b - h\nu - \xi + tk_B T}. \end{aligned} \tag{4.43}$$

The numerically calculated spectra using the solution (4.43) with the energy of localized exciton $\Delta E_{loc} = E_0^{1S} - E_{loc} = 1$ meV are depicted in Fig. 4.13 a). The spontaneous emission spectra of inelastic localized exciton interaction with free exciton are strongly asymmetric. The long lower energy side of the spectrum does not depend on temperature. The higher energy side of the spectrum has a sudden fall forming the steep edge of the spectrum. The strong asymmetry is caused due to the Dirac δ wave functions of localized exciton. Because of that, the interaction potential, which is very complicated in case of two exciton, might not be chosen correctly.

In contrast to the lower energy side, the higher energy side of the calculated spectrum has strong dependence on temperature. With the temperature increase the high energy side of the spectrum becomes smoother. However, the peak position and intensity does not change with temperature

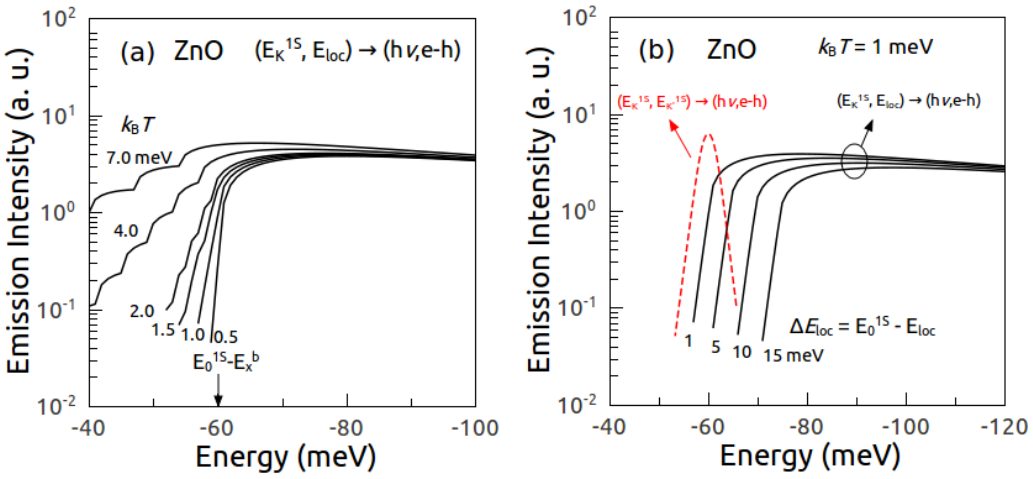

Figure 4.13: Calculated PL spectra of inelastic collision of free exciton with localized exciton using the equation (4.43). The PL spectra dependence on temperature for exciton with the localisation energy $\Delta E_{loc} = 1$ meV (a). The PL spectra dependence on ΔE_{loc} (solid lines) with respect to PL spectrum of free excitons interaction (dotted line) (b).

significantly.

In Fig. 4.13 b), the calculated spectra for free excitons collision process and for localized to free excitons collision process are depicted at fixed temperature of $k_B T = 1$ meV. Evidently, by changing localization energy ΔE_{loc} of exciton, the spectrum shifts to the higher energy side by the value of ΔE_{loc}. Note, that the emission peak position of the PL spectra with localized exciton contribution does not coincide with the actual energy of the free exciton-exciton interaction emission peak reduced by localization energy: $(E_0^{1S} - E_x^b) - \Delta E_{loc} \neq E_{PL}(E_{\mathbf{K}}^{1S}, E_{loc})$.

In Fig. 4.14, the calculated spontaneous emission spectra due to the exciton-exciton inelastic interaction are compared with the experimentally measured PL spectra at high excitation conditions. The emission spectra caused by inelastic interaction of free exciton with localized exciton are calculated with the ΔE_{loc} bound energy values from 1 to 15 meV. However, the usual energy difference between FX and D^0X bound excitons is more than 20 meV. Therefore, the calculated spectra are situated at the expected energy position and coincide with the experimentally measured P-band's energy position. The emission spectrum of free excitons radiative collision marks the theoretical position of the P-band.

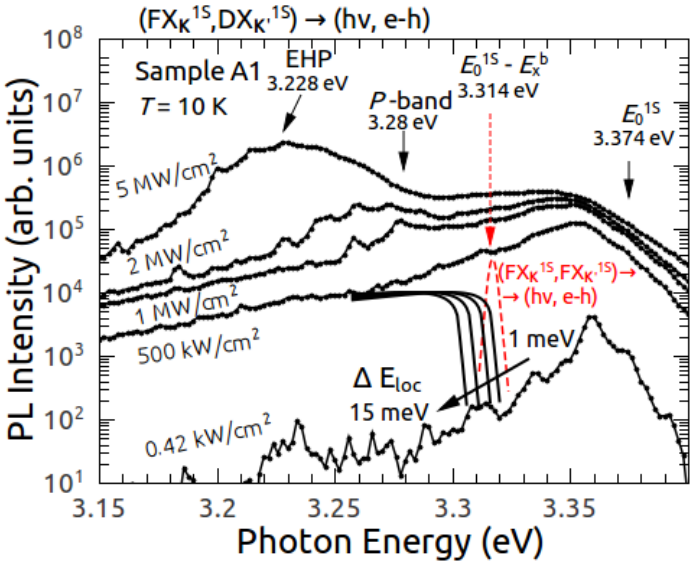

Figure 4.14: Calculated spontaneous emission spectra in comparison with experimentally measured PL spectra of sample A1 (dots) at 10 K temperature. The emission spectra caused by inelastic interaction of free exciton with localized exciton (solid line) are calculated with the $\Delta E_{loc} = E_0^{1S} - E_{loc}$ localization energy values of 1 meV, 5 meV, 10 meV and 15 meV. The emission spectrum of free excitons radiative collision (dashed line) marks the theoretical position of the P-band.

4.3 PL properties of highly conductive ZnO:Ga epitaxial layers

A group of Ga doped ZnO epitaxial layers were optically characterized. The samples contain different stacks of epitaxial layers and are schematically depicted in Fig. 4.15. The purpose of the Ga doped ZnO is to be applied in devices as highly conductive transparent n-type contact layers. Therefore, the ZnO:Ga layers are deposited on the top of various epitaxial stacks.

The highly conductive and transparent ZnO:Ga epitaxial layers were grown under metal-rich conditions with adjusted reactive oxygen pressure P_{O2} to incorporated metal (Zn + Ga) pressure ratio <1:1 [103]. The epitaxial layers were grown on the a-plane sapphire substrates by plasma-enhanced MBE at Virginia Commonwealth University (USA). The B4 sample was grown on c-plane sapphire substrate, while for B6 sample the Ga doped ZnO layer was deposited on the GaN based LED structure.

The ZnO:Ga epitaxial layers studied here are single crystal and highly

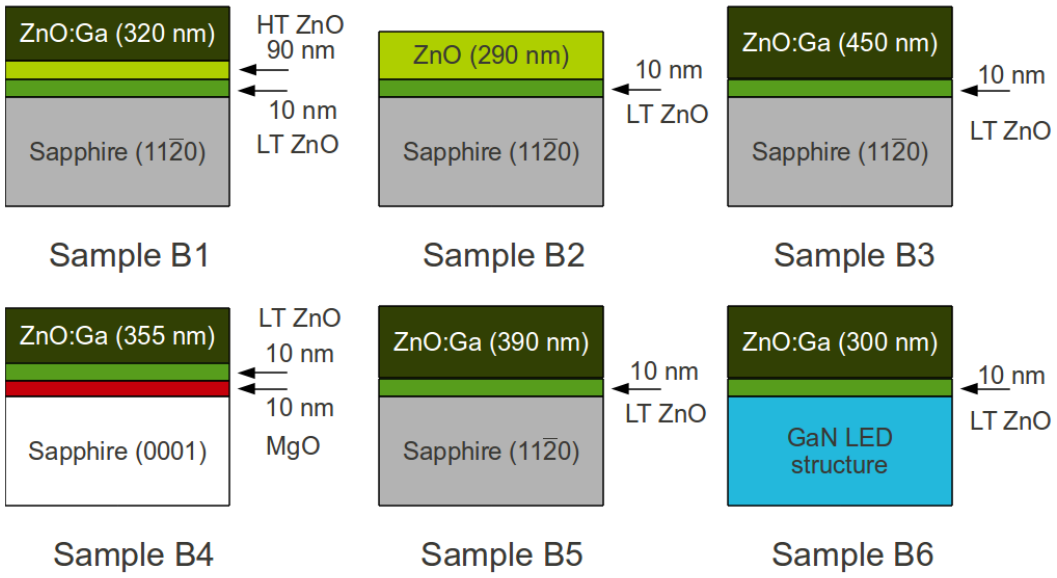

Figure 4.15: Schematic structure of Ga doped ZnO epitaxial layer samples. The sample B1 has high temperature ZnO epitaxial layer under the ZnO:Ga layer and sample B2 is the reference for sample B1. Other samples have various stacks of epitaxial layers under ZnO:Ga layer as indicated in the figure.

Table 4.5: Layer thickness d_{GZO}, carrier concentration n_e, and carrier mobility μ_e of Ga doped ZnO epitaxial layers. The concentration and mobility of electrons were measured by Hall experiment.

Samples	B1	B2	B3	B4	B5	B6
d_{GZO} (nm)	320	290	450	355	390	300
$n_e \times 10^{20}$ (cm^{-3})	9.2	0.001	6.9	4.8	5	5.3
μ_e (cm^2/V·s)	40	73	31	34	40	49

conductive with the electron concentration as high as 9.2×10^{20} cm^{-3}, the RT carrier mobility μ_e of ~ 41 cm^2/Vs, and the high transmittance exceeding 90% in the visible wavelength range. Detailed description of the growth procedure and studies of structural and electrical properties of the ZnO:Ga layers based on the temperature-dependant Hall measurements can be found elsewhere [104]. The thickness of the epitaxial layers d_{GZO}, electron concentration n_e and Hall mobility μ_e are given in Table 4.5.

In order to observe the defect related PL, the low excitation PL experiment was conducted as the defect related PL bands are usually saturated and obscured at high excitations. Apparently, the nominally undoped ZnO epitaxial layer of the reference sample B2 shows a broad, well-pronounced

deep recombination centres (DRC) band (Fig. 4.16) centred at 2.17 eV with a FWHM of 700 meV. The other PL band of the sample B2 spectrum is NBE emission peaking at the photon energy of 3.305 eV with a FWHM of 117 meV. The NBE band is quite asymmetrical having two lower energy side shoulders approximately at 3.27 eV and 3.19 eV photon energy.

The DRC band in the sample B1 is very weak if compare to the NBE band, which is consistent with the published data reporting that heavy doping of ZnO with Ga can drastically suppress the deep-level emission due to the screening effect in highly degenerate material [105, 106, 107]. The DRC band has the peak intensity at around 2.425 eV. The NBE band at 3.275 eV from the sample B1 is broader (FWHM ∼295 meV) and even more asymmetric with extended lower energy side if compare to the NBE band from the reference sample B2. This may be caused by radiative recombination through the DOS tales which are created by large amount of shallow defects in the doped ZnO epitaxial layer [107]. The PL band on the higher energy side from ZnO NBE emission band has been observed. The higher energy (HE) PL band is centred at 3.51 eV and its FWHM is of about 202 meV. Since the NBE and HE PL bands are overlapping, the FWHM values were estimated by the deconvolution method with the percent error not more than 12%.

To gain insight into the origin of the HE line in the sample B1, the de-

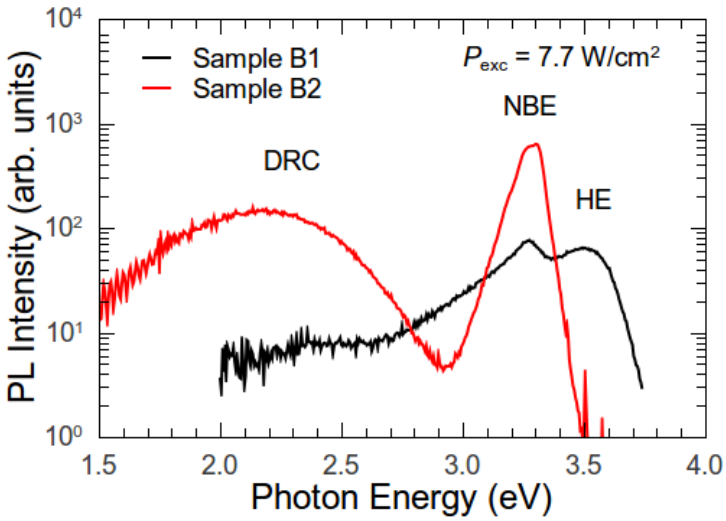

Figure 4.16: RT PL spectra of Ga doped ZnO and undoped ZnO epitaxial layers of samples B1 and B2 measured under low excitation.

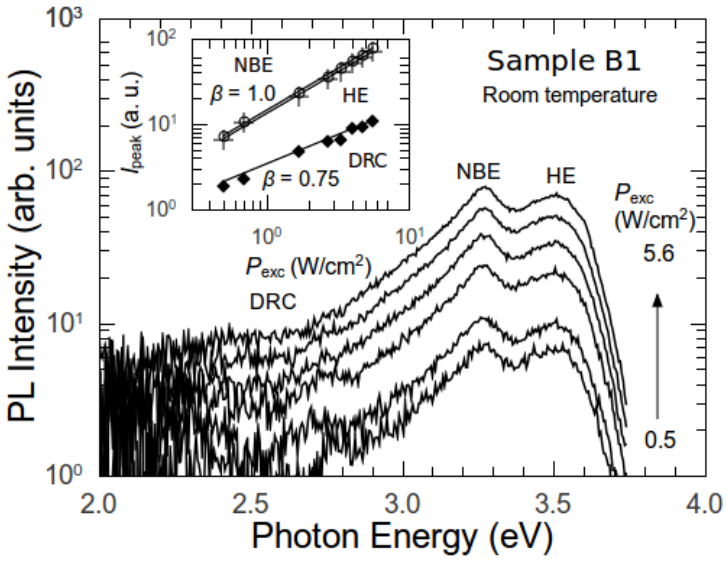

Figure 4.17: PL spectra dependence on excitation power density for the sample B1 measured at RT. The inset shows the PL peak position dependence on excitation power density P_{exc} of NBE (empty ellipses), HE (crosses) and DRC (filled diamonds) PL bands.

pendence of PL intensity on excitation power density was measured at the low excitation level. The excitation power density was changed in the range from 0.5 W/cm^2 to 5.6 W/cm^2. The results are shown in the Fig. 4.17. At the lowest excitation level a new PL line appears, which is obscured by the broad NBE PL band. This band is centred at 2.76 eV, in region characteristic for DRC-related emission. In fact it is possibly Cu-related green line. However, it is to weak to identify properly. As it is shown in the inset of Fig. 4.17, the PL peak intensity of the NBE and HE bands increases with excitation power density with the rate $\beta = 1$. This finding suggests that both PL bands are either band-to-band radiative recombination transition or free exciton radiative recombination transition. The DRC related PL band depends on excitation power density with the rate $\beta = 0.75$. The estimated intermediate DRC band rate may be due to the overlapped DRC and NBE PL bands.

The PL spectra dependence on temperature of the sample B1 is shown in Fig. 4.18. The NBE line at low temperatures clearly shows excitonic nature. The dominant PL line at 3.358 eV (8.1 K temperature) is the neutral donor bound exciton (D^0X) radiative transition. However, the line has higher

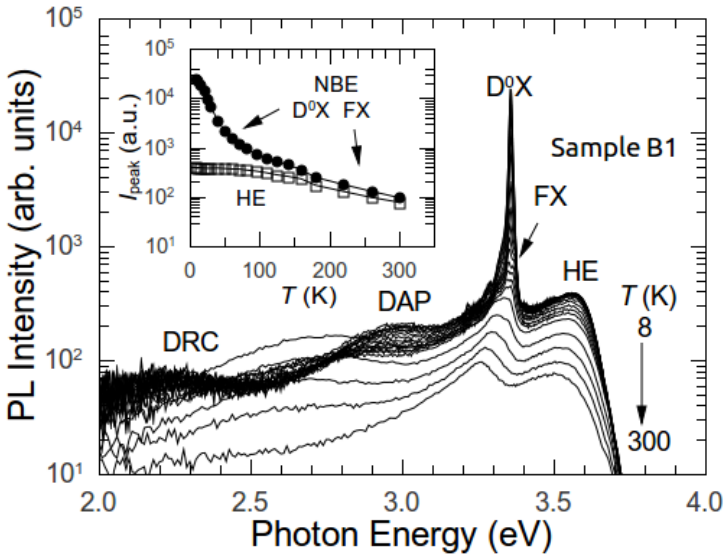

Figure 4.18: PL spectra dependence on temperature of sample B1 under CW excitation. Inset shows the peak intensity dependence on temperature for NBE (filled ellipses) and HE (empty squares) PL lines.

energy shoulder at 3.372 eV what is the exact energy of low temperature free exciton (FX) transition. The two longitudinal optical phonon replicas (LO1 and LO2) are at 3.288 eV and 3.216 eV photon energies, what is 70 and 142 meV apart from the D^0X PL line. In the temperature range from 100 to 150 K, the FX line overcomes the D^0X line by intensity due to dissociation of donor bound excitons, what is typical behaviour for ZnO and as well as GaN. The DRC band at low temperature is situated at 3.02 eV and the FWHM is $\sim$ 0.55 eV. However, at 160 K temperature the DRC band experiences sudden shift to lower energies and the increase in intensity. This may be related with thermal activation of DRC.

Based on the excitation- and temperature-dependent PL measurements, it is proved the excitonic nature of the 3.27 eV line, while the band at 3.51 eV can be attributed to the free electron-hole plasma in highly degenerate ZnO:Ga layer. The position of HE line well correlates with the blue shift of 255 meV of the absorption edge observed in other degenerate ZnO:Ga samples with similar electron concentrations. The coexistence of two bands in the PL spectrum of highly Ga doped ZnO layers should be discussed in more details. Since the carrier density in the ZnO:Ga layer of sample B1 is 9.2×10^{20} cm^{-3}, the existence of excitons in the layer is unlikely, as

the Mott density for ZnO is around 3.7×10^{19} cm^{-3}. Therefore, the NBE band probably originates from the underlying 90 nm thick ZnO epitaxial layer. On the other hand, the ZnO:Ga epitaxial layer is 320 nm thick and the penetration depth for excitation light is around 65 nm (the absorption coefficient for $\lambda_{exc} = 325$ nm is $\alpha = 1.6 \times 10^5$ cm^{-1} [16]). Therefore, the excitation of underlying ZnO layer is hardly possible.

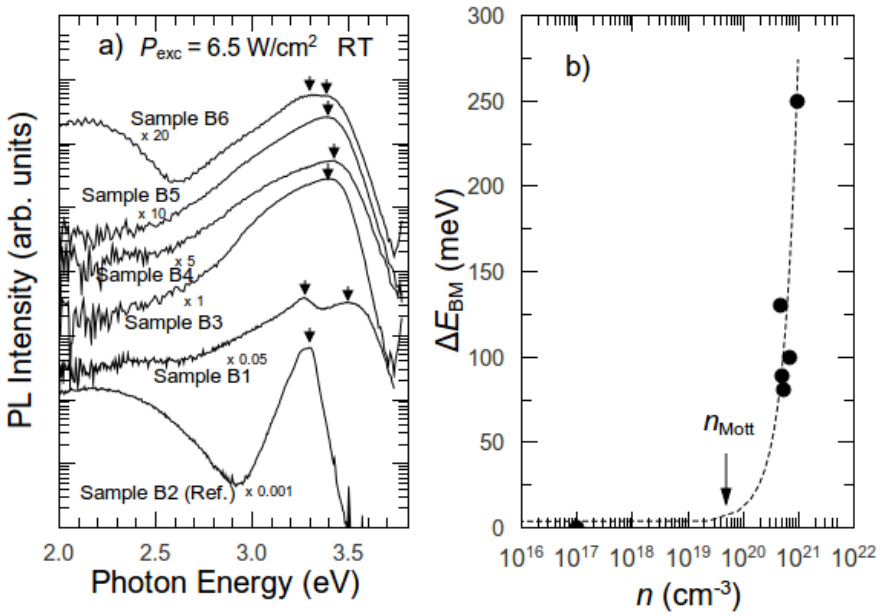

Figure 4.19: PL spectra of ZnO:Ga epitaxial layers on various epitaxial layer stacks and substrate orientations measured under CW excitation at RT (a). The Burstein-Moss energy shift of the HE band from the free excitons band ΔE_{BM} dependence on the electron concentration n (b). The Mott concentration is marked with the arrow. The doted line is a guide for the eye.

To gain more knowledge about the measured phenomenon, more samples were measured. The structure of the samples are depicted in the Fig. 4.15. The selected samples does not have high temperature grown ZnO layer underneath the ZnO:Ga epitaxial layer. Therefore if the free exciton emission arises from the undoped ZnO layer, as it is the case of sample B1, it would not be present in the other samples. The PL spectra are compared in the Fig. 4.19(a). All highly conductive Ga doped ZnO layers exhibit the PL peak with the Burstein–Moss shift about 100 meV to the higher energy side. Apparently, every other sample without high temperature grown ZnO

epitaxial layer underneath the Ga doped ZnO epitaxial layer has carrier concentration higher than Mott density and is degenerated. Therefore one can conclude that the 3.27 eV PL band in the PL spectrum of sample B1 originates from the underlying ZnO epitaxial layer. In the Fig. 4.19(b), The Burstein-Moss energy shift of the HE band from the free excitons band ΔE_{BM} dependence on the electron concentration n is depicted. Evidently, the emission band shift to the higher energy side is greater for the more degenerated samples with higher carrier concentration as the quasi-Fermi level of electrons penetrates more into the conduction band. This result coincide with the results reported in the literature [106, 107].

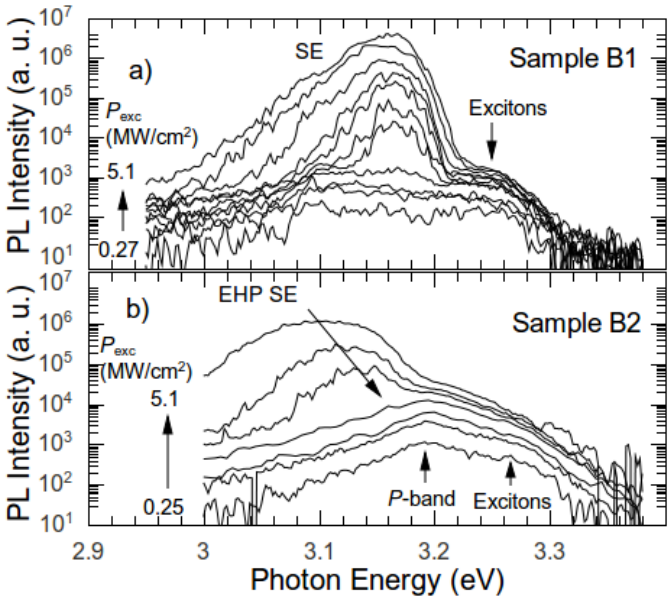

Figure 4.20: PL spectra dependence on excitation power density under high excitations for samples B1 and B2. The SE appears at elevated excitations at 3.15 eV and 3.11 eV photon energy.

At high excitation, created by 4th harmonic of pulsed YAG:Nd^{3+} laser ($\lambda_{exc} = 266$ nm, $\tau_{exc} = 4$ ns), the SE lines appear (Fig. 4.20) with a threshold excitation power densities of 1.2 MW/cm^2 and 0.86 MW/cm^2 (Fig. 4.21) for the reference sample B2 and the sample B1 with ZnO:Ga layers, respectively. At relatively lower excitation, the P-band was also detected at 3.196 eV (69 meV apart from spontaneous emission peak) for the ZnO epitaxial layer of sample B2. The P-band emission is attributed to the radiative recombination of an exciton-exciton collision process. It is worth noting that

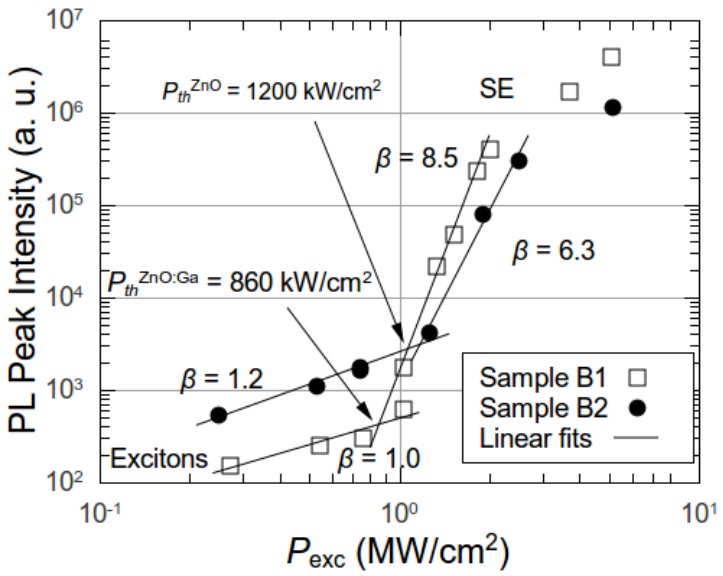

Figure 4.21: Integrated PL intensity dependence on excitation power density P_{exc} in double logarithmic scale. The threshold values of excitation power density for SE are shown with arrows.

the peak position of SE lines in the sample B2 and sample B1 is quite different — 3.13 eV and 3.168 eV, respectively. The SE line around 3.13 eV is due to the electron-hole plasma (EHP). The optically pumped SE has been observed by many researchers for undoped ZnO grown by a variety of methods. However, only one study of the SE lines in ZnO:Ga ($n = 10^{18}$ cm^{-3}) has been reported [108]. The SE lines in ZnO:Ga did not exhibit red shift as typically observed for the EHP SE in nominally undoped ZnO layers. The broadening of SE lines under high excitation is due to the accumulation of higher density of carriers and strong saturation of OG.

The OG spectra measured applying the VSL technique are shown in Fig. 4.22. The OG spectrum of sample B1 has maximum value of 190 cm^{-1} at the photon energy 3.145 eV and the shoulder of 130 cm^{-1} value at 3.17 eV. Therefore, we observe overlapped OG spectrum of two mechanisms: the EHP OG and exciton-exciton interaction caused OG. If compare to the reference sample B2, the maximum OG coefficient is only 60 cm^{-1} by value peaked at 3.14 eV. Also recall, that the threshold excitation power densities for SE are 0.86 MW/cm^2 and 1.2 MW/cm^2 (Fig. 4.21) for samples B1 and B2, respectively. Therefore the Ga doped ZnO epitaxial layer plays important role for improving the conditions for SE to occur. It is possible, that photo-excited holes are injected through the interface between the

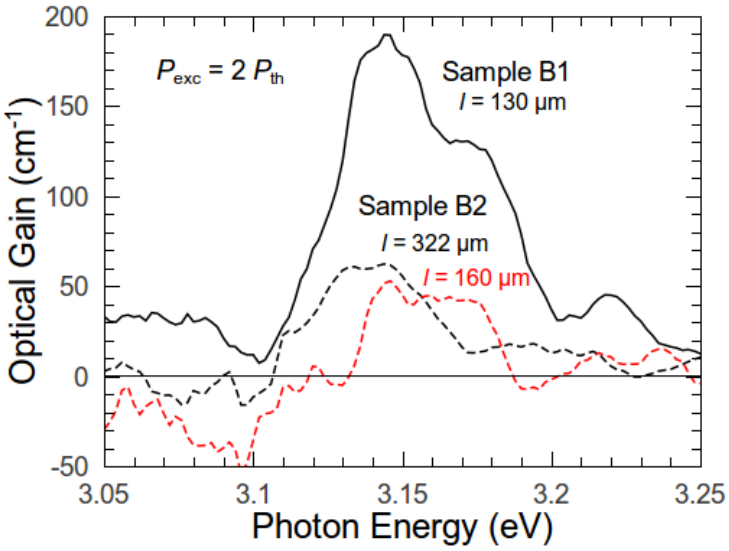

Figure 4.22: OG spectra of sample B1 (with the ZnO:Ga epitaxial layer on the high temperature grown ZnO thin epitaxial layer) and sample B2 (only high temperature grown ZnO epitaxial layer) measured in the VSL technique. The OG spectra with highest OG values were selected for comparison.

ZnO:Ga and ZnO epitaxial layers and support the population inversion in the ZnO epitaxial layer.

4.4 Optical characterization of ZnO:N films grown by DC magnetron sputtering

The N doped ZnO thin films were deposited by DC magnetron sputtering at Kaunas University of Technology. Two samples were prepared for PL experiment for optical characterization of the films. The structure of the samples is depicted schematically in the Fig. 4.23. Sample C1 is the N doped ZnO thin film grown on lime glass substrate, while sample C2 is the N doped ZnO grown on Si substrate under the same partial oxygen pressure $p_{O2} = 1.7 \times 10^{-2}$ Pa. The residual gas pressure in the growth chamber was 7×10^{-3} Pa. The working pressure was kept constant $p_{Ar+O2+N2} = 2 \times 10^{-1}$ Pa by adjusting oxygen and nitrogen gas flows. The substrate temperature was set to 230 °C before the growth. This substrate temperature is relatively low for ZnO growth and it is more likely to obtain the polycrystalline ZnO films [109]. The deposition was performed with a

constant discharge current density of 8 mA/cm^2. The current density from plasma of the unbalanced magnetron to substrate was around -3.5 mA/cm^2. The thickness of films estimated from cross-section SEM images is $\sim$0.5 µm. The details on growth equipment, sample preparation, electrical and optical properties can be found elsewhere [25, 55].

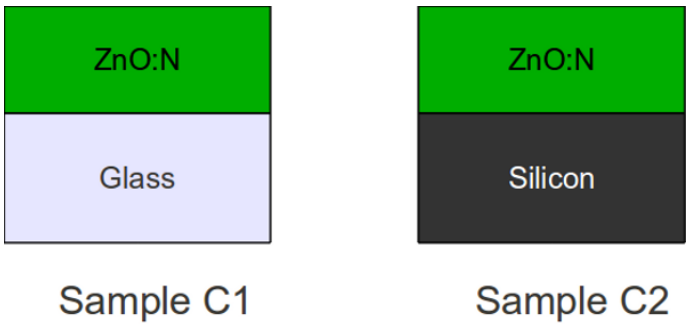

Figure 4.23: Structure of N doped ZnO thin films on the lime glass (sample C1) and the Si (sample C2) substrates grown by DC magnetron sputtering.

The PL experiment was carried out in quasi-stationary excitation regime exciting with pulsed YAG:Nd^{3+} laser. The excitation power density was $\sim$1.5 MW/cm^2. The PL spectra of the ZnO:N films are shown in Fig. 4.24 and Fig. 4.25 for samples C1 and C2, respectively. The room temperature PL spectra consist of one predominant broad line at the NBE spectral region with the peak energy of 3.23 eV for both samples. The only difference is the FWHM which is 259 meV and 274 meV for ZnO:N thin films on glass and Si substrates, respectively. The attention was concentrated on the NBE spectral region of ZnO while the natural ZnO DRC PL bands in yellow-green spectral region were not observed.

The PL spectra were measured also from the other side of the sample plate in order to reveal the possible contribution of the substrate. Such PL spectra are depicted in Fig. 4.24 and Fig. 4.25 as curves (c). As can be seen, the sample C1 has some emission from substrate side in a given spectral range. It is a wide band with the FWHM of about 1.173 eV and maximum at 3.255 eV, which is nearly to the peak position of PL spectrum of ZnO:N film. This could be the PL spectra of the film-substrate interface as the glass substrate is transparent for excitation wavelength. Such interface should be

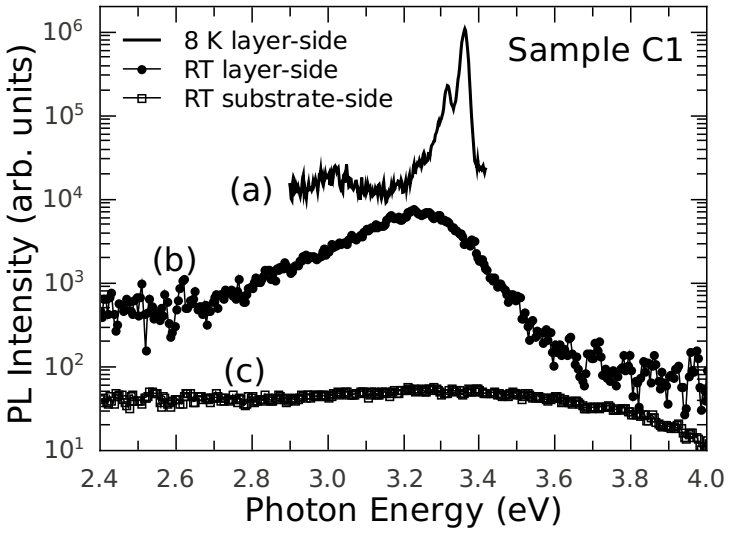

Figure 4.24: PL spectra of ZnO:N film on the glass substrate at 8 K (a) and RT (b); curve (c) demonstrates PL spectrum from back-side of the sample. Spectra are arbitrary shifted in intensity scale.

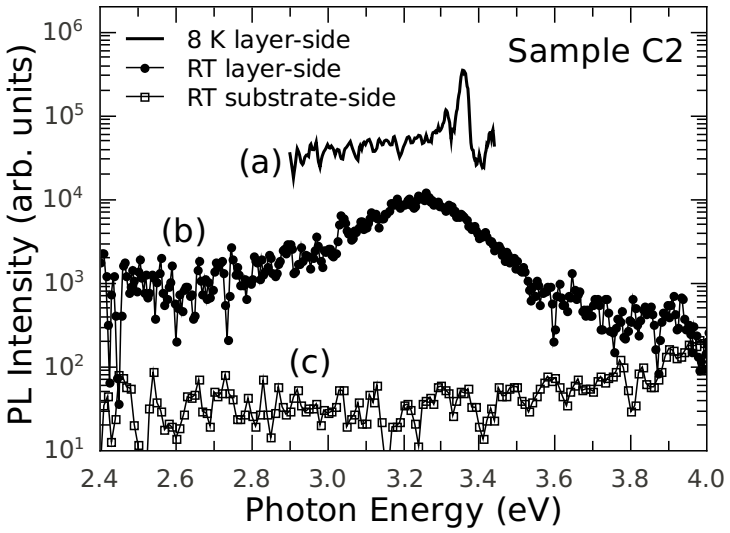

Figure 4.25: PL spectra of ZnO:N film on the Si substrate at 8 K (a) and room temperature (b); curve (c) demonstrates PL spectrum from back-side of the sample. Spectra are arbitrary shifted in intensity scale.

very disordered what explains broadened PL band. Meanwhile, in the case of sample C2 there is no noticeable radiation in a given spectral range when measuring from the substrate side of the sample C2.

The ZnO:N film PL spectra at 8 K show two clearly resolved lines at 3.362 and 3.315 eV. The FWHM of the dominant line is 19 and 25 meV for

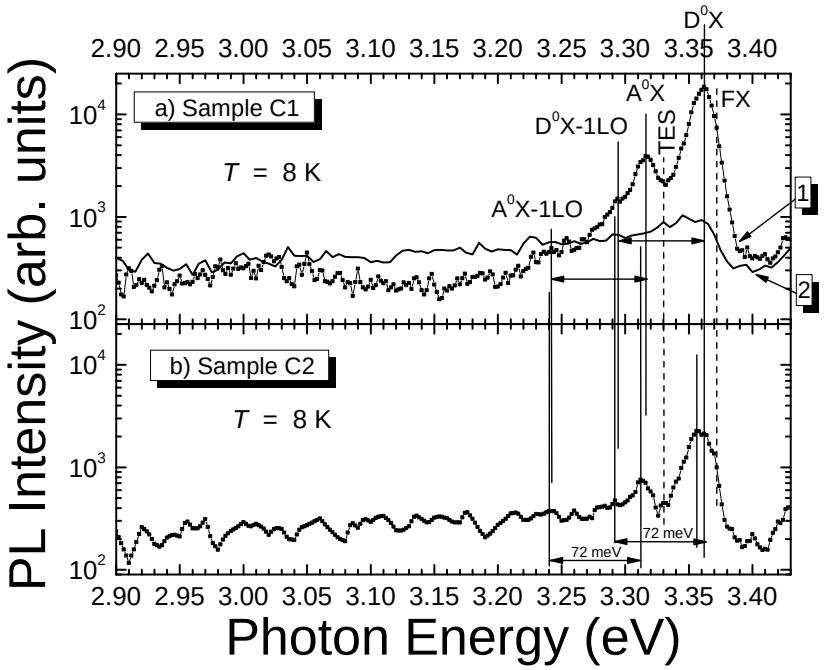

Figure 4.26: Detailed view of the NBE PL spectra of the ZnO:N films at 8 K. The spectral lines are denoted as follows: FX is a free exciton line at 3.372 eV; D^0X is a line of bound exciton related to neutral donor at 3.362 eV; TES marks two electron satellites at 3.330 eV; A^0X is a neutral acceptor related bound exciton line at about 3.314 eV; 1LO's mark the first replicas of the longitudinal optical phonon assisted bound exciton recombination lines shifted by 72 meV toward low energy side from D^0X and A^0X lines. Spectra denoted as 1 and 2 are from the newly-cut and as-it-is areas of the sample C1, respectively.

samples C1 and C2, respectively. This demonstrates rather poor quality of ZnO:N films comparing, for example, to 3 meV value of FWHM of MBE-grown ZnO epilayer on a sapphire substrate [6]. Detailed view of the low temperature PL spectra is illustrated in Fig. 4.26. The most intense two lines can be attributed to the radiative recombination of the bound excitons at neutral donors (D^0X) and neutral acceptors (A^0X). These two lines have LO phonon replicas shifted toward low energy side by 72 meV with respect to the main lines. Weak free exciton emission (FX) can also be observed on the higher energy side of D^0X line as a light shoulder at 3.372 eV. The line at 3.33 eV is attributed to the two electron satellite (TES) transition. The excitation of neutral donor from initial state to excited $1S$ state during

the radiative recombination of the donor bound exciton (also possible $2S$ or $2P$ final states with the result of more adequate TES lines in PL spectra) is the mechanism behind this PL line. The dominant D^0X line is a result of several overlapping PL lines [15]. We were able to resolve these lines at 3.362, 3.356, and 3.344 eV by using the detection system with spectral resolution of less than 5 meV. All these lines are typical for the undoped bulk ZnO single crystals and are attributed to the intrinsic shallow donors. The relatively weak FX line and intense A^0X line evidence lower quality of the films and higher density of shallow acceptors in both ZnO:N films in comparison with the bulk ZnO films. The clearly pronounced A^0X line is probably caused by nitrogen created states in ZnO matrix [16].

It also should be noted that PL signal from ZnO:N films was relatively weak when excitation beam was focused on the as-it-is sample surface. The PL signal increased nearly 20 times in magnitude (compare spectra 1 and 2 in Fig. 4.26 a) when focused excitation beam was aimed at newly-cut area of sample surface. It gives an idea about strong surface recombination. This effect significantly depreciates the radiative properties of tested ZnO:N samples.

For conclusion, the PL spectra revealed poor radiative properties and confirmed lower structural quality of ZnO:N thin films grown by DC magnetron sputtering at low growth temperature. Low temperature PL spectra possess relatively intense A^0X line at 3.314 eV which is a signature of nitrogen caused shallow neutral acceptor states in ZnO.

5 Exciton localization effects in MgZnO epitaxial layers

The PL investigation on the MBE grown $Mg_xZn_{1-x}O$ epitaxial layers revealed the *S*-shaped PL peak position dependence on temperature. This behaviour is attributed to carrier localization in randomly distributed potential field minima and it is usual effect in ternary and quaternary semiconductor epitaxial layers and QWs. To the best of our knowledge, first time two blue-shifts of the PL peak position dependence on temperature for samples with high Mg content x in $Mg_xZn_{1-x}O$ alloys are analysed and described. The model of band-filling of two energy separated Gaussian-like tails of DOS is suggested. The origin of potential field fluctuations as localization centres is inhomogeneous distribution of Mg in ternary alloy. The localized excitons are prevented from escaping the Mg rich areas in the crystal and the probability to be trapped in the non-radiative recombination centres is significantly reduced. As a result, the enhancement of PL intensity is observed and this effect is useful for efficient optoelectronic devices based on MgZnO epitaxial layers.

In this chapter, the results of the investigation on $Mg_xZn_{1-x}O$ epitaxial layers with different Mg content in the alloys by means of SEM, XRD, EDX, AFM, PL, and SNOM are presented. In the first section, the samples preparation procedure is presented with some experimental data about crystal quality of the grown epitaxial layers. The second section is devoted to PL analysis and the discussion on the observed double *S*-shape of the PL peak with the increasing temperature. In the third section, the model of two energy separated Gaussian-like DOS tails derived from the experimental data and the evidences of carriers distribution in localized states achieved by SNOM measurements with nano-scale lateral resolution are presented.

5.1 Growth of MgZnO epitaxial layers

The $Mg_xZn_{1-x}O$ epitaxial layer samples were prepared using MBE technique at Institute of Photonics and Optoelectronics of National Taiwan University. Epitaxial layers were grown on sapphire (0001) substrates with $\sim$ 10 nm thick MgO nucleation layers, while the sample D4 was grown on (0001) sapphire substrate with 2 µm thick GaN buffer layer, as shown in Fig. 5.1. The $\sim$ 100 nm thick ZnO buffer layers were deposited on the nucleation or buffer layer prior the growth of $Mg_xZn_{1-x}O$. The substrate temperature was set to 500 °C and the Zn effusion cell temperature was set to 290 °C during the growth of $Mg_xZn_{1-x}O$ epitaxial layers. The adjustable growth parameters were O_2 gas flow rate φ_{O2} and Mg effusion cell temperature T_{Mg}. The values of growth parameters are presented in the Table 5.1. For the samples with MgO nucleation layer, the growth duration of $Mg_xZn_{1-x}O$ epitaxial layers was 2 hours yielding thickness d_{MgZnO} about 100 nm. However, for sample D4 the growth process took $\sim$ 6 hours resulting the $Mg_xZn_{1-x}O$ epitaxial layer about 320 nm thick.

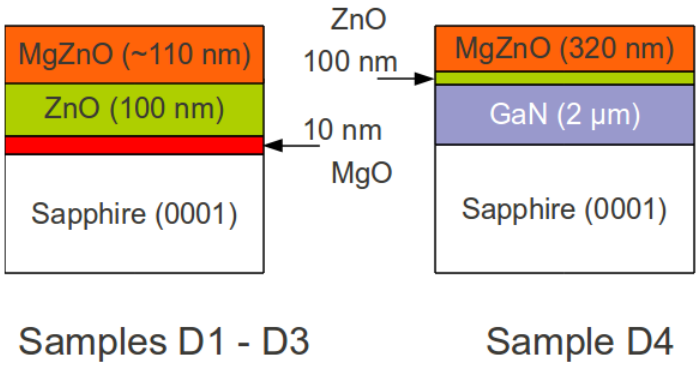

Figure 5.1: Schematic structure of $Mg_xZn_{1-x}O$ epitaxial layer samples. Samples D1, D2 and D3 have MgO nucleation and ZnO buffer layers, while sample D4 has GaN and ZnO buffer layers.

The thickness of the epitaxial layers was confirmed by cross-section SEM images. The cross-section SEM image of the sample D2 is depicted in the Fig. 5.2 and the visible layers are indicated as follows: the sapphire substrate, $\sim$ 10 nm MgO nucleation layer, $\sim$ 100 nm ZnO buffer layer, and the single phase homogeneous $Mg_{0.17}Zn_{0.83}O$ epitaxial layer of good crystal

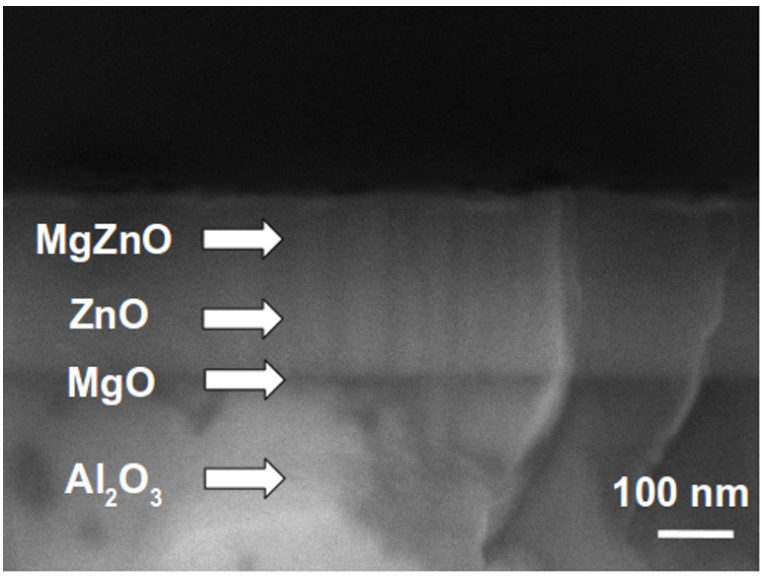

Figure 5.2: Cross-section SEM image of sample D2 shows the single-phase epitaxial $Mg_{0.17}Zn_{0.83}O$ layer. However, the columnar growth parallel to the *c*-axis can be traced in the image.

Table 5.1: Growth conditions for $Mg_xZn_{1-x}O$ epitaxial layers. The T_{Mg} is Mg effusion cell temperature and φ_{O2} is the O_2 gas flow rate. The d_{MgZnO} is the thickness of $Mg_xZn_{1-x}O$ epitaxial layers confirmed by cross-section SEM images.

Sample	D1	D2	D3	D4
T_{Mg} (°C)	310	370	345	345
φ_{O2} (sccm)	2.5	2.8	2.7	2.7
d_{MgZnO} (nm)	100	130	110	320

quality. However, the columnar growth can be traced parallel to the growth direction (*c*-axis), what may be the threading dislocations arising from the substrate and penetrating through the ZnO and $Mg_xZn_{1-x}O$ epitaxial layers up to the surface.

Consistently with cross-section SEM data, the XRD measurements also show the $Mg_xZn_{1-x}O$ epitaxial layers being of single phase and good crystal quality. In the Fig. 5.3, the ω-2Θ scan around (002) diffraction peak consist of the $Mg_{0.17}Zn_{0.83}O$ diffraction peak and ZnO diffraction peak with FWHM values 140 arcsec and 130 arcsec, respectively. The FWHM values are similar for both epitaxial layers, therefore the crystal quality of $Mg_xZn_{1-x}O$ epitaxial layers is as good as of ZnO buffer layers.

The EDX experiment was carried out to estimate the Mg content x in the $Mg_xZn_{1-x}O$ alloys. The estimated Mg content x in the alloys is 0.025,

0.17, 0.30, and 0.32 for samples D1, D2, D3, and D4, respectively. The high amount of Mg is close to the critical concentration that may lead to crystal lattice phase separation [73]. The phase separation emerges in the epitaxial layers with high amount of Mg and the co-existence of MgZnO in wurtzite and cubic lattices may be observed. However, the crystal structure experiments have not showed the evidences of possible phase separation. Moreover, recently the high quality single-phase wurtzite MgZnO epitaxial layers with up to 55% of Mg part in the alloys were reported [47, 110].

Table 5.2: Mg content x in the alloys measured by EDX and surface parameters of $Mg_xZn_{1-x}O$ epitaxial layers measured by AFM: R_{AFM} is the roughness, σ is the standard deviation and H denotes the peak-to-peak distance.

Sample	D1	D2	D3	D4
x (%)	2.5	17	30	32
R_{AFM} (nm)	2.3	5.8	9.1	2.8
σ_{AFM} (nm)	2.9	17.2	12.9	3.6
H (nm)	25	73	126	65

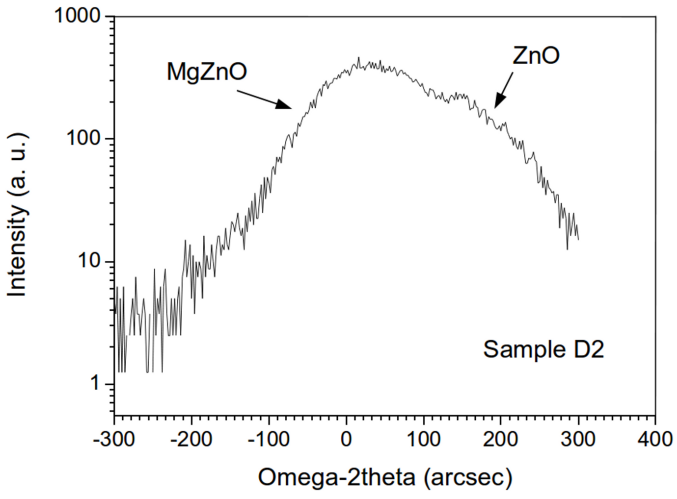

Figure 5.3: ω-2Θ rocking curve around the (002) diffraction peak of sample D2. The main $Mg_{0.17}Zn_{0.83}O$ diffraction peak has FWHM of 140 arcsec and the second ZnO diffraction peak has FWHM of 130 arcsec.

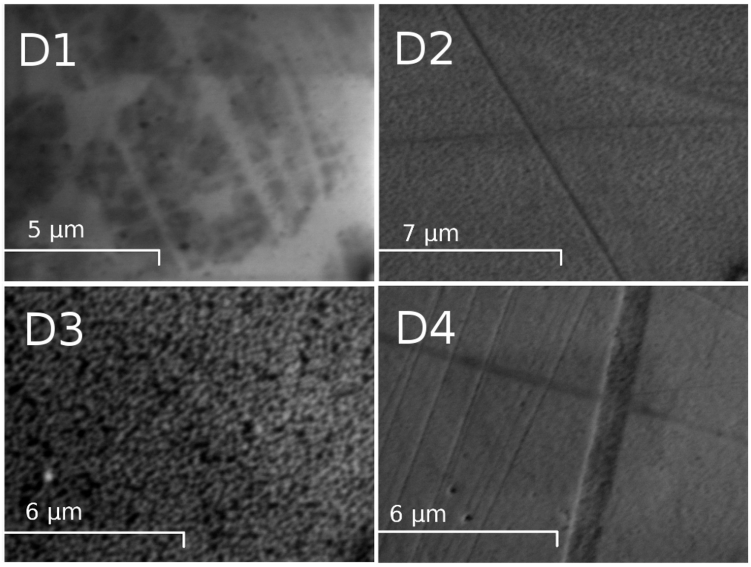

Figure 5.4: SEM images of the $Mg_xZn_{1-x}O$ epitaxial layer surfaces. The sample names are depicted on the corresponding images. The ditches in images D2 and D4 are mechanical scratches in sample surface.

The SEM images of the $Mg_xZn_{1-x}O$ epitaxial layers surfaces are shown in Fig. 5.4. By comparing the images one can say, that samples D1 and D4 have smooth and uniform surfaces, while the samples D2 and especially D3 have grainy profiles. The increase of Mg in the alloy reduces the crystal quality of the epitaxial layer. However, the $Mg_{0.32}Zn_{0.68}O$ epitaxial layer on the sapphire/GaN template has much better crystal quality if compare with the $Mg_{0.3}Zn_{0.7}O$ epitaxial layer on the MgO nucleation layer, even though the Mg part x in the alloys is very similar, however the thickness of the epitaxial layers differs.

The AFM experiment results shown in Fig. 5.5 are consistent with SEM images, only AFM allows to probe the surface with 10 nm lateral resolution. The surface roughness R_{AFM} was measured as 2.3 nm, 5.8 nm, 9.1 nm and 2.8 nm for samples D1, D2, D3, and D4, respectively. The roughness increases with increase of Mg part in the alloy, however drops down significantly for $Mg_{0.32}Zn_{0.68}O$ epitaxial layer on GaN buffer layer (sample D4). Other surface parameters extracted from AFM data, such as peak-to-peak distance H and standard deviation σ_{AFM}, correlate with the roughness and are listed in Table 5.2.

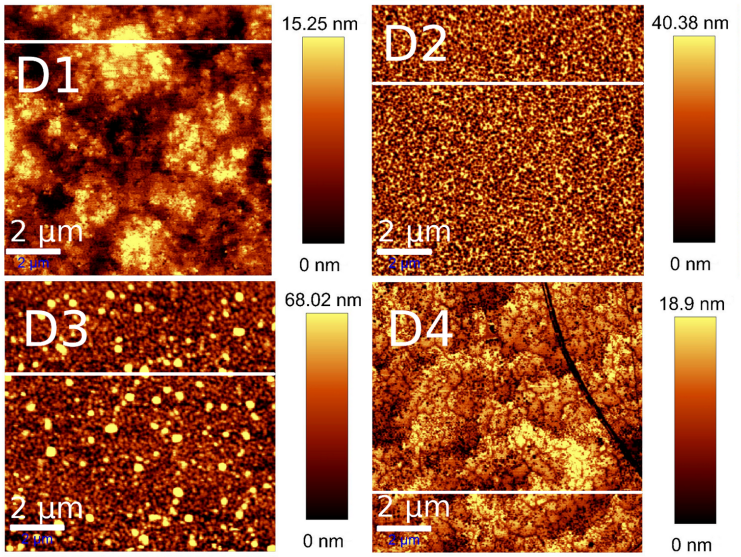

Figure 5.5: AFM images of $Mg_xZn_{1-x}O$ epitaxial layers. The samples D1 and D4 are much smoother if compare to samples D2 and D3.

5.2 Double blueshift of PL spectra of MgZnO with temperature

The room temperature PL spectra of the $Mg_xZn_{1-x}O$ epitaxial layers with various Mg content x in the alloys are shown in Fig. 5.6. The PL spectra shift to higher energy side from 3.297 eV to 4.0 eV by changing x from 0 to 0.32. Besides, the PL spectra broaden with increased Mg part in the compound and the tails towards the lower energy side becoming longer, what is the evidence of the increase of DOS tail states [111]. However, the FWHM of sample D4 PL band is 230 meV and is significantly smaller than the FWHM of sample D3 (343 meV) and rather close to the FWHM of sample D2 (184 meV). This can be explained by the use of different buffer layer in the structure of sample D4. The PL spectrum of sample D1 is similar by shape to the PL band of ZnO epitaxial layer used as a reference with FWHM values 90 meV and 84 meV, respectively. The PL spectra were measured in the same experimental conditions only changing the samples on the sample holder. Therefore, the PL intensity is comparable in arbitrary units. One can say, that even small incorporation of Mg in the ZnO lattice reduces the PL intensity. The PL intensity drops down significantly for sample D1 if compare to the PL intensity of the ZnO epitaxial layer. Nevertheless, the PL intensity increases gradually with increase of Mg content x in the alloy.

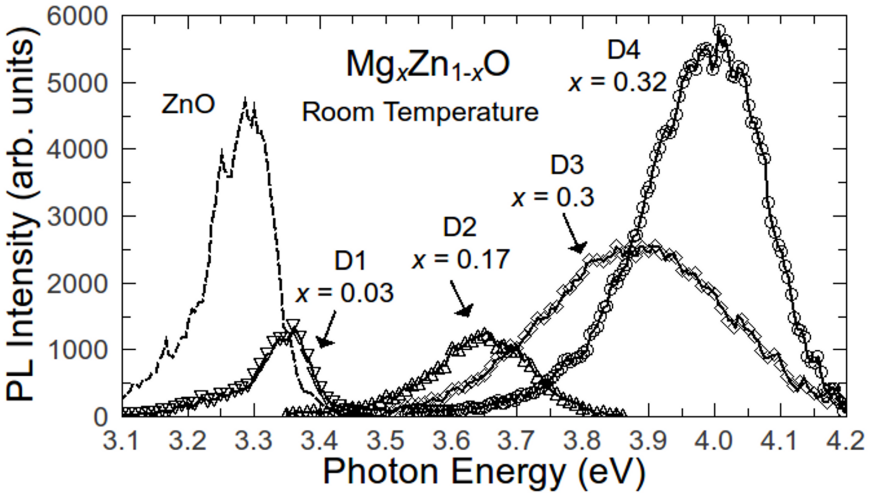

Figure 5.6: RT PL spectra of $Mg_xZn_{1-x}O$ epitaxial layers with different Mg content x, which was estimated by EDX and is depicted above the corresponding spectrum. The spectrum of ZnO epitaxial layer is depicted as a reference point for the PL peak position shift due to increasing x. The PL intensity is comparable in arbitrary units.

The peak position of PL spectra measured at 8 K temperature is depicted in Fig. 5.7. The linear fit over the experimental data gives the relation $E_{PL}^{8K} = 3.35 + 1.9x$. The result is compared with the deduced function for the PL peak position of the laser deposition grown MgZnO epitaxial layers PL spectra measured at 2 K temperature [112]. The lines have slightly different slope and the PL peak energy at $x = 0$. As it is claimed in the paper [112], the extrapolated 3.38 eV PL peak energy at 2 K temperature may be the evidence of dominant free exciton recombination in the MgZnO PL spectrum. Our results show that low temperature PL peak positions of samples D1, D2 and D3 together with PL peak position of the ZnO epitaxial layer align well. Therefore, the dominant recombination mechanism of low temperature PL band is the recombination of donor bound excitons. However, the peak position of sample's D4 PL band is slightly shifted to the higher energy side. It may be a clue for different dominant recombination mechanism of $Mg_{0.32}Zn_{0.68}O$. Although, the structural and optical properties of sample D4 do not show significant difference comparing to other samples and the recombination mechanism is still of excitonic origin [24]. Also it is worth noting, that the given relation in the paper [112] was estimated for the $Mg_xZn_{1-x}O$ epitaxial layers up to 15%. Therefore it may

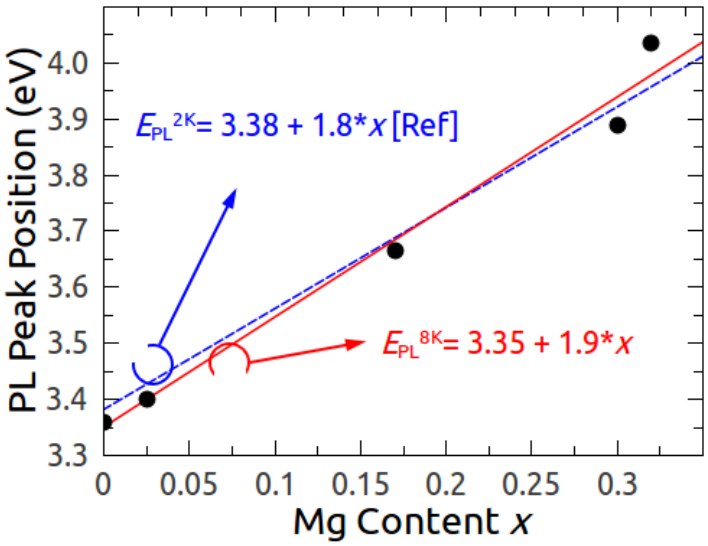

Figure 5.7: Low temperature PL spectra peak position dependence on Mg content x in the alloys. The solid line represents the linear fit over the experimental data (dots). The doted line is the fit of experimental data reported in the paper [112].

not be accurate for the higher Mg contents in the MgZnO epitaxial layers.

The PL peak position of the MgZnO band of the sample D4 dependence on temperature is depicted in Fig. 5.8. The NBE PL spectrum of MgZnO consist of single broad band at whole temperature interval. The PL peak

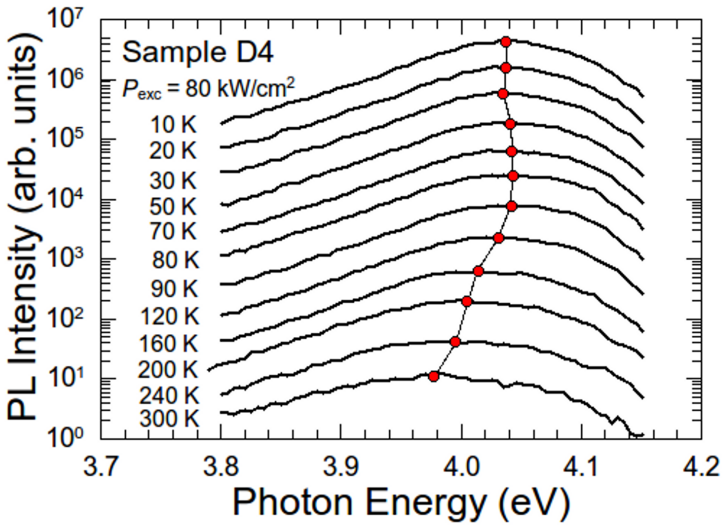

Figure 5.8: MgZnO PL band dependence on temperature of sample D4. The spectra are arbitrary shifted in the intensity scale.

position dependence on temperature follows the *S*-shape. The small red-shift occurs in temperature range from 10 to 30 K with –0.125 meV/K decrease. The blue-shift occurs in temperature range from 30 to 80 K with 0.15 meV/K increase. With the further increase of temperature from 80 to 300 K the red-shift occurs again with –0.3 meV/K decrease. However, for comparison with MBE-grown ZnO hetero-epitaxial layers the red-shift due to the temperature induced band gap shrinkage in the range from 80 K to 300 K vary from –0.36 meV/K to –0.4 meV/K, as we have measured earlier [24]. Also the value of –0.35 meV/K was reported [88]. The lower rate of band gap shrinkage with temperature in MgZnO epitaxial layers refers to anomalous behaviour as it is going to be discussed later.

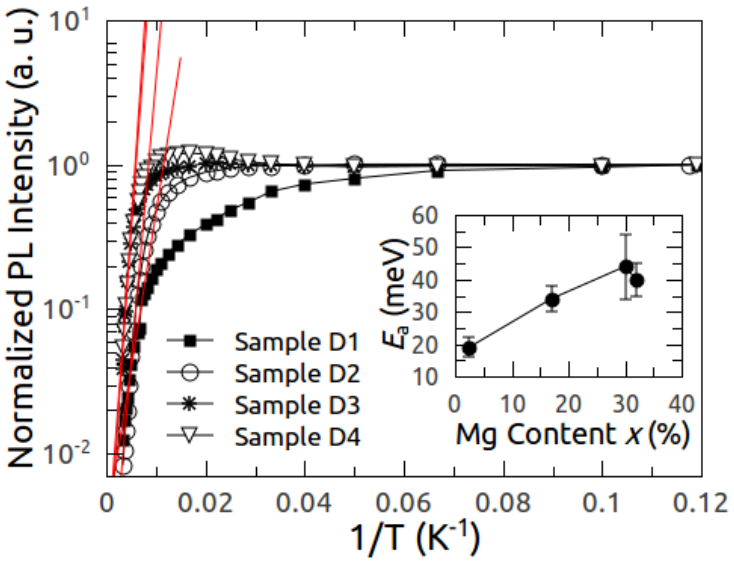

Figure 5.9: Arrhenius plot of the MgZnO emission band of MgZnO epitaxial layers with different Mg part in the alloys x. The inset shows the activation energy E_a as a function of x.

The PL intensity of the MgZnO emission band dependence on temperature is depicted in Fig. 5.9 as the Arrhenius plot. The temperature of PL intensity thermal quenching is increasing with increase of Mg part in the alloys. Moreover, for MgZnO epitaxial layers with 30% and 32% of Mg the PL intensity increases and reaches the maximum at around 30 K. The activation energy E_a was estimated from Arrhenius plot. The activation energy increases with the increase of Mg part in the alloy from 19 meV for

sample D1 with 2.5% of Mg to around 40 meV for sample D3 with 30% of Mg as it is shown in the inset of Fig. 5.9. This result coincide well with the results provided in literature [111, 113]. However, for the MgZnO epitaxial layers with high Mg content in the alloy the activation energy values are reported even higher. For example, for $Mg_{0.15}Zn_{0.85}O$ thermal activation energy $E_a = 66$ meV [111] and for $Mg_{0.37}Zn_{0.63}O$ thermal activation energy is even 127 meV [113].

The *S*-shaped PL peak position dependence on temperature is typical behaviour in case of carrier localization effect which usually takes place in ternary [80, 114, 115, 116] and quaternary [117, 118] semiconductor epitaxial layers and QWs. The model explains the non-monotonous decrease of PL peak position with increase of temperature through the thermal activation of exciton hopping. At low temperatures, the carriers are frozen so that they are strongly localized in the potential field fluctuations without escaping. However, with increase of temperature, the carriers gain thermal energy to overcome the potential field barriers and move to the lowest energy levels causing the initial red-shift of the PL peak position. With the further increase of temperature, the carriers are thermalized in the randomly distributed potential field minima occupying the higher energy levels of DOS tail states. Therefore the PL peak energy experiences the blue-shift. Furthermore, the fundamental band gap shrinkage with the temperature increase overcomes the blue-shift and causes the red-shift of the PL peak position.

The band-filling model for tails of DOS is applied in order to estimate the average potential field fluctuations depth in the $Mg_xZn_{1-x}O$ epitaxial layers. The model was derived by P. G. Eliseev *et al.* for AlGaN/InGaN/GaN QWs [115] assuming a Gaussian shape of the band tail

$$\rho(E) = \rho_0 \exp\left[-\frac{(E-E_0)^2}{2\sigma_0^2}\right], \tag{5.1}$$

where ρ_0, E_0, and σ_0 are fixed parameters for band tail. The parameter σ represents the average depth of randomly distributed potential field fluctuations. It manifest itself through the PL peak position dependence on

temperature as an additional term in Varshni function (4.1)

$$E_0(T) = E_0(0) - \frac{\alpha T^2}{(\beta + T)} - \frac{\sigma^2}{k_B T}. \tag{5.2}$$

The function well describes the blue-shift of PL peak position and allows to evaluate the average depth of randomly distributed potential field fluctuations σ [119].

In Fig. 5.10, the measured PL peak position dependence on temperature for sample D4 at different excitation power densities is shown. The results of fitting over the experimental data using function (5.2) is shown in Fig. 5.10 as lines. The fitting parameters are presented in Table 5.3. The Varshni parameters α and β were considered independent on excitation power density and kept constant. The two independent blue-shifts can be indicated in PL peak position dependence on temperature. The lower temperature blue-shift was fitted in temperature range from 40 K to 140 K. The randomly distributed potential field fluctuation parameter σ decreases from 12.1 to 10.7 meV with increasing excitation power density 20 times as shown in the inset (a) of Fig. 5.10. This behaviour is expected having in mind the screening of the potential field pattern with increased number of photo-excited carriers. When density of excitons increases the potential field fluctuations are covered and the effect diminishes. The extrapolated excitation power density at which $\sigma = 0$ meV is around 250 kW/cm^2 and it gives abrupt value of photo-excited carriers density about 1.6×10^{20} cm^{-3}.

The second blue-shift occurs at the temperature 240 K. The fitting of the experimental data in the range from 220 K to 300 K with the function (5.2) reveals the average potential field fluctuation value Γ (the adequate parameter to σ for high temperature blue-shift) from 70 to 84 meV (Fig. 5.10 inset b). However, at medium excitation regime the large potential field fluctuation pattern is not sensitive to carrier density alternation and broad distribution of the parameter may arise due to small fitting interval limited to 300 K temperature.

The presence of double-scale potential field profile was revealed by Monte Carlo simulation in case of quaternary AlInGaN alloys by K. Kazlauskas *et al.* [118]. The model well describes the *S*-shape PL peak position dependence on temperature in wide temperature range as well as *W*-shaped linewidth dependence on temperature. The σ and Γ quantitative expres-

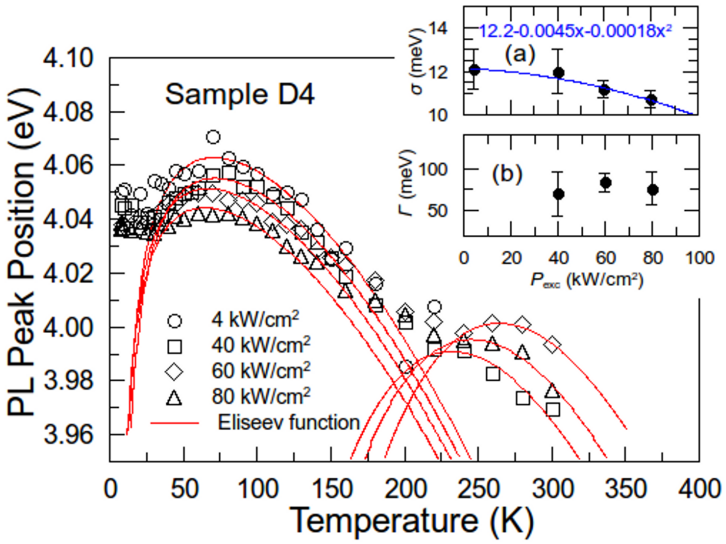

Figure 5.10: PL peak energy dependence on temperature at different excitation levels for sample D4. The lines are fitting of experimental points with Eliseev function (5.2). The inset shows the random potential field distribution parameter σ (a) and Γ (b) dependence on excitation power density P_{exc}.

Table 5.3: Eliseev function (5.2) parameter values obtained by the best fit to the peak position dependence on temperature at different excitation power densities of sample D4. The low and high temperature blue-shifts were fitted using $\alpha = 6.9 \pm 3.6$ meV/K and $\beta = 2665 \pm 557$ K.

P_{exc} kW/cm^2	E_0^{σ} (eV)	σ (meV)	E_0^{Γ} (eV)	Γ (meV)
4 ± 1	4.1 ± 0.003	12.1 ± 0.9	–	–
40 ± 10	4.094 ± 0.008	12 ± 1	4.37 ± 0.02	70 ± 2.6
60 ± 15	4.085 ± 0.02	11.2 ± 0.4	4.478 ± 0.006	84.3 ± 0.8
80 ± 20	4.076 ± 0.002	10.7 ± 0.4	4.41 ± 0.01	76 ± 2

sions in relation to experimentally available quantities T_S and Γ_S are presented in the paper:

$$\sigma = 2k_B T_S, \tag{5.3}$$

$$\Gamma = \sqrt{\Gamma_S^2 / \ln(4) - \sigma^2}, \tag{5.4}$$

where T_S is a saturation temperature of the linewidth and Γ_S is the temperature independent linewidth above the saturation temperature.

Table 5.4: Eliseev function (5.2) parameter values obtained by the best fit to the peak position dependence on temperature for $Mg_xZn_{1-x}O$ epitaxial layers with different Mg content x in the alloys.

Sample	E_0^{σ}(eV)	E_0^{Γ}(eV)	σ(meV)
D2	3.678 ± 0.001	3.92 ± 0.01	4.7 ± 0.2
D3	4.016 ± 0.002	4.46 ± 0.03	24.2 ± 0.3
D4	4.085 ± 0.002	4.48 ± 0.01	11.2 ± 0.4
Sample	Γ(meV)	α(meV/K)	β(K)
D2	54 ± 2	4.8 ± 2.5	2350 ± 491
D3	85 ± 4	9.4 ± 4.9	2166 ± 453
D4	84 ± 1	6.9 ± 3.6	2665 ± 557

In the case of sample D4 in our experiment, the W-shaped FWHM dependence on temperature was measured yielding the $T_S = 53.75$ K and $\Gamma_S = 150$ meV, therefore the calculated values are $\sigma = 9.26$ meV and $\Gamma = 127.7$ meV. The fitted σ values concur well with the calculated, however the fitted Γ values are much lower than calculated one. This disagreement may indicate the other origin of second Gaussian like DOS tails than that introduced in the model. Besides, the double-scale potential field profile was introduced in case of $Cd_{0.043}Zn_{0.957}O/Mg_{0.12}Zn_{0.88}O$ QWs in the frame of Monte Carlo simulation [120]. The estimated values are $\sigma = 20$ meV and $\Gamma = 29$ meV and these double-scale potential field fluctuations are attributed to composition and QW width fluctuations, respectively. Since our samples are ternary MgZnO epitaxial layers the origin of strongly expressed Γ potential field fluctuations is in question and it is necessary to investigate the crystal properties of MgZnO epitaxial layers in nano-scale resolution.

In Fig. 5.11, the PL peak position dependence on temperature for samples D2, D3, and D4 is depicted. All curves were measured at the fixed excitation power density of 60 kW/cm^2. The two blue-shifts were fitted with the Eliseev function (5.2) and the σ and Γ values are depicted in the inset of Fig. 5.11. The fitting parameters are presented in Table 5.4. The determined localization energy is compared with the FWHM of MgZnO PL band. The σ values for MgZnO alloys with different Mg part in the compound correlates with the PL FWHM broadening as it is depicted in inset a) of Fig. 5.11. This proves the relation of carrier localization pattern with the amount of DOS tail states caused by Mg inhomogeneous distribution. In case of sample D1, the PL peak position dependence on temperature follows the

Varshni law, therefore parameters σ and Γ in that sense are equal to 0.

5.3 Band tail filling effects in MgZnO

The model we used to describe independently two blue-shifts of the same experimental curve should give the same set of fitting parameters. In the most simple case, if two Gaussian-like DOS tails does not interact with each other, the combined fitting function would be in form

$$E_0(T) = E_0(0) - \frac{\alpha T^2}{\beta + T} - \frac{(\sigma^2 + \Gamma^2)}{k_B T}. \tag{5.5}$$

However, in such a case the sum of Gaussian DOS would manifest itself in the same way as single Gaussian DOS tail only with broader distribution over the energy. We managed to fix the Varshni parameters α and β for low and high temperature blue-shifts. However, the parameter $E_0(0)$ gives significantly different values for lower temperature and higher temperature blue-shifts as shown in Fig. 5.12 a). The difference between $E_0^{\sigma}(0)$ and $E_0^{\Gamma}(0)$ is 240, 440, and 390 meV for samples D2, D3, and D4, respectively.

In general case, the parameter $E_0(0)$ gives the extrapolated value of PL peak position at 0 K if localization effect is excluded. The dashed lines in Fig. 5.12 a) are the Varshni functions plotted using fitted parameter values with no localization responsible term in the equation (5.2) (σ or $\Gamma = 0$ meV). When the high temperature blue-shift occurs the PL peak shifts to the much lower energy side and PL peak position at low temperature should be situated around the $E_0^{\sigma}(0)$ value if there is one Gaussian DOS tail. In our case, the low temperature blue-shift lowers the PL peak position energy again to the actual measured PL peak position at 8 K temperature of $E_0^{PL} = 4.037$ eV as it is shown in Fig. 5.12 a). The difference $\Delta E_2 = E_0^{\sigma}(0) - E_0^{PL} = 38$ meV is the actual energy difference between the two Gaussian like DOS peaks. At low temperatures the first Gaussian like DOS tail is filled with the increase of temperature causing the low temperature blue-shift and at elevated temperatures the second Gaussian like DOS tail is filled causing the high temperature blue-shift of PL peak position. The estimated potential field profile for carrier localization with two spatially separated localization centres is depicted in Fig. 5.12 b).

The SNOM images of samples D3 and D4 are shown in Fig. 5.13. In

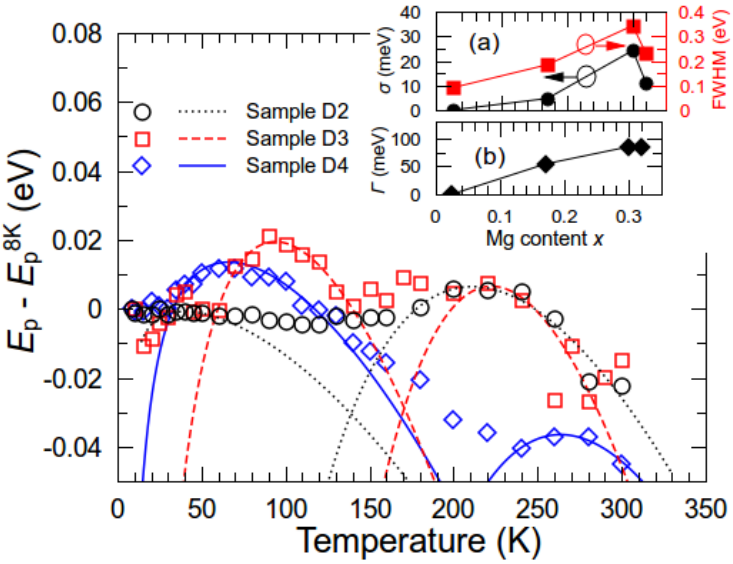

Figure 5.11: PL peak position dependence on temperature of MgZnO epitaxial layers with different Mg content x in the alloys. The lines are the fittings with Eliseev function (5.2). The inset a) shows the lower temperature localization energy σ and PL FWHM dependence on Mg content x, which correlate well. In the inset b) the Γ dependence on Mg content x is depicted.

the left-hand-side picture the PL intensity distribution in the scanned area is shown. In the right-hand-side picture the PL peak position distribution in the scanned area is shown. The SNOM images show less Mg incorporated areas with red-shifted PL spectra in high contrast. However, the PL intensity experiences anti-correlation with PL peak wavelength providing the Pearson correlation coefficient -0.51 in case of sample D4. The Pearson correlation coefficients for all samples are listed in the Table 5.5. Therefore, the SNOM experiment reveals the peculiar distribution of photo-excited carriers across the MgZnO epitaxial layers. This behaviour is abnormal from the first view, because Mg rich regions must behave as carrier scattering barriers due to greater band gap. Therefore, the PL mapping shows reversed distribution than the expected one. The Mg rich areas have the wider band gap as the introduction of Mg increases the band gap of ZnO. Naturally, one should expect the carriers to move to the lower energy areas, which has less Mg. Therefore the positive Pearson correlation coefficient should be expected.

Evidently, the photo-excited carriers are localized in Mg rich areas and are prevented to escape to lower energy states of Mg absent areas. The

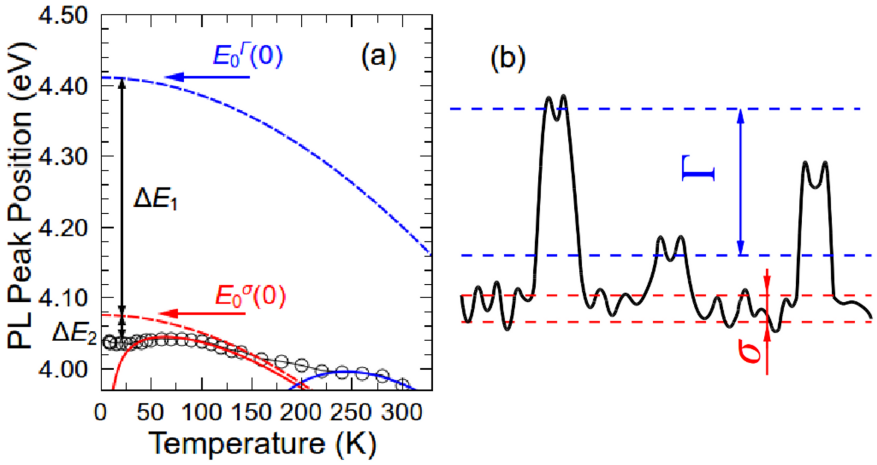

Figure 5.12: PL peak position dependence on temperature of sample D4 (open circles) and the Eliseev function (5.2) fit of low and high temperature blue shifts (solid lines) together with Varshni functions using same parameters (dashed lines) (a). Estimated potential field profile for carrier localization with two separated localization centres (b).

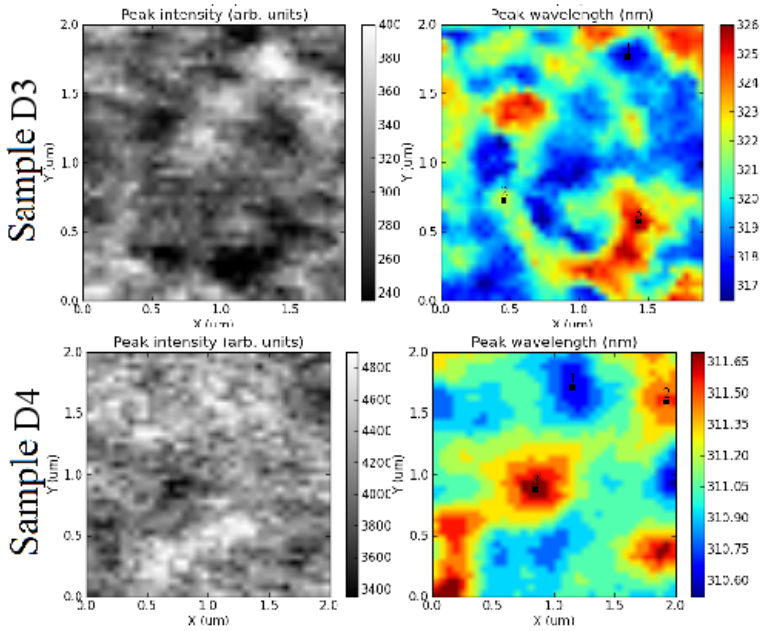

Figure 5.13: SNOM images of samples D3 (upper) and D4 (lower) with the 30% and 32% of Mg in the alloys, respectively. The left-hand-side picture shows the PL intensity distribution in the area; the right-hand-side picture shows the PL peak position distribution in the area.

Table 5.5: Correlation ρ between PL intensity I_{PL} and peak wavelength λ_p, PL intensity I_{PL} and FWHM of PL band ω, and peak wavelength λ_p and FWHM of PL band ω.

Sample	D1	D2	D3	D4
$\rho(I_{PL}, \lambda_p)$	-0.25	-0.07	-0.46	-0.51
$\rho(I_{PL}, \omega)$	0.09	-0.47	-0.52	-0.02
$\rho(\lambda_{PL}, \omega)$	-0.09	0.06	0.28	0.38

Mg inhomogeneous distribution within the Mg rich around 100 nm width areas causes the Γ localization scale. The potential field fluctuations in Mg absent areas across the sample causes σ localization scale, which is from 4 to 10 times less than Γ localization scale (see Table 5.4). If compare with thermal energy of carriers at room temperature, the σ localization scale in the Mg absent areas has no significance.

The σ and Γ dependence on Mg content in the MgZnO alloy is closely related with other structural and optical parameters. In Fig. 5.14 a), the AFM roughness R_{AFM} dependence on Mg content x is depicted together with RT PL FWHM. The Fig. 5.14 b) shows the average potential field fluctuations energy σ dependence on Mg content x in comparison with RT

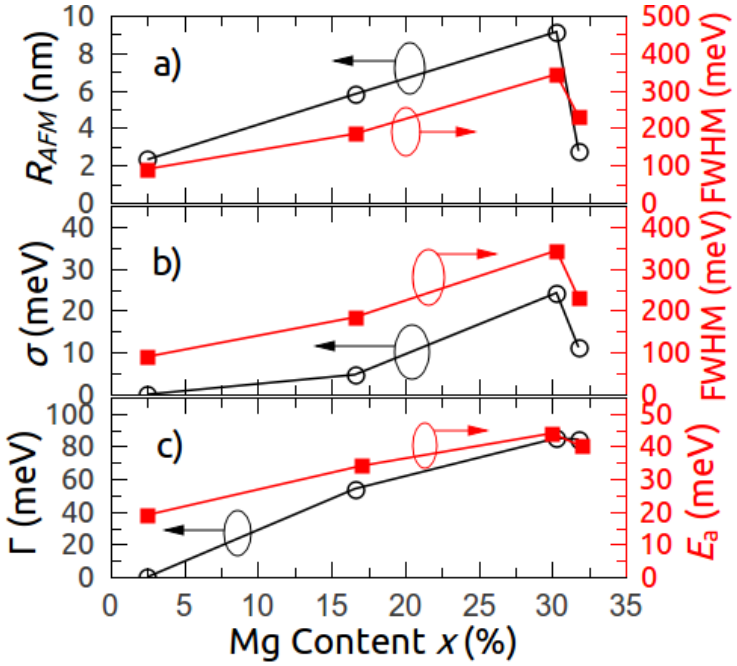

Figure 5.14: AFM roughness R_{AFM}, RT PL FWHM, activation energy E_a, average localization energy σ and Γ dependence on Mg content x in the alloy.

PL FWHM. All three quantities monotonously increase with Mg content x and sharply decrease for sample D4. The Γ dependences on Mg content together with the thermal activation energy E_a are depicted in Fig. 5.14 c). Each of the quantity increases with Mg content x and saturates at high Mg content. The FWHM of PL band has relation to the amount of DOS tails at the band edge and DOS tails are created by the structural disorder of the crystal. The potential field distortion arise due to the inhomogeneous distribution of atoms in the alloy. The thermal activation energy of PL intensity quenching has relation to the temperature induced band tail filling with carriers, what depends on the profile of DOS tails caused by localization centres.

In conclusion, the double S-shaped of PL peak position dependence on temperature was measured for MgZnO epitaxial layers with different Mg content in the alloys. The model of two Gaussian energy separated DOS tails is suggested and the average depth of fluctuating potential field was extracted to be around 10 and 75 meV. The origin of the DOS tails formation is inhomogeneous Mg distribution over the ZnO lattice. The utilization of strong carrier localization effects in MgZnO epitaxial layers may be beneficial for optoelectronic devices.

6 Optical properties of CdZnO/ZnO MQWs structures for LEDs

In this chapter, the optical characterization results of CdZnO/ZnO MQWs structures for green LEDs application are presented. As it was discussed before in section 2.2, the relatively low efficiency of green LEDs motivates to look for alternative methods to fabricate the light emitters for this particular spectral range. It was shown, that CdZnO quantum structures containing around 15% of Cd are promising for blue LEDs [121, 122, 123]. However, the optical properties of CdZnO quantum structures are poorly investigated, especially with higher Cd content in the alloy.

For that purpose, CdZnO/ZnO MQWs structures were prepared at Institute of Photonics and Optoelectronics of National Taiwan University using combined MOCVD and plasma-assisted MBE techniques [51]. The active area of the structures consists of 3 and 10 repetitive MQWs. The time-integrated temperature-dependent and transient PL experiments were carried out for optical characterisation of the structures. In order to compare the optical properties of CdZnO/ZnO MQWs structures the conventional InGaN/GaN LED structures were investigated. The InGaN/GaN MQWs structures were grown using the MOCVD technique and consist of 5 repetitive MQWs. Both LED structures were designed to emit at the wavelength of around 505 nm.

The PL properties of CdZnO/ZnO and InGaN/GaN MQWs structures are compared. The PL intensity and decay time are different by two orders of magnitude and is lower for CdZnO/ZnO MQWs if compare to InGaN/GaN MQWs. The most influential physical properties, that are responsible for lower light emission from CdZnO/ZnO MQWs, are investigated and discussed.

6.1 Growth of CdZnO/ZnO MQWs structures

Seven CdZnO/ZnO MQWs samples were fabricated using the combined plasma-assisted MBE and MOCVD techniques. The schematic drawing of the samples is shown in the Fig. 6.1. Prior to the MQWs growth, the 2 µm thick undoped GaN buffer layer was deposited at 1000 °C temperature on the 50 nm thick GaN nucleation layer deposited at 550 °C on sapphire (0001) plane substrate using MOCVD technique. The ∼1 µm thick *p*-GaN contact layer was deposited at 930 °C on the GaN buffer layer. After MOCVD growth, the targets were moved to MBE reactor for continues growth. The triple 5 nm thick CdZnO QWs and 20 nm thick ZnO barriers were grown followed by Ga doped 30 nm thick *n*-type ZnO contact layer. The Cd effusion cell temperature T_{Cd} was varied from 240 °C to 267 °C for samples E1 to E4 while the substrate temperature T_{Sub}^{QW} for growth of quantum well layers was kept constant at 170 °C for all samples. For samples E3 and E5 to E7 the Cd effusion cell temperature T_{Cd} was fixed to 260 °C while the substrate temperature T_{Sub}^{Br} for growth of barrier layers was changed from 170 °C to 420 °C.

For growth of ZnO barriers, the O_2 flow rate φ_{O2} was fixed at 1.8 sccm and the growth duration was 12 min. For the growth of the well and barrier layers, the Zn effusion cell temperature T_{Zn} was kept constant at 295 °C. For Ga doped *n*-ZnO deposition, the growth conditions were set to T_{Sub} = 550 °C, T_{Zn} = 310 °C, T_{Ga} = 700 °C for Ga effusion cell temperature, φ_{O2} = 1.8 sccm, and growth duration was 60 min. The working pressure in MBE growth chamber during the growth process was from 1.5 × 10^{-5} to 2 ×

Table 6.1: Growth conditions for CdZnO/ZnO MQWs structures for LEDs: n_{QW} is the number of QWs, T_{Cd} is Cd effusion cell temperature for growth of QW layers, and T_{Sub}^{Br} is the substrate temperature for growth of barrier layers. The substrate temperature T_{Sub}^{QW} for growth of QW layers is 170 °C for all samples.

Sample	E1	E2	E3	E4	E5	E6	E7	E8	E9
n_{QW}	3	3	3	3	3	3	3	10	10
T_{Cd} (°C)	240	250	260	267	260	260	260	260	260
T_{Sub}^{Br} (°C)	170	170	170	170	250	350	420	170	170

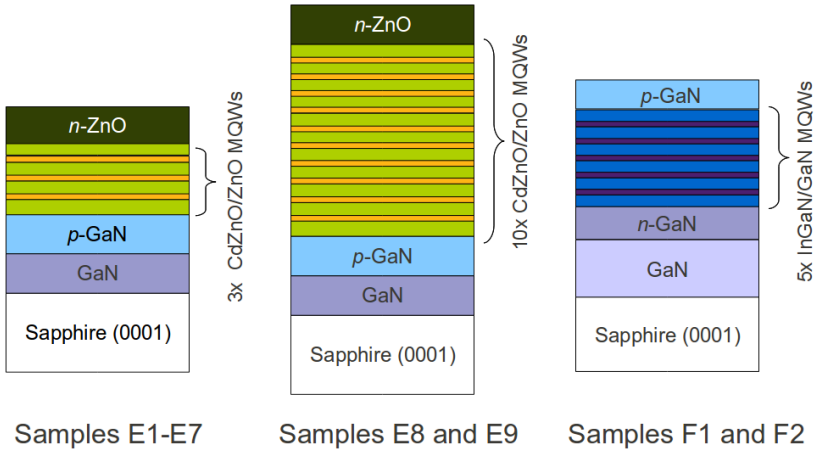

Figure 6.1: Schematic drawing of CdZnO/ZnO MQWs structures with 3 and 10 repetitive QWs and InGaN/GaN MQWs structures with 5 repetitive QWs.

10^{-5} torr. After growth process samples were *in situ* annealed at 600 °C for 10 min before moving out from the MBE reactor.

Additionally, two samples, namely E8 and E9 in Fig. 6.1, were prepared with 10 repetitive MQWs grown under near conditions as samples E3. In total, nine LED samples were prepared by varying the Cd effusion cell temperature in growing CdZnO well layers and substrate temperature in growing ZnO barrier layers. The variable growth parameters for CdZnO/ZnO MQWs LED structures is listed in the Table 6.1. Few MOCVD grown conventional InGaN/GaN MQWs LED structures with 5 repetitive QWs were selected as reference in order to compare properties of the CdZnO/ZnO MQWs structures with those of GaN based structures for LEDs, which are designed to emit at the peak wavelength of around 505 nm.

6.2 PL spectra of CdZnO/ZnO MQWs structures

The time-integrated PL spectra were measured for CdZnO/ZnO LED samples using selective excitation at $\lambda_{exc} = 403$ nm wavelength. The CW violet LD created 17 W/cm^2 excitation power density in the excitation spot of 150 µm diameter on the sample surface. The PL spectra measured at 300 K temperature of CdZnO/ZnO LED samples are shown in Fig. 6.2. The PL intensity is arbitrary comparable due to the ensured identical experimental

conditions with 10% possible deviation. Strong influence of growth conditions on PL spectra is evident. For example, the spectrum of sample E7 grown at highest substrate temperature for growth of barrier layers T_{Sub}^{Br} = 420 °C has no PL band in the spectral range of interest. Unfortunately, the growth conditions are not suitable for Cd incorporation in the ZnO layers. Probably, due to the high temperature Cd atoms evaporate from the QW layers. This is the case for sample E6 as well, which was prepared at T_{Sub}^{Br} = 350 °C. The PL spectrum of sample E6 is shifted the most to the higher energy side indicating the lowest Cd amount incorporated in the QWs. The spectra of other three samples E1, E2, and E5 are situated around 2.73 eV photon energy and have quite same spectral width and shape. Other samples are significantly shifted to lower energy side of the spectrum.

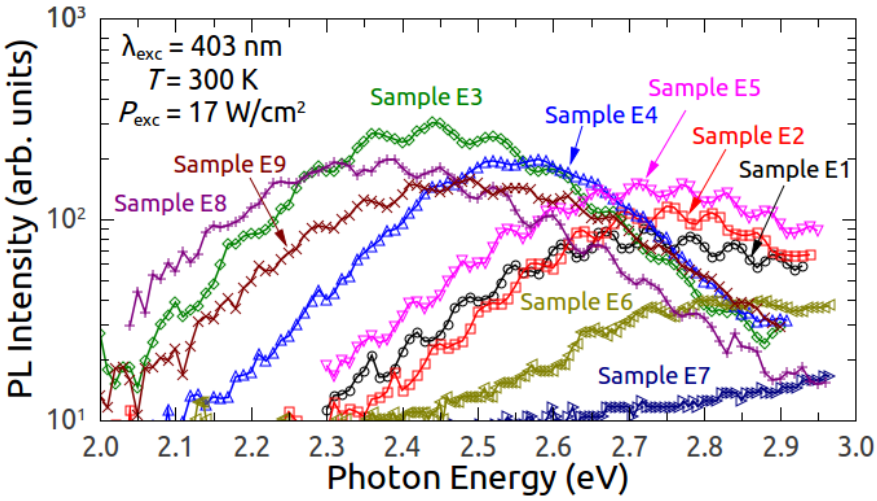

Figure 6.2: PL spectra of the CdZnO/ZnO MQWs structures measured at the 300 K temperature under selective excitation conditions. The PL intensity is comparable in arbitrary units as the spectra were measured in the same experimental conditions.

Since the QWs were excited selectively using laser wavelength λ_{exc} = 403 nm, the single PL band is observed in the spectrum decorated with interference fringes arising from the multiple reflections from the interfaces of epitaxial layers of different refraction indexes. For the extraction of the spectral parameters, the interference fringes were removed using fast Fourier transformation filtering. The main spectral parameters extracted from the

Table 6.2: Spectral parameters of the selectively excited CdZnO/ZnO MQWs PL bands at 300 K temperature.

Sample	E1	E2	E3	E4	E5	E6	E7	E8	E9
PL peak (eV)	2.72	2.75	2.44	2.56	2.73	2.76	–	2.38	2.50
FWHM (meV)	490	374	372	327	444	372	–	470	485
Cd content y (%)	16	15	26	22	15	15	–	29	24

selectively excited PL spectra are listed in the Table 6.2. The abrupt Cd concentration y in the $Cd_yZn_{1-y}O$/ZnO QWs was estimated using empirically derived Vegrad's law:

$$E_g^{CdZnO}(y) = E_g^{ZnO}(1-y) + E_g^{CdO}(y) - by(1-y) \tag{6.1}$$

where the band gap of ZnO $E_g^{ZnO} = 3.28$ eV, the band gap of CdO $E_g^{CdO} = 2.3$ eV, and the bowing parameter $b = 3.04$ eV [9]. Because of the Stoke's shift, the PL peak energy does not exactly correspond to band gap energy. As it was measured in ref. [9], the Stoke's shift for Cd content around 20% can be as large as from 300 to 400 meV. However, the used values of parameters are deduced experimentally, and for example E_g^{ZnO} is the PL peak position of ZnO band rather than actual band gap energy at room temperature. The y values are listed in Table 6.2.

In Fig. 6.3, the Cd content y in the $Cd_yZn_{1-y}O$/ZnO QWs dependence on Cd effusion cell temperature T_{Cd}^{QW} for growth of well layers is shown when the temperature for growth of ZnO barrier layers is fixed to $T_{Sub}^{Br} = 170$ °C. The inset shows the Cd content y dependence on substrate temperature T_{Sub}^{Br} for growth of ZnO barrier layers at fixed $T_{Cd}^{QW} = 260$ °C, which is important growth parameter for QWs quality as it was shown in case of samples E6 and E7. Apparently, for better Cd incorporation into the CdZnO QWs the higher T_{Cd}^{QW} but lower T_{Sub}^{Br} temperatures are preferable.

The PL spectra dependence on excitation power density P_{exc} was measured for sample E8 with highest Cd content in the active area. The PL spectra were measured at low excitation regime at room temperature and it is shown in Fig. 6.4. In the measured excitation power range the integrated PL intensity increases linearly with P_{exc} resulting the dependence power $\beta = 1$. According the comprehensive study by Netzel *et al.* [74], in the limit of a dominant nonradiative recombination, the rate equations (2.15) and

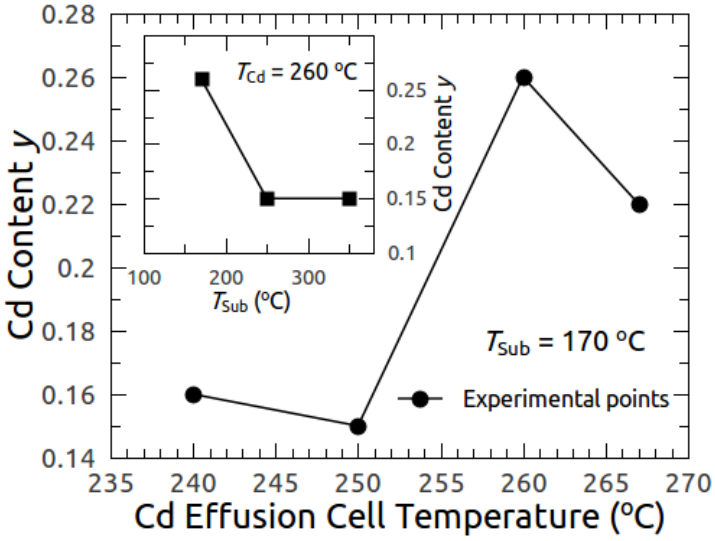

Figure 6.3: Cd content y in the $Cd_yZn_{1-y}O$/ZnO QWs dependence on Cd effusion cell temperature T_{Cd}^{QW}. The inset shows the Cd content y dependence on substrate temperature T_{Sub}^{Br} for growth of ZnO barrier layers.

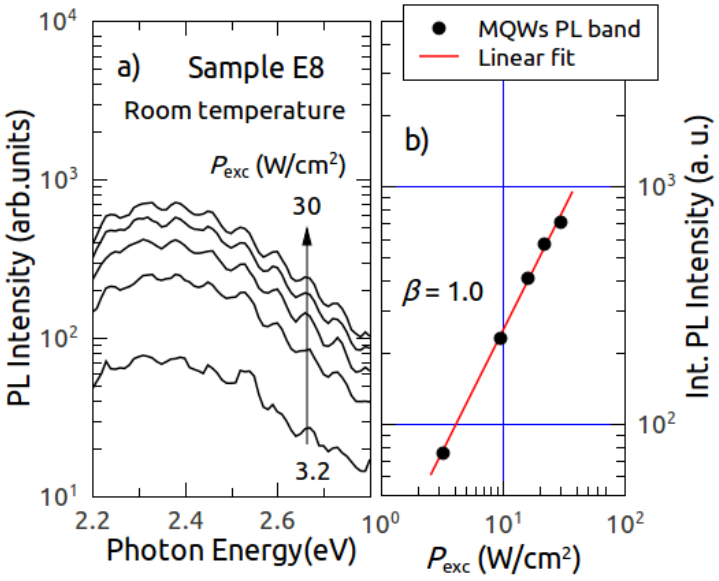

Figure 6.4: PL spectra dependence on excitation power density P_{exc} for sample E8 measured at room temperature (a). The integrated PL intensity dependence on P_{exc} in double logarithmic scale (b).

(2.18) yield $\beta = 1$ in the case of excitons and $\beta = 2$ in the case of free EHP. Therefore, one can say that PL band from CdZnO/ZnO MQWs is of excitonic nature.

6.3 PL decay time and internal quantum efficiency of CdZnO/ZnO MQWs structures

The PL decay time τ_{PL} of CdZnO/ZnO MQWs was measured in the range from 30 to 50 ps at room temperature and depends on the growth conditions of the structures, as it is depicted in Fig. 6.5. The second harmonic of mode-locked Ti:sapphire laser was used with $\lambda_{exc} = 390$ nm for excitation of MQWs selectively. The pulse duration τ_{exc} was less than 3 ps with repetition rate $f_{rep} = 76$ MHz. The excitation power density P_{exc} was around 30 W/cm^2 and the excitation energy density per pulse $I_{exc} = 7$ mJ/cm^2. The PL was measured using streak camera.

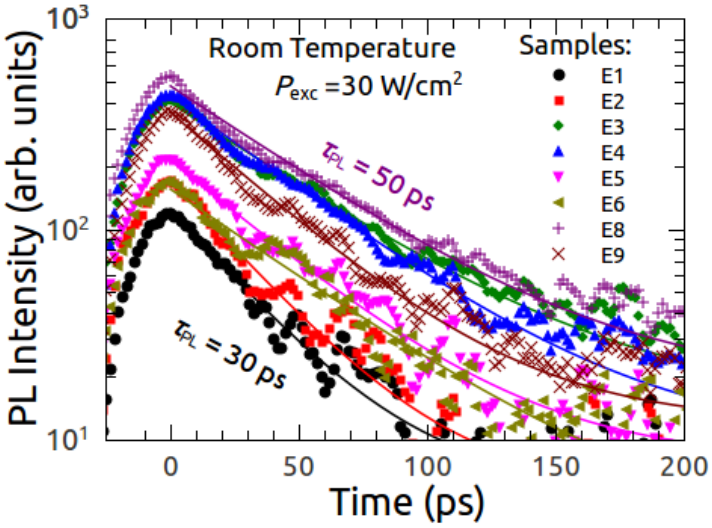

Figure 6.5: PL decay of CdZnO/ZnO MQWs LED structures measured with streak camera applying selective excitation for MQWs.

According to measured PL decay time, the samples can be separated in three groups. The lower PL decay time was measured for samples E1 and E2 and it is around 30 ps. For samples E5 and E9, the PL decay time was measured about 40 ps. For all other samples, including sample E8 with estimated highest Cd concentration in the QWs ($y = 29\%$), the PL decay time was measured around 50 ps. The PL decay time values measured for

CdZnO/ZnO MQWs structures are listed in the Table 6.3.

The PL decay time is considered as characteristic for evaluation of crystal quality [79, 98, 124]. In Fig. 6.6 the τ_{PL} is depicted as a function of Cd effusion cell temperature T_{Cd}^{QW} for growth of well layers and substrate temperature T_{Sub}^{Br} for growth of ZnO barrier layers (inset). In agreement with the discussed results in section 6.2 about the influence of growth parameters to the Cd incorporation to the layers, the PL decay time increases with the increase of Cd effusion cell temperature T_{Cd}. However, the substrate temperature T_{Sub}^{Br} for growth of ZnO barrier layers has no significant influence on PL decay time of CdZnO/ZnO MQWs.

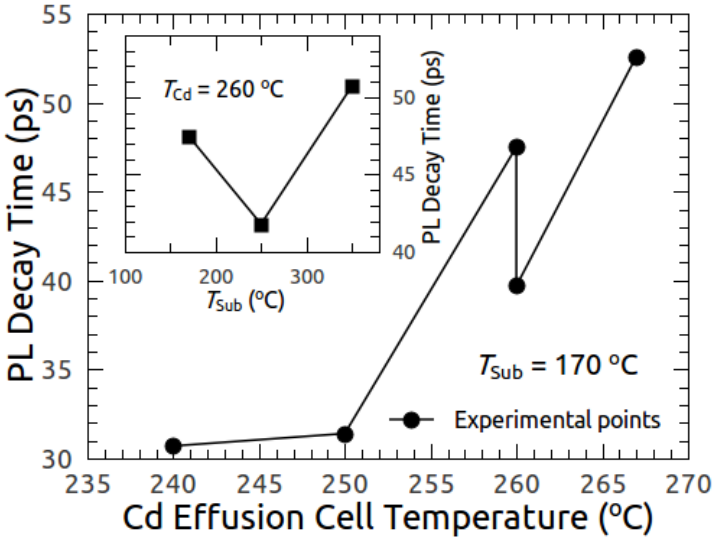

Figure 6.6: PL decay time dependence on Cd effusion cell temperature T_{Cd}^{QW}. The inset shows the PL decay time dependence on substrate temperature T_{Sub}^{Br} for growth of ZnO barrier layers.

It is worth noting, that there are only few reports on PL decay time of CdZnO quantum structures or epitaxial layers. At the time of preparation of this work, two papers were found, that reported on the PL decay time of CdZnO quantum structures. The PL decay time for laser MBE grown CdZnO/MgZnO MQWs was measured around 30 ps at 200 K temperature and shorter than the temporal resolution of setup above 200 K [41]. For plasma enhanced MBE grown $Cd_{0.16}Zn_{0.84}O$ films, the two-exponential decay with 21 ps and 50 ps lifetime was measured at room temperature [125].

Table 6.3: τ_{PL} and room temperature IQE values for CdZnO/ZnO MQWs structures.

Sample	E1	E2	E3	E4	E5	E6	E7	E8	E9
τ_{PL} (ps)	31	31	48	53	42	51	–	52	40
IQE (%)	34	25	12	12	32	–	–	5.4	7.1

For farther investigation of optical properties of the CdZnO/ZnO MQWs structures, the internal quantum efficiency (IQE) was measured. The widely used method to evaluate IQE is to measure the PL intensity dependence on temperature. On the basis of two conditions, that the radiative recombination is dominant at the low temperature and the nonradiative recombination rate does not depend on temperature, the IQE can be estimated using relation (2.12).

The PL spectrum dependence on temperature of sample E8 is shown in Fig. 6.7. The PL spectra consist of single PL band and remain of the same shape and width in all temperature range. The small red-shift can be observed with increase of temperature. The PL intensity monotonously decreases with increase of temperature. This behaviour is typical for all CdZnO/ZnO samples.

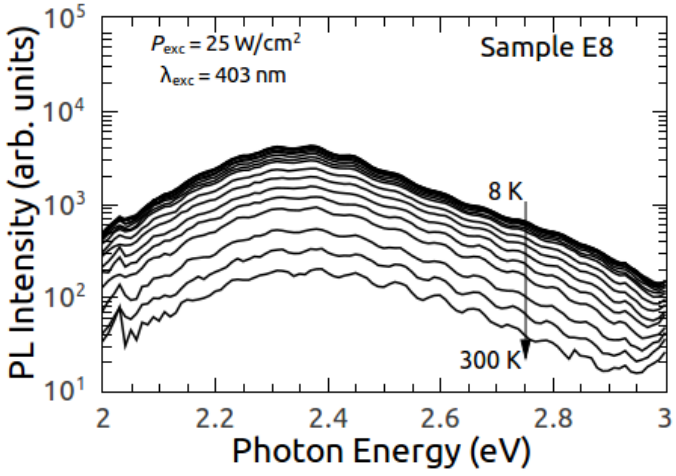

Figure 6.7: PL spectra dependence on temperature for sample E8. The spectra were measured under selective excitation at λ_{exc} = 403 nm keeping constant excitation power density of about 25 W/cm^2.

The integrated PL intensity dependence on temperature for CdZnO/ZnO MQWs samples is depicted in Fig. 6.8. The lowest temperature integrated PL intensity is normalized to unity, assuming that the radiative recombination is dominant over nonradiative and the IQE due to the radiative recombination is near 100% at the 0 K temperature limit. Therefore, in Fig. 6.8, the value of integrated PL intensity at 300 K denotes the IQE value at room temperature. The estimated IQE values for CdZnO/ZnO structures are presented in Table 6.3.

Note, that for samples with lower Cd content y in the alloys and lower PL decay time τ_{PL} the IQE values are measured significantly greater. Indeed, for samples E1, E2 and E5 IQE values are from 30% to 40%. For samples with better characteristics, namely E3 and E4, resulting IQE values are around 10%. Moreover, the samples E8 and E9 with the 10 MQWs in the active area has monotonous decrease with the increasing temperature and IQE values are 5.4% and 7.1%, respectively. These IQE values are in agreement with reported in literature. Indeed, the IQE of 5.1% and around 10% was reported for CdZnO/ZnO MQWs based LEDs by Ting *et al.* [75] and Chen *et al.* [77]. The observed contradiction can be explained in such a way, that in case of CdZnO/ZnO MQWs structures with worse crystal quality of active area due to unsuitable growth conditions the radiative recombination is low even at low temperatures, therefore the conditions for IQE evaluation is not fulfilled.

Furthermore, the carrier localization effect was measured for samples E3 and E4. In Fig. 6.9, the PL peak position dependence on temperature is depicted and it shows small blueshift in the temperature range from 30 to 60 K. By fitting the S-shaped peak position dependence with the function (5.2), which was discussed in chapter 5, the average depth of randomly distributed potential field fluctuations σ was estimated about 4.5 meV for samples E3 and E4. In Fig. 6.10, the PL peak intensity dependence on

Table 6.4: Fitting parameters on the temperature dependence of the PL intensity in CdZnO/ZnO MQWs samples E3 and E4.

Sample	c	E_a (meV)	υ	E_a^h (meV)	T_B (K)
E3	14 ± 2	31 ± 2	0.6 ± 0.1	12 ± 1	96 ± 5
E4	16 ± 4	33 ± 3	0.4 ± 0.1	10 ± 2	83 ± 7

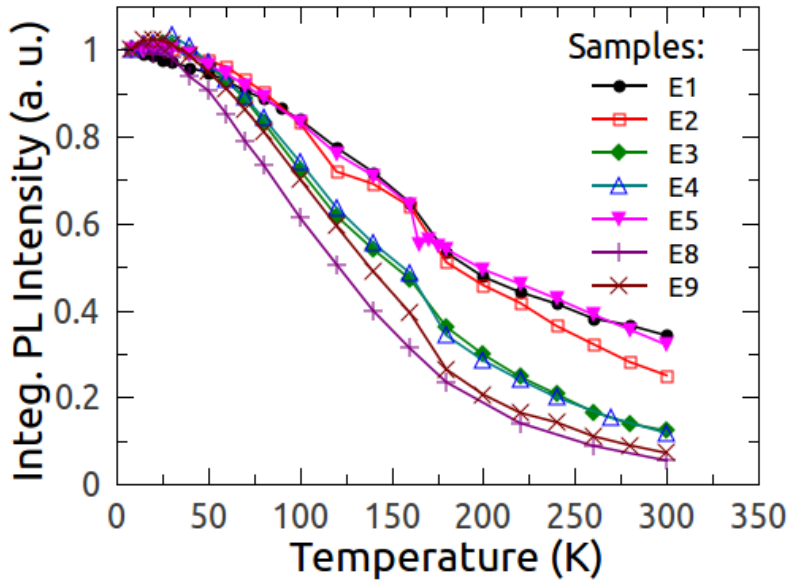

Figure 6.8: Integrated PL intensity dependence on temperature for CdZnO/ZnO MQWs structures. The 8 K temperature integrated PL intensity is normalized to unity and the integrated PL intensity at the 300 K temperature shows the room temperature IQE value if the conditions are fulfilled (see text).

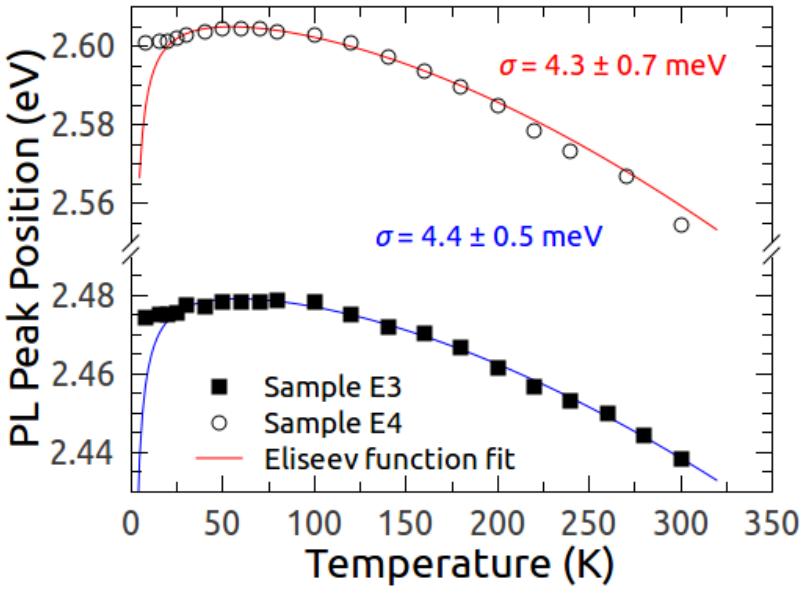

Figure 6.9: PL peak position dependence on temperature for samples E3 and E4. Points are experimental data and lines are fitting curves.

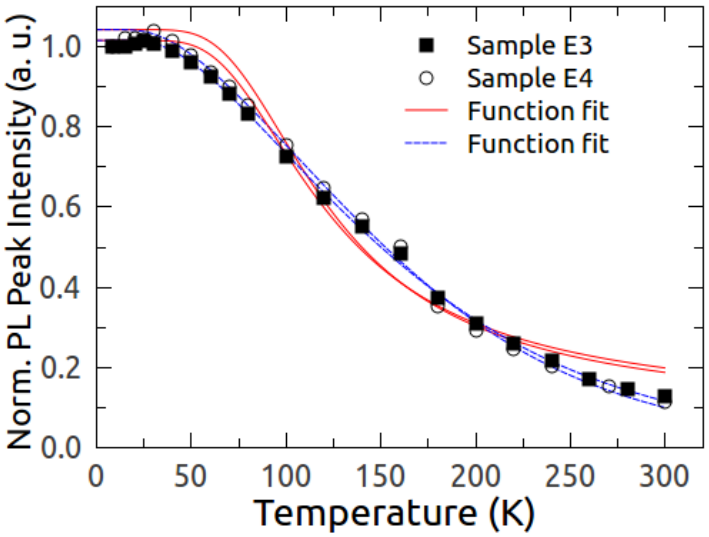

Figure 6.10: Normalized PL peak intensity dependence on temperature for samples E3 and E4. Points are experimental data. The solid lines are fitting with the function (6.2) and dotted lines are fitting with the function (6.3), which takes into account the hopping of localized carriers.

temperature was fitted with the PL intensity thermal quenching relation [126]:

$$\frac{I(T)}{I_0} = \frac{1}{1 + c\exp(-E_a/k_B T)}, \tag{6.2}$$

where E_a is the activation energy in a thermal quenching process, I_0 is the PL peak intensity at the limit of 0 K, and c is fitting parameter. The deviation of fitting results from experimental data is clearly observed. Therefore the hopping thermal quenching term was added to the relation (6.2):

$$\frac{I(T)}{I_0} = \frac{1}{1 + \upsilon\exp(-E_a^h/k_B T + T/T_B)}, \tag{6.3}$$

where E_a^h is the activation energy, T_B is a characteristic temperature, and υ is fitting parameter. The fitting of CdZnO/ZnO MQWs PL intensity dependence on temperature was significantly improved taking into account the localization of carriers. The hopping of localized carriers process contribute to the PL intensity variation with temperature and it is the evidence of carrier localization effect in MQWs. All fitting parameters are listed in the Table 6.4.

6.4 Carrier localization in CdZnO/ZnO and InGaN/GaN MQWs structures

In order to compare the measured optical properties of CdZnO/ZnO MQWs structures, two conventional InGaN/GaN MQWs structures for green LEDs, which emit at the wavelength of around 505 nm, were investigated. The InGaN/GaN MQWs sample structure is schematically drawn in Fig. 6.1.

The time-integrated PL spectra were measured for the PL intensity comparison in arbitrary units at RT with 6% accuracy caused by the change of the samples in the experimental setup. Under the same experiment conditions, the PL intensity of InGaN/GaN MQWs structures is by two orders of magnitude greater than the PL intensity of CdZnO/ZnO MQWs structures, as can be seen in Fig. 6.11.

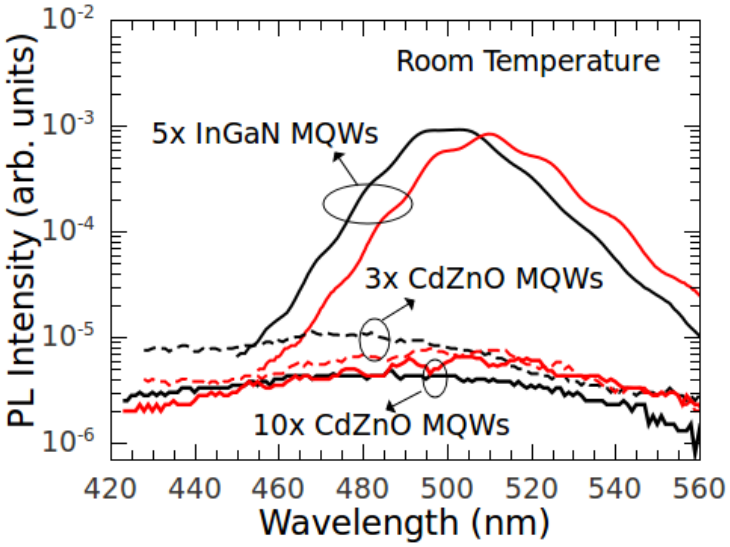

Figure 6.11: PL spectra of the CdZnO/ZnO MQWs structures and InGaN/GaN MQWs structures at RT.

The measured PL decay time at RT for InGaN/GaN MQWs is 4.2 ns and 4.0 ns for samples F1 and F2, respectively. The PL decay time of two kinds of LEDs structures differs by two orders of magnitude, as it is shown in Fig. 6.12.

The IQE was also estimated from PL intensity variation with temperature for InGaN/GaN MQWs structures. From the variation of PL intensity with

temperature the IQE values were estimated as 12% and 15% for samples F1 and F2, respectively. If compare to the IQE of CdZnO/ZnO MQWs samples, IQE is greater, but not enough to explain the observed enhancement of radiative efficiency in InGaN/GaN MQWs. In Fig. 6.13, the PL peak position dependence on temperature is shown. The well pronounced *S*-shape suggests the strong carrier localization effect in active area of InGaN/GaN MQWs. The best fitting with Eliseev function (5.2) revealed that average energy scale σ of potential field fluctuations due to inhomogeneous In distribution and QWs width deviation is more than 30 meV. Indeed, this energy is greater than thermal energy of carriers at RT, therefore the localization effect is not eliminated, at it is in the case of CdZnO/ZnO MQWs structures. The fitting parameters are listed in Table 6.5.

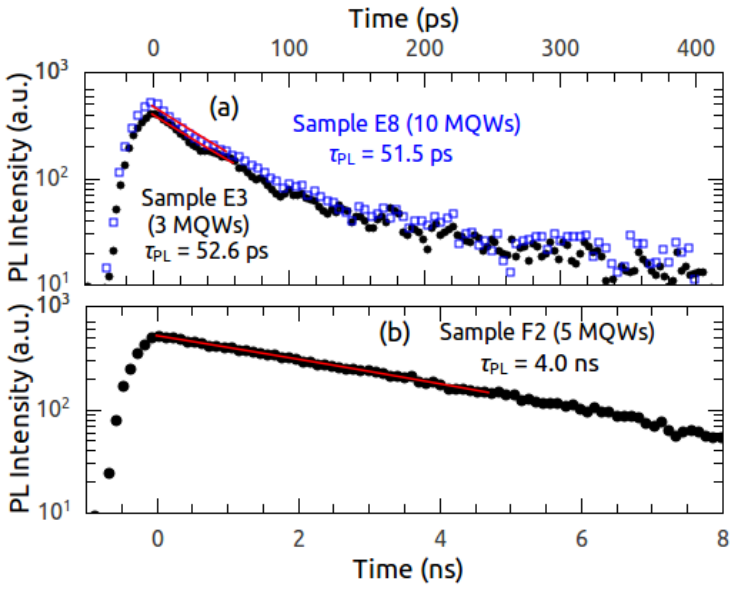

Figure 6.12: PL decay of CdZnO/ZnO MQWs structures (a) and of InGaN/GaN MQWs structure (b).

For further investigation on photogenerated carrier recombination and dynamics, five samples were selected. The LITG experiment was carried out for the carrier dynamics investigation in the MQWs structures. Due to the unavailability of selective excitation for MQWs, the ZnO barrier were also excited with third harmonic of mode-locked YAG:Nd^{3+} laser at $\lambda_{exc} = 355$ nm wavelength. Therefore, prior to the LITG experiment the

Table 6.5: Eliseev function (5.2) parameter values obtained by the best fit to the peak position dependence on temperature of CdZnO/ZnO and InGaN/GaN MQWs structures.

Sample	E_0 (eV)	α (meV/K)	β (K)	σ (meV)
E3 (CdZnO)	2.485 ± 0.002	1.0 ± 0.5	1770 ± 370	4.4 ± 0.5
E4 (CdZnO)	2.61 ± 0.01	0.9 ± 0.5	1360 ± 284	4.3 ± 0.7
F1 (InGaN)	2.5 ± 0.2	0.4 ± 0.2	690 ± 144	31 ± 13
F2 (InGaN)	2.6 ± 0.2	0.7 ± 0.4	700 ± 150	35 ± 9

transmission experiment was conducted for MQWs samples. For complex epitaxial layer samples with MQWs structure the absorption measurements are very complicated. One should expect, that absorption edge would be formed of the thicker layers, that is ZnO layers in CdZnO/ZnO MQWs LED structures. In Fig. 6.14 the plot of $(\alpha h\nu)^2$ versus photon energy $h\nu$ is depicted for the sample E8. As it was expected, the absorption edge is formed by ZnO layers and gives the band gap $E_g = 3.38$ eV. However, the closer look to the slope of the absorption edge, the linear decline intervals can be observed. The linear extrapolation to energy axis gives the absorption edge at 2.75 eV. This energy can be attributed to the CdZnO band gap energy taking into account the Stoke's shift. One can say, that non-selective excitation can also give information about QWs in transmitted light variation.

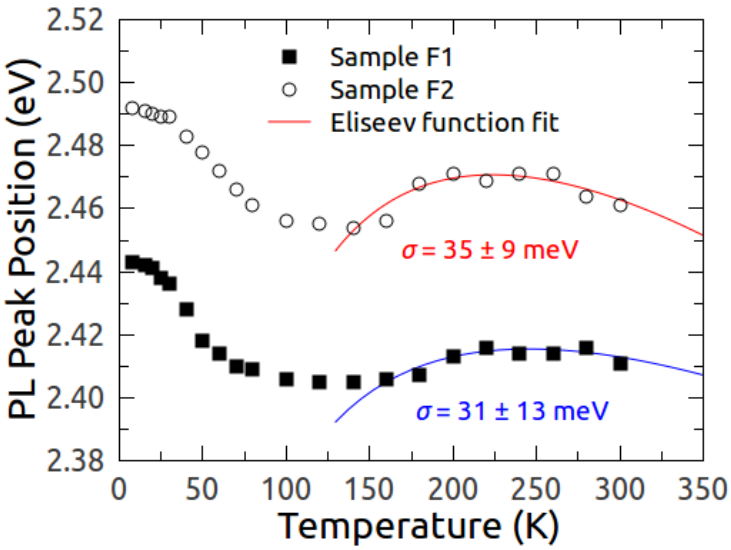

Figure 6.13: PL peak position dependence on temperature for InGaN/GaN MQWs samples F1 and F2 (dots). The lines are the fitting with Eliseev function (5.2).

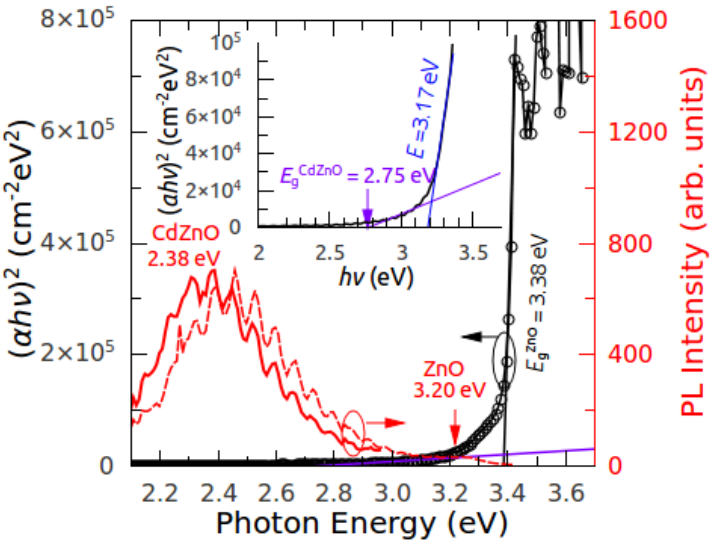

Figure 6.14: Absorption spectrum as the $(\alpha h\nu)^2$ versus photon energy $h\nu$ for sample E8 with 10 MQWs in the active area. Together the PL spectra are depicted measured under selective excitation (solid line) and non-selective excitation (dotted line). The inset shows the absorption edge of the spectrum in detail.

The diffusion coefficient was measured using the LITG technique [124]. The results of experiment for sample E3 are shown in Fig. 6.15. The measured ambipolar diffusion coefficient D_a is greater for CdZnO/ZnO MQWs structures, where the localization effect in room temperature is eliminated. The carrier recombination time τ_R is comparable for both types of structures and it is consistent with measured IQE values, which do not differ significantly. The extracted carrier mobility values μ_a are also presented in the Table 6.6 and correlates with diffusion coefficient values. Evidently, the carrier localization in the active area of LED reduces the carrier mobility in the QWs.

Table 6.6: Diffusion coefficient D, recombination time τ_r, and mobility μ of carriers in MQWs structures measured by LITG experiment.

Sample	D_a (cm^2/s)	τ_R (ps)	μ_a (cm^2/Vs)
E3 (CdZnO)	3.2	503	124
E5 (CdZnO)	4.6	510	180
F1 (InGaN)	2.6	527	100
F2 (InGaN)	0.4	500	15

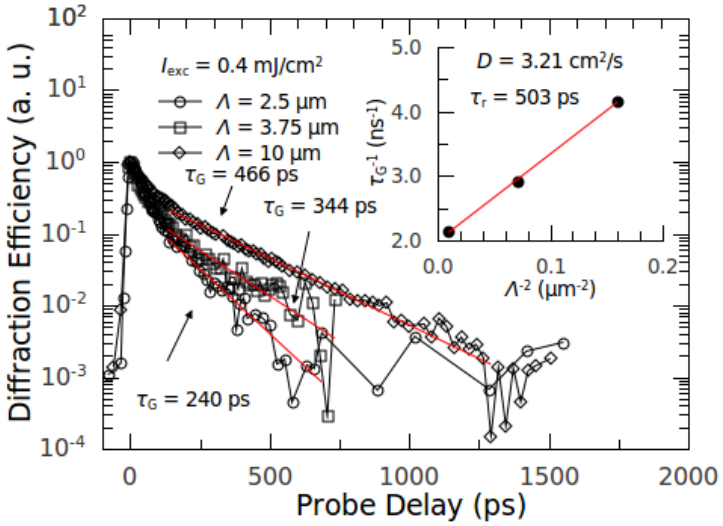

Figure 6.15: Diffraction efficiency kinetics for sample E3. In the inset the inverse grating decay time τ_G as a function of the grating period Λ is depicted.

In conclusions, the CdZnO/ZnO MQWs structures for LEDs, designed for emission at 505 nm wavelength, were characterized optically. The PL decay time was measured for the structures at RT and it is in the range from 30 to 50 ps depending on growth conditions of active area of the LED structure. The IQE was estimated from PL intensity variation with temperature. IQE values do not exceed the 10% value and for structures with worse structural quality the nonradiative recombination is dominant even at low temperature. It was shown, that small carrier localization of around 4 meV average depth of potential field fluctuations increases the radiative recombination rate at low temperatures significantly. The optical CdZnO/ZnO properties were compared with corresponding InGaN/GaN MQWs structures for 505 nm LEDs. The RT PL intensity and PL decay time were measured two orders of magnitude greater for InGaN/GaN MQWs structures if compare to CdZnO/ZnO MQWs structures. It was ascertained, that major influence has carrier localization effect in InGaN/GaN MQWs active area. The estimated average depth of potential field fluctuations is around 30 meV, what is more than thermal energy at RT.

7 Conclusions

1. The model of inelastic excitons interaction applied for indication of P-band in PL spectra of the ZnO. The experimental deviation of the P-band from theoretical peak energy position is explained by involvement of localized excitons in formation of P-band.

2. The reduced threshold and enhanced optical gain coefficient of stimulated emission was observed in the highly Ga doped ZnO and high temperature grown ZnO epitaxial layers structure, what is the result of carriers redistribution near the interface.

3. The low temperature PL spectra of N doped ZnO layers exhibit the intense band at 3.314 eV photon energy. The line is attributed to an acceptor-bound exciton recombination. It indicates the presence of the acceptor states in the band gap.

4. The double blue-shift of the PL peak position dependence on temperature was measured revealing the strong carrier localization effect in the MgZnO alloys. The model of two different Gaussian shaped DOS tails filling with temperature is introduced.

5. The SNOM experiment revealed the existence of less than 100 nm Mg rich areas with enhanced PL intensity. In these areas, the large scale field fluctuations are located and the potential field barriers prevent the carriers to escape to lower energy states in the Mg absent areas. The second carrier localization caused by the smaller potential field fluctuations are located in the Mg absent areas.

6. The CdZnO MQWs structures for 505 nm emitting green LEDs have low emission efficiency and short carrier lifetime. If compare to InGaN/GaN MQWs structures for green LEDs, the emission efficiency and the carrier lifetime is two order of magnitude lower.

7. The average depth of localization centres for CdZnO/ZnO MQWs is estimated around 4 meV, while for corresponding InGaN/GaN MQWs it is more than 30 meV. Small carrier localization effect in active area of CdZnO/ZnO MQWs is the main reason for lower radiative recombination rate.

Bibliography

[1] C. Klingshirn, The luminescence of ZnO under high one- and two-quantum excitation, Phys. Status Solidi B **71**(2), 547 (1975).

[2] K. Hummer, Interband magnetoreflection of ZnO, Phys. Status Solidi B **56**(1), 249 (1973).

[3] D. M. Bagnall, Y. F. Chen, M. Y. Shen, Z. Zhu, T. Goto, T. Yao, Room temperature excitonic stimulated emission from zinc oxide epilayers grown by plasma-assisted MBE, J. Cryst. Growth **184/185**, 605 (1998).

[4] C. Klingshirn, ZnO: Material, physics and applications, ChemPhysChem **8**(6), 782 (2007).

[5] H. Morkoç, Ü. Özgür, *Zinc Oxide: fundamentals, materials and device technology* (Wiley-VCH, 2009).

[6] Y. Chen, D. Bagnall, T. Yao, ZnO as a novel material for the UV region, Mater. Sci. Eng. B-ADV **B75**, 190–198 (2000).

[7] Y. Liu, C. R. Gorla, S. Liang, N. Emanetoglu, Y. Lu, H. Shen, M. Wraback, Ultraviolet detectors based on epitaxial ZnO films grown by MOCVD, J. Electron. Mater. **29**(1), 69 (2000).

[8] T. Makino, Y. Segawa, M. Kawasaki, A. Ohtomo, R. Shiroki, K. Tamura, T. Yasuda, H. Koinuma, Band gap engineering based on MgZnO and CdZnO ternary alloy films, Appl. Phys. Lett. **78**(9), 1237 (2001).

[9] K. Yamamoto, T. Tsuboi, T. Ohashi, T. Tawara, H. Gotoh, A. Nakamura, J. Temmyo, Structural and optical properties of Zn(Mg,Cd)O alloy films grown by remote-plasma-enhanced MOCVD, J. Cryst. Growth **312**, 1703 (2010).

[10] A. Yamamoto, K. Miyajima, T. Goto, H. J. Ko, T. Yao, Biexciton luminescence in high-quality ZnO epitaxial thin films, J. Appl. Phys. **90**(10), 4973 (2001).

[11] Y. I. Alivov, Ü. Özgür, X. Gu, C. Liu, Y. Moon, H. Morkoç, O. Lopatiuk, L. Chernyak, C. E. Litton, Hybrid II-IV and III-V compound double heterostructures and their properties, J. Electron. Mater. **36**(4), 409 (2007).

[12] T. Serevičius, S. Juršėnas, Growth, properties and sensor applications of low temperature grown ZnO nanorods, Lith. J. Phys. **51**(4), 309 (2011).

[13] Y. M. Lu, H. W. Liang, D. Z. Shen, Z. Z. Zhang, J. Y. Zhang, D. X. Zhao, Y. C. Liu, X. W. Fan, Excitonic properties of vertically aligned ZnO nanotubes under high-density excitation, J. Lumin. **119/120**, 228 (2006).

[14] C. H. Chia, T. Makino, K. Tamura, Y. Segawa, M. Kawasaki, A. Ohtomo, H. Koinuma, Confinment-enhanced biexciton binding energy in ZnO/ZnMgO multiple quantum wells, Appl. Phys. Lett. **82**(12), 1848 (2003).

[15] B. K. Meyer, H. Alves, D. M. Hofmann, W. Kriegseis, D. Forster, F. Bertram, J. Christen, A. Hoffmann, M. Strassburg, M. Dworzak, U. Haboeck, A. V. Rodina, Bound exciton and donor-acceptor pair recombination in ZnO, Phys. Status Solidi B **241**(2), 231–260 (2004).

[16] Ü. Özgür, Y. I. Alivov, C. Liu, A. Teke, M. A. Reshchikov, S. Dogan, V. Avrutin, S.-J. Cho, H. Morkoç, A comprehensive review of ZnO materials and devices, J. Appl. Phys. **98**, 041301 (2005).

[17] J. S. Liu, C. X. Shan, H. Shen, B. H. Li, Z. Z. Zhang, L. Liu, L. G. Zhang, D. Z. Shen, ZnO light-emitting device with a lifetime of 6.8 hours, Appl. Phys. Lett. **101**, 011106 (2012).

[18] H. Amano, M. Kito, K. Hiramatsu, I. Akasaki, P-type conduction in Mg-doped GaN treated with low-energy electron beam irradiation (LEEBI), Jpn. J. Appl. Phys. **28**(12), L2112 (1989).

[19] I. Akasaki, H. Amano, M. Kito, K. Hiramatsu, Photoluminescence of Mg-doped p-type GaN and electroluminescence of GaN p-n junction LED, J. Lumin. **48–49**(2), 666 (1991).

[20] S. Nakamura, Y. Harada, M. Seno, Novel metalorganic chemical vapor deposition system for GaN growth, Appl. Phys. Lett. **58**(18), 2021 (1991).

[21] S. Nakamura, M. Senoh, T. Mukai, High-power InGaN/GaN double-heterostructure violet light emitting diodes, Appl. Phys. Lett. **62**(19), 2390 (1993).

[22] S. Nakamura, G. Fosal, *The Blue Laser Diode: GaN Based Light Emitters and Lasers* (Springer, 1997).

[23] M. Karaliunas, E. Kuokstis, K. Kazlauskas, S. Jursenas, V. Hoffmann, A. Knauer, Optical gain dynamics in InGaN / InGaN quantum wells, Proceedings of SPIE-The International Society for Optical Engineering **7142** (2008).

[24] M. Karaliunas, T. Serevicius, E. Kuokstis, S. Jursenas, S.-Y. Ting, J.-J. Huang, C.-C. Yang, Optical characterization of MBE-grown ZnO epilayers, Advanced Materials Research **222**, 86 (2011).

[25] S. Burinskas, J. Dudonis, D. Milcius, M. Karaliunas, E. Kuokstis, Synthesis of ZnO:N thin films by reactive DC magnetron sputtering, Lith. J. Phys. **50**(3), 325 (2010).

[26] E. Kuokštis, M. Karaliūnas, S. Juršėnas, S. Miasojedovas, T. Serevičius, S.-Y. Ting, J.-J. Huang, C.-C. Yang, Photoluminescence studies of MBE-grown ZnO and MgZnO epitaxial layers, Phys. Status Solidi C **6**(12), 2668 (2009).

[27] V. Hoffmann, A. Knauer, F. Brunner, C. Netzel, U. Zeimer, S. Einfeldt, M. Weyers, G. Trankle, J. M. Karaliunas, K. Kazlauskas, S. Jursenas, U. Jahn, J. R. van Look, M. Kneissl, Influence of MOVPE growth temperature on the structural and optical properties of InGaN MQW laser diodes, J. Cryst. Growth **310**(21), 4525 (2008).

[28] D. M. Bagnall, Y. F. Chen, Z. Zhu, T. Yao, S. Koyama, M. Y. Shen, T. Goto, Optically pumped lasing of ZnO at room temperature, Appl. Phys. Lett. **70**(17), 2230 (1997).

[29] Y. Chen, N. T. Tuan, Y. Segawa, H.-J. Ko, S.-K. Hong, T. Yao, Stimulated emission and optical gain in ZnO epilayers grown by plasma-assisted molecular-beam epitaxy with buffers, Appl. Phys. Lett. **78**(11), 1469 (2001).

[30] A. Tsukazaki, A. Ohtomo, T. Onuma, M. Ohtani, T. Makino, M. Sumiya, K. Ohtani, S. F. Chichibu, S. Fuke, Y. Segawa, H. Ohno, H. Koinuma, M. Kawasaki, Repeated temperature modulation epitaxy for p-type doping and light-emitting diode based on ZnO, Nat. Mater. **4**, 42 (2005).

[31] A. B. M. A. Ashrafi, A. Ueta, A. Avramescu, H. Kumano, I. Suemune, Y.-W. Ok, T.-Y. Seong, Growth and characterization of hypothetical zinc-blende ZnO films on GaN (001) substrates with ZnS buffer layers, Appl. Phys. Lett. **76**(5), 550 (2000).

[32] G. H. Lee, T. Kawazoe, M. Ohtsu, Difference in optical bandgap between zinc-blende and wurtzite ZnO structure formed on sapphire (0001) substrate, Solid State Commun. **124**, 163 (2002).

[33] K. Koike, T. Aoki, R. Fujimoto, S. Sasa, M. Yano, S.-I. Gonda, R. Ishigami, K. Kume, Radiation hardness of single-crystalline zinc oxyde films, Phys. Status Solidi C **9**(7), 1577 (2012).

[34] D. C. Look, Recent advances in ZnO materials and devices, Mater. Sci. Eng. B-Adv. **80**, 383 (2001).

[35] C. Klingshirn, R. Hauschild, H. Priller, M. Decker, J. Zeller, H. Kalt, ZnO rediscovered — once again!?, Microlattice Microstruct. **38**, 209 (2005).

[36] T. Makino, G. Isoya, Y. Segawa, C. H. Chia, T. Yasuda, M. Kawasaki, A. Ohtomo, K. Tamura, H. Koinuma, Optical spectra in ZnO thin films on lattice-matched substrates grown with laser-MBE method, J. Cryst. Growth **214/215**, 289 (2000).

[37] M. Dvorak, S.-H. Wei, Z. Wu, Origin of the variation of exciton binding energy in semiconductors, Phys. Rev. Lett. **110**, 016402 (2013).

[38] R. C. Whited, C. J. Flaten, W. C. Walker, Exciton thermoreflectance of MgO and CaO, Solid State Commun. **13**, 1903 (1973).

[39] J. L. Morrison, J. Huso, H. Moeck, E. Casey, J. Mitchell, L. Bergman, M. G. Norton, Optical properties of ZnO and MgZnO nanocrystals below and at the phase separation range, J. Appl. Phys. **104**, 123519 (2008).

[40] H. D. Sun, T. Makino, Y. Segawa, M. Kawasaki, A. Ohtomo, K. Tamura, H. Koinuma, Enhansment of exciton binding energies in ZnO/ZnMgO multiquantum wells, J. Appl. Phys. **91**(4), 1993 (2002).

[41] T. Makino, C. H. Chia, N. T. Tuan, Y. Segawa, M. Kawasaki, A. Ohtomo, K. Tamura, H. Koinuma, Radiative and nonradiative recombination processes in lattice-matched (Cd,Zn)O/(Mg,Zn)O multiquantum wells, Appl. Phys. Lett. **77**(11), 1632 (2000).

[42] A. K. Sharma, J. Narayan, J. F. Muth, C. W. Teng, C. Jin, A. Kvit, R. M. Kolbas, O. W. Holland, Optical and structural properties of epitaxial MgZnO alloys, Appl. Phys. Lett. **75**(21), 3327 (1999).

[43] Philips Lumileds, *LUXEON Rebel Color Portfolio Datasheet DS68* (2011).

[44] M. Fox, *Optical Properties of Solids* (Oxford University Press, 2001).

[45] T. P. Lee, S. Chandrasekhar, *High-Speed Photonic Devices* (Wiley-Interscience, 1998), chapter 7, 409–472.

[46] A. Ohtomo, M. Kawasaki, T. Koida, K. Masubuchi, H. Koinuma, Y. Sakurai, Y. Yoshida, T. Yasuda, Y. Segawa, $Mg_xZn_{1-x}O$ as a II-VI widegap semiconductor alloy, Appl. Phys. Lett. **72**(19), 2466 (1998).

[47] Y. N. Hou, Z. X. Mei, Z. L. Liu, T. C. Zhang, X. L. Du, $Mg_{0.55}Zn_{0.45}O$ solar-blind ultraviolet detector with high photoresponse performance and large internal gain, Appl. Phys. Lett. **98**, 103506 (2011).

[48] Y. Tian, X. Ma, L. Jin, D. Li, D. Yang, Electrically pumped wavelength-tunable blue random lasing from CdZnO films on silicon, Appl. Phys. Lett. **100**, 231101 (2012).

[49] A. V. Thompson, C. Boutwell, J. W. Mares, W. V. Schoenfeld, A. Osinsky, B. Hertog, J. Q. Xie, S. J. Pearton, D. P. Norton, Thermal stability of CdZnO/ZnO multi-quantum-wells, Appl. Phys. Lett. **91**, 201921 (2007).

[50] Y. Chen, D. M. Bagnall, H.-J. Koh, K.-T. Park, K. Hiraga, Z. Zhu, T. Yao, Plasma assisted molecular beam epitaxy of ZnO on *c*-plane sapphire: Growth and characterization, J. Appl. Phys. **84**(7), 3912 (1998).

[51] S.-Y. Ting, *Growth, Characterization, and Light-emitting Diode Application of CdZnO/ZnO Quantum Wells*, Ph.D. thesis, Graduate Institute of Photonics and Optoelectronics of National Taiwan University (2012).

[52] M. A. Herman, H. Sitter, *Molecular Beam Epitaxy: fundamentals and current status* (Springers, 2006).

[53] Y. Liu, C. R. Gorla, S. Liang, N. Emanetoglu, Y. Lu, H. Shen, M. Wraback, Ultraviolet detectors based on epitaxial ZnO films grown by MOCVD, J. Electronic Mater. **29**(1), 69 (2000).

[54] H. W. Kim, N. H. Kim, Structural studies of room-temperature RF magnetron sputtered ZnO films under different RF powered cnditions, Mater. Sci. Eng. B-ADV **103**, 297 (2003).

[55] S. Burinskas, *Synthesis and Investigation of the Multicomponental Thin Films*, Ph.D. thesis, Kaunas University of Technology (2011).

[56] C. Benoit a la Guillaume, J.-M. Debever, F. Salvan, Radiative recombination in highly excited CdS, Phys. Rev. **177**(2), 567 (1969).

[57] D. G. Thomas, J. J. Hopfield, M. Power, Excitons and the absorption edge of cadmium sulfide, Phys. Rev. **119**(2), 570 (1960).

[58] T. Moriya, T. Kushida, Luminescence spectra due to exciton-exciton collisions in semiconductors. II. Stimulated emission spectra, Journal of the Physical Society of Japan **40**(6), 1676 (1976).

[59] H. J. Ko, Y. F. Chen, Z. Zhu, T. Yao, I. Kobayashi, H. Uchiki, Photoluminescence properties of ZnO epilayers grown on CaF2(111) by plasma assisted molecular beam epitaxy, Appl. Phys. Lett. **76**(14), 1905 (2000).

[60] Y.-N. He, C.-C. Zhu, J.-W. Zhang, The study on mechanism of ultraviolet laser emission at room temperature from nanocrystal thin ZnO films grown on sapphire substrate by L-MBE, Microelecronics Journal **35**, 389 (2004).

[61] T. J. Inagaki, M. Aihara, A. Takahashi, Theory of the luminescence spectra of high-density electron-hole systems: crossover from excitonic Bose-Einstein condensation to electron-hole BCS state, Solid State Commun. **115**, 645 (2000).

[62] C. J. Pan, C. W. Tu, C. J. Tun, C. C. Lee, G. C. Chi, Structural and optical properties of ZnO epilayers grown by paslam-assisted molecular beam epitaxy on GaN/sapphire (0001), J. Cryst. Growth **305**, 133 (2007).

[63] H. J. Ko, Y. F. Chen, T. Yao, K. Miyajima, A. Yamamoto, T. Goto, Biexciton emission from high-quality ZnO films grown on epitaxial GaN by plasma-assisted molecular-beam epitaxy, Appl. Phys. Lett. **77**(4), 537 (2000).

[64] J. M. Hvam, Excitonic molecule transition in ZnO, Phys. Status Solidi B **93**, 581 (1979).

[65] J. M. Hvam, G. Blattner, M. Reuscher, C. Klingshirn, The biexciton levels and nonlinear optical transitions in ZnO, Phys. Status Solidi B **118**, 179 (1983).

[66] H. Priller, R. Hauschild, J. Zeller, C. Klingshirn, H. Kalt, F. Kalt, F. Reuss, R. Kling, C. Kirchner, A. Waag, Temperature dependent dynamics of the excitonic photoluminescence in zinc oxide nanorods,

in *Physics of Semiconductors: 27th international conference on the physics semiconductors* (2005), volume CP772, 896.

[67] L. J. Brillson, Y. Dong, F. Tuomisto, B. G. Svensson, A. Y. Kuznetsov, D. Doutt, H. L. Mosbacker, G. Cantwell, J. Zhang, J. J. Song, Z.-Q. Fang, D. C. Look, Native point defects at ZnO surfaces, interfaces and bulk films, Phys. Status Solidi C **9**(7), 1566 (2012).

[68] D. C. Look, D. C. Reynolds, C. W. Litton, R. L. Jones, D. B. Eason, G. Cantwell, Characterization of homoepitaxialy *p*-type ZnO grown by molecular beam epitaxy, Appl. Phys. Lett. **81**(10), 1830 (2002).

[69] J. L. Lyon, A. Janotti, C. G. Van de Walle, Why nitrogen cannot lead to p-type conductivity in ZnO, Appl. Phys. Lett. **95**, 252105 (2009).

[70] J. G. Reynolds, C. L. Reynolds, Jr., A. Mohanta, J. F. Muth, J. E. Rowe, H. O. Everitt, D. E. Aspnes, Shallow acceptor complexes in *p*-type ZnO, Appl. Phys. Lett. **102**, 152114 (2013).

[71] Q. Qiao, C.-X. Shan, J. Zheng, B.-H. Li, Z.-Z. Zhang, L.-G. Zhang, D.-Z. Shen, Localized surface plasmon enhanced light-emitting devices, J. Mater. Chem. **22**, 9481 (2012).

[72] L. K. Wang, Z. G. Ju, J. Y. Zhang, J. Zheng, D. Z. Shen, B. Yao, S. X. Zhao, Z. Z. Zhang, B. H. Li, C. X. Shan, Single-crystalline cubic MgZnO films and their application in deep-ultraviolet optoelectronic devices, Appl. Phys. Lett. **95**, 131113 (2009).

[73] J. Chen, W. Z. Shen, N. B. Chen, D. J. Qui, H. Z. Wu, The study of composition non-uniformity in ternary MgZnO thin films, J. Phys.: Condens. Matter **15**, L475 (2003).

[74] C. Netzel, V. Hoffmann, T. Wernicke, A. Knauer, M. Weyers, M. Kneissl, N. Szabo, Temperature and excitation power dependent photoluminescence intensity of GaInN quantum wells with varying charge carrier wave function overlap, J. Appl. Phys. **107**, 033510 (2010).

[75] S.-Y. Ting, H.-S. Chen, W.-M. Chang, J.-J. Huang, C.-H. Liao, C.-Y. Chen, C. Hsieh, Y.-F. Yao, H.-T. Chen, Y.-W. Kiang, C.-C. Yang,

MBE-grown CdZnO/ZnO multiple quantum-well light-emitting diode on MOCVD-grown p-type GaN, IEEE Photonics Technology Letters **24**(11), 909 (2012).

[76] A. Hangleiter, D. Fuhrmann, M. Grewe, F. Hitzel, G. Klewer, S. Lahmann, C. Netzel, N. Riedel, U. Rossow, Towards understanding the emission efficiency of nitride quantum wells, Phys. Status Solidi A **201**(12), 2808 (2004).

[77] H.-S. Chen, S.-Y. Ting, C.-H. Liao, C.-Y. Chen, C. Hsieh, Y.-F. Yao, H.-T. Chen, Y.-W. Kiang, C.-C. Yang, Vertical CdZnO/ZnO quantum-well light-emitting diode, IEEE Photonics Technology Letters **25**(3), 317 (2013).

[78] E. Fred Schubert, *Light-Emitting Diodes* (Cambridge University Press, 2007), second edition.

[79] S. Juršėnas, S. Miasojedovas, A. Žukauskas, Rate of radiative and nonradiative recombination in bulk GaN grown by various techniques, J. Cryst. Growth **281**, 161 (2005).

[80] R. Kudrawiec, M. Syperek, P. Ploczek, J. Misiewicz, R. H. Mari, M. Shafi, M. Henini, Y. Galvao Gobato, S. V. Novikov, J. Ibanez, M. Schmidbauer, S. I. Molina, Carrier localization in GaBiAs probed by photomodulated transmittance and photoluminescence, J. Appl. Phys. **106**, 023518 (2009).

[81] J. Brandt, D. Fröhlich, C. Sandford, M. Bayer, H. Stolz, N. Naka, Ultranarrow optical absorption and two-phonon excitation spectroscopy of Cu_2O paraexcitons in a high magnetic field, Phys. Rev. Lett. **99**, 217403 (2007).

[82] A. Yamamoto, T. Kido, T. Goto, Y. Chen, T. Yao, A. Kasuya, Dynamics of photoexcited carriers in ZnO epitaxial thin films, Appl. Phys. Lett. **75**(4), 469 (1999).

[83] B. W. Hakki, T. L. Paoli, CW degradation at 300° K of GaAs double-heterostructure junction lasers. II. electronic gain., J. Appl. Phys. **44**(9), 4113 (1973).

[84] U. T. Schwarz, E. Sturm, W. Wegscheider, V. Kümmler, A. Lell, V. Härle, Optical gain, carrier-induced phase shift, and linewidth enhancement factor in InGaN quantum well lasers, Appl. Phys. Lett. **83**(20), 4095 (2003).

[85] P. S. Cross, W. G. Oldham, Theory of optical-gain measurements, IEEE J. Quantum Elect. **QE-11**(5), 190 (1975).

[86] J. Mickevičius, G. Tamulaitis, M. S. Shur, Q. Fareed, J. P. Zhang, R. Gaska, Saturated gain in GaN epilayers studied by variable stripe length technique, J. Appl. Phys. **99**, 103513 (2006).

[87] G. Behme, A. Richter, M. Suptitz, C. Lienau, Vacuum near-field scanning optical microscope for variable cryogenic temperatures, Rev. Sci. Instrum. **68**(9), 3458 (1997).

[88] L. Wang, N. C. Giles, Temperature dependence of the free-exciton transition energy in zinc oxide by photoluminescence excitation spectroscopy, J. Appl. Phys. **94**(2), 973 (2003).

[89] S. Fischer, G. Steude, D. M. Hofmann, F. Kurth, F. Anders, M. Topf, B. K. Meyer, F. Bertram, M. Schmidt, J. Christen, L. Eckey, J. Holst, A. Hoffmann, B. Mensching, B. Rauschenbach, On the nature of the 3.41 eV luminescence in hexagonal GaN, J. Cryst. Growth **189/190**, 556 (1998).

[90] D. C. Look, B. Claflin, P-type doping and devices based on ZnO, Phys. Status Solidi B **241**(3), 624 (2004).

[91] Y. P. Varshni, Temperature dependence of the energy gap in semiconductors, Physica **34**, 149 (1967).

[92] E. Kuokstis, Stimulated emission from wide-gap semiconductors, Advanced Material Research **222**, 110 (2011).

[93] J. Fallert, R. Hauschild, A. Urban, H. Priller, H. Kalt, C. Klingshirn, Processes of stimulated emission in ZnO, in W. Jantsch, F. Schaffler (eds.), *Physics of Semiconductors: 28th International Conference on the Physics of Semiconductors* (2007), volume CP893, 163.

[94] T. Moriya, T. Kushida, Luminescence spectra due to exciton-exciton collisions in semiconductors. I. Spontaneous emission spectra, Journal of the Physical Society of Japan **40**(6), 1668 (1976).

[95] N. Ohashi, Y.-G. Wang, T. Ishigaki, Y. Wada, H. Taguchi, I. Sakaguchi, T. Ohgaki, Y. Adachi, H. Haneda, Lowered stimulated emission threshold of zinc oxide by hydrogen doping with pulsed argon-hydrogen plasma, J. Cryst. Growth **306**, 316 (2007).

[96] S. Cho, J. Ma, Y. Kim, Y. Sun, G. K. Wong, J. B. Ketterson, Photoluminescence and ultravilet lasing of polycrystalline ZnO thin films prepared by the oxidation of the metallic Zn, Appl. Phys. Lett. **75**(18), 2761 (1999).

[97] P. Yu, Z. K. Tang, G. K. L. Wong, M. Kawasaki, A. Ohtomo, H. Koinuma, Y. Segawa, Room-temperature gain spectra and lasing in microcrystalline ZnO thin films, J. Cryst. Growth **184/185**, 601 (1998).

[98] S. Cho, S. I. Kim, Y. H. Kim, J. Mickevičius, G. Tamulaitis, M. S. Shur, Effects of growth temperature on exciton lifetime and sructural properties of ZnO films on sapphire substrate, Phys. Status Solidi A **203**(15), 3699 (2006).

[99] M. Mihailovic, A.-L. Henneghien, S. Faure, P. Disseix, J. Leymarie, A. Vasson, D. A. Buell, F. Semond, C. Morhain, J. Z. Perez, Optical and excitonic properties of ZnO films, Opt. Mater. **31**(3), 532 (2009).

[100] M. Oshikiri, Y. Imanaka, F. Aryasetiawan, G. Kido, Comparison of the electron effective mass of the n-type ZnO in the wurtzite structure measured by cyclotron resonance and calculated from first principle theory, Physica B **298**, 472 (2001).

[101] S.-M. Zhou, X.-H. Zhang, X.-M. Meng, S.-K. Wu, S.-T. Lee, Synthesis and optical properties of Pb-doped ZnO nanowires, Phys. Status Solidi A **202**(3), 405 (2005).

[102] A. Tredicucci, Y. Chen, V. Pellegrini, C. Deparis, Modification of excitonic emission in a GaAs bulk microcavity, Appl. Phys. Lett. **66**(18), 2388 (1995).

[103] H. Y. Liu, V. Avrutin, N. Izyumskaya, M. A. Reshchikov, Ü. Özgür, H. Morkoç, Highly conductive and optically transparent GZO films grown under metal-rich conditions by plasma assisted MBE, Phys. Status Solidi RRL **4**(3-4), 70 (2010).

[104] H. Y. Liu, V. Avrutin, N. Izyumskaya, Ü. Özgür, A. B. Yankovich, A. V. Kvit, P. M. Voyles, H. Morkoç, Electron scattering mechanisms in GZO films grown on a-sapphire substrates by plasma-enhanced molecular beam epitaxy, J. Appl. Phys. **111**(10), 103713 (2012).

[105] Z.-Z. Li, M. Bao, S.-H. Chang, Z.-Z. Chen, X.-M. Ma, Green emissions and related defects in ZnO:Ga thin films, Vacuum **86**, 1448 (2012).

[106] T. Makino, Y. Segawa, S. Yoshida, A. Tsukazaki, A. Ohtomo, M. Kawasaki, Gallium concentration dependence of room-temperature near-band-edge luminescence in n-type ZnO:Ga, Appl. Phys. Lett. **85**(5), 759 (2004).

[107] H. C. Park, D. Byun, B. Angadi, D. H. Park, W. K. Choi, J. W. Choi, Y. S. Jung, Photoluminescence of Ga-doped ZnO film grown on c-Al_2O_3 (0001) by plasma-assisted molecular beam epitaxy, J. Appl. Phys. **102**, 073114 (2007).

[108] P. Onufrijevs, T. Serevičius, P. Scajev, G. Manolis, A. Medvids, L. Chernyak, E. Kuokstis, C. Yang, K. Jarasiunas, Characterization of optical and photoelectrical properties of ZnO crystals, Acta Phys. Polonica A **119**(2), 274 (2011).

[109] E. Przezdziecka, L. Wachnicki, W. Paszkowicz, E. Lusakowska, T. Krajewski, G. Luka, E. Guziewicz, M. Godlewski, Photoluminescence, electrical and structural properties of ZnO films, grown by ALD at low temperature, Semicond. Sci. Technol. **24**, 105014 (2009).

[110] Z. L. Liu, Z. X. Mei, R. Wang, J. M. Zhao, H. L. Liang, Y. Guo, A. Yu Kuznetsov, X. L. Du, Alloy-fluctuation-induced exciton localization in high-Mg-content ($0.27 < x < 0.55$) wurtzite $Mg_xZn_{1-x}O$ epilayers, J. Phys. D: Appl. Phys. **43**, 285402 (2010).

[111] H. Shibata, H. Tampo, K. Matsubara, A. Yamada, K. Sakurai, S. Ishizuka, S. Niki, M. Sakai, Photoluminescence characterization

of ZnMgO epitaxial thin films grown on ZnO by radical source molecular beam epitaxy, Appl. Phys. Lett. **90**, 124104 (2007).

[112] S. Heitsch, G. Benndorf, G. Zimmermann, C. Schulz, D. Spemann, H. Hochmuth, H. Schmidt, T. Nobis, M. Lorenz, M. Grundmann, Optical and structural properties of MgZnO/ZnO hetero- and double heterostructures grown by pulsed laser deposition, Appl. Phys. A **88**, 99 (2007).

[113] T. A. Wassner, B. Laumer, S. Maier, A. Laufer, B. K. Meyer, M. Stutzmann, M. Eickhoff, Optical properties and structural characteristics of ZnMgO grown by plasma assisted molecular beam epitaxy, J. Appl. Phys. **105**, 023505 (2009).

[114] D. Ouadjaout, Y. Marfaing, Thermal activation of localized excitons in ZnHgTe semiconductor alloys: Photoluminescence line-shape analysis, Phys. Rev. B **46**(12), 7908 (1992).

[115] P. G. Eliseev, P. Perlin, J. Lee, M. Osinski, Blue temperature-induced shift and band-tail emission in InGaN-based light sources, Appl. Phys. Lett. **71**(5), 569 (1997).

[116] A. Ait-Ouali, A. Chennouf, R. Y.-F. Yip, J. L. Brebner, R. Leonelli, R. A. Masut, Localization of excitons by potential fluctuations and its effect on the Stokes shift in InGaP/InP quantum confined heterostructures, J. Appl. Phys. **84**(10), 5639 (1998).

[117] L. Grenouillet, C. Bru-Chevallier, G. Guillot, P. Gilet, P. Duvaut, C. Vannuffel, A. Million, A. Chenevas-Paule, Evidence of strong carrier localization below 100 K in a GaInNAs/GaAs single quantum well, Appl. Phys. Lett. **76**(16), 2241 (2000).

[118] K. Kazlauskas, G. Tamulaitis, A. Zukauskas, M. A. Khan, J. W. Yang, J. Zhang, G. Simin, M. S. Shur, R. Gaska, Double-scaled potential profile in a group-III nitride alloy revealed by Monte Carlo simulation of exciton hopping, Appl. Phys. Lett. **83**(18), 3722 (2003).

[119] E. Kuokstis, W. H. Sun, M. Shatalov, J. W. Yang, M. A. Khan, Role of alloy fluctuations in photoluminescence dynamics of AlGaN epilayers, Appl. Phys. Lett. **88**(26), 261905 (2006).

[120] T. Makino, K. Saito, M. Kawasaki, Exciton transfer between localized states in ZnO quantum well structures, Superlattices Microstruct. **42**, 206 (2007).

[121] J. W. Mares, M. Falanga, A. V. Thompson, A. Osinsky, J. Q. Xie, B. Hertog, A. Dabiran, P. P. Chow, S. Karpov, W. V. Schoenfeld, Hybrid CdZnO/GaN quantum-well light emitting diodes, J. Appl. Phys. **104**, 093107 (2008).

[122] L. Li, Z. Yang, J. Y. Kong, J. L. Liu, Blue electroluminescence from ZnO based heterojunction diodes with CdZnO active layers, Appl. Phys. Lett. **95**, 232117 (2009).

[123] H. C. Jeon, S. H. Park, S. J. Lee, T. W. Kang, T. F. George, Electronic and optical properties of CdZnO quantum well structures with electric field and polarization effects, Appl. Phys. Lett. **96**, 101113 (2010).

[124] T. Malinauskas, K. Jarašiūnas, S. Miasojedovas, S. Juršėnas, B. Beaumont, P. Gibart, Optical monitoring of nonequilibrium carrier liftime in freestanding GaN by time-resolved four-wave mixing and photoluminescence techniques, Appl. Phys. Lett. **88**, 202109 (2006).

[125] M. Gerhold, A. Osinsky, D. C. Look, Development of ZnMgCdO-based alloys and heterostructures for optical applications, in M. Razeghi, G. J. Brown (eds.), *Quantum Sensing and Nanophotonic Devices III* (2006), volume 6127, B1271, conference on Quantum Sensing and Nanophotonic Devices III, San Jose, CA, JAN 23-26, 2006.

[126] Z. Yang, L. Li, Z. Zuo, J. L. Liu, Temperature-dependent photoluminescence of CdZnO thin films grown by molecular-beam-epitaxy, J. Cryst. Growth **312**, 68 (2009).